Graduate Theses and Dissertations

8-2022

Study of Thin GaN/InGaN/GaN double graded structures for Future photovoltaic application

Mirsaeid Sarollahi
University of Arkansas, Fayetteville

Study of Thin GaN/InGaN/GaN double graded structures for Future photovoltaic application

A dissertation submitted in partial fulfillment
of the requirements for the degree of
Doctor of Philosophy in Engineering

by

Mirsaeid Sarollahi
Zanjan University
Bachelor of Science in Solid State Physics, 2000
Azad-Tehran University
Master of Science Atomic and Molecular Physics, 2007
University of Arkansas
Master of Science in Electrical Engineering, 2018

August 2022
University of Arkansas

This dissertation is approved for recommendation to the Graduate Council.

_____ _____

Morgan E. Ware, Ph.D.   Jin Hu, Ph.D.
Dissertation Director   Committee Member

_____ _____

Zhong Chen, Ph.D.   Hameed Naseem, Ph.D.
Committee Member   Committee Member

Abstract

Indium gallium nitride ($In_xGa_{1-x}N$) materials have displayed great potential for photovoltaic and optoelectronic devices due to their optical and electrical properties. Properties such as direct bandgap, strong bandgap absorption, thermal stability and high radiation resistance qualify them as great materials for photovoltaic devices. The tunable bandgap which absorbs the whole solar spectrum is the most significant feature which became attractive for scientists. The bandgap for these materials varies from 0.7 eV for InN to 3.4 eV for GaN covering from infrared to ultraviolet. $In_xGa_{1-x}N$ wurtzite crystal is grown on GaN buffer layer by Molecular Beam Epitaxy (MBE). Epitaxial growth of high quality $In_xGa_{1-x}N$ material, however, creates great challenges due to lattice mismatch between InN and GaN (up to 11%). This might be the actual reason of partially and fully strain at the interface relating to growth condition which affect optical properties of the materials. Therefore, studying solar cell parameters for different indium compositions (low to high) in the material is significant.

In this work, graded composition $In_xGa_{1-x}N$ (44 nm ramping up followed by 44 nm ramping down) were grown on GaN/sapphire template. The growth was done at different indium compositions (low to high) in plasma-assisted MBE. Additionally, optical and structural characterizations of the materials were done. The results showed that by increasing indium composition, the composition was not linearly graded as expected and was accompanied by strain relaxation along the growth direction. In other words, for low indium composition, the results showed fully strained. However, for high indium composition partially strain relaxation was seen. The optical respond of three samples was studied with photoluminescence. For the first: to study the source of each peak in aspect of either exciton or different kinds of defect states. Second, peaks related to ground state transition. Furthermore, nextnano[3] and nextnano+

software were used to simulate optical properties of 100 nm graded structures such as the band structure, ground state wave-function position as well as determine the optical transition probabilities among ground state hole and electrons as well as solar cell parameters for different structures under different strained conditions. Simulation continued for higher alloys (20% to 90%) under strain and (20%-100%) under relaxed condition. An equation like Vegard's law was created to predict the energy bandgap under strain for different indium compositions. The simulation was performed for 100 nm Λ-graded structure to find the optimum x_{max} for both conditions for maximum solar efficiency. In addition, the performance of graded structure in a Flat Base Graded (FBG) was studied to compare with Square well and Homojunction structure.

ACKNOWLEDGEMENT

I would like to acknowledge, give my warmest thanks and express my sincere gratitude to my adviser Dr. Morgan Ware for his help, support, motivation and patient to finish my PhD study. Also special thanks to my dissertation committee members for their helpful support and motivation that helped me to accomplish this research. I would like to thank my son, my parent and family members, and my sisters who have been supporting me during my education.

Table of Contents

LIST OF FIGURES

List of Tables

List of published/accepted papers

Chapters 2, 3, 4, 5 and 6 were published/ accepted in scientific journals, which are listed below with minor modification:

Chapter 2: Mirsaeid Sarollahi, Pijush K Ghosh, Manal A. Aldawsari , Andrian Kuchuk, Morgan E. Ware, 2020"Luminescence Properties of GaN/In$_x$Ga$_{1-x}$N/In$_y$Ga$_{1-y}$N Double Graded Structures (Zigzag Quantum Wells)" Journal of Electronic Materials, Springer, published on March 4,2020, https://doi.org/10.1007/s11664-020-08033-w.

Chapter 3: Mirsaeid Sarollahi, Pijush K.Ghosh, Manal A.Aldawsari, Shiva Davari, Malak I. Refaei, Reem Alhelais, Yuriy I.Mazur, Morgan E.Ware, 2021"Experiment-simulation comparison of luminescence properties of GaN/InGaN/GaN double graded structures", Journal of Luminescence, Elsevier, published on August 29,2021, https://doi.org/10.1016/j.jlumin.2021.118411

Chapter 4: Mirsaeid. Sarollahi, Rohith Allaparthi, Reem Alhelais, Manal A. Aldawsari, Malak I. Refaei, Md Helal Uddin Maruf , Morgan E. Ware, 2021 "Effects of numbers of wells on optical properties of periodic InGaN graded structure" Proceedings Volume 11800, Low-Dimensional Materials and Devices 2021; 1180016 (2021), Presented at SPIE Nanoscience Engineering, 2021, San Diego, California, United States, https://doi.org/10.1117/12.2598268.

Chapter 5: Mirsaeid. Sarollahi, Mohammad Zamani-Alavijeh ,Rohith Allaparthi, Manal A. Aldawsari , Malak I. Refaei, Reem Alhelais, Md Helal Uddin Maruf , Yuriy Mazur, Morgan E. Ware, 2022 "Study of simulations of double graded InGaN solar cell structures", Journal of Vacuum Science and Technology B (JVSTB), Accepted June 06. https://doi.org/10.1116/6.0001841

CHAPTER 1

Introduction

1.1 Introduction

Due to the enormous potential, solar energy is the most reliable and efficient alternative for fossil fuels, being much larger (several orders of magnitude) than the combination of other energy sources (Fig. 1)[1]. The amount of solar power available is ~1.7×10^{17} watts which is more than annual energy consuming by humans. There are several advantages for solar energy such as global accessibility, environmentally friendly (pollution free) and unlimited (for our purposes). Solar renewable have increased greatly in significance recently. This has been driven almost entirely by silicon solar cells.
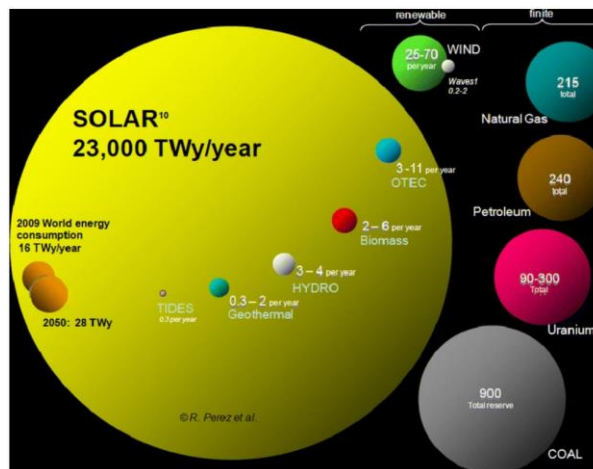
Figure 1. 1.Comparison of energy potentials of renewable energy sources and various types of fossil fuels[1]

Silicon based solar cells are the most common solar cells in the market due to low cost and potential availability. However, silicon solar cell efficiency is restricted by different phenomena like thermal and transmission loss which are due to mismatch between energy of sunlight (photons) and silicon bandgap. As cost and efficiency are two significant parameters in the solar cell industry, three generations are defined with respect to design, cost, efficiency and

development. The first generation is silicon based which has been very completely studied, characterized, developed and commercialized in the market as it is the oldest generation in photovoltaic area. There are various reports on efficiency of these cheap, stable and well known devices. The maximum efficiency for single-junction solar cell is changing between 10-26.7% experimentally [2]–[4]. Schockley and Queisser showed that the maximum theoretical efficiency limit for a p-n junction solar cell is 33.7% under standard solar spectrum (AM1.5) at 300 K at a bandgap 1.34 eV which is very similar to solar cell bandgap (1.12 eV). In the same report, they reported 30% efficiency for a bandgap of 1.1 eV [5]. Second generation solar cells are defined based on the concept of thin films in order to use less materials for reducing the cost. However, this generation displays lower solar efficiency than first generation[6]. To beat the other energy sources, overall price per watts should be reduced. It means, by increasing solar cell efficiency, reasonable cost should be considered[7]. The third generation solar cells have prevailed modern PV technology. This solar cell generation introduces tandem solar cells which includes various materials with different bandgaps on top of each other to absorb different wavelength ranges of light. The material with wide energy band gap is located at the top while the bandgap is decreased toward lower layers[8]–[10]. The theoretical maximum efficiency for a multi-junction solar cell for ∞ junction is reported as 68.2% under 1 sun, on other hand, the efficiency for 3 junction is 49.3%[11].

In aspect of marketing, the third generation solar cells can be provided under $1/Watt which is comparable with other energy sources cost[12]. Fig.1.2 shows more details about the cost of each of individual generation rate.

Other structures like multi-quantum well and intermediate band solar cells are designed to improve the efficiency of solar cells over single junction designs by creating mechanisms by

which photons with energy lower than the fundamental bandgap can be absorbed and converted to electricity[13]–[18]. These novel designs are also generally considered in the third generation of solar cells.
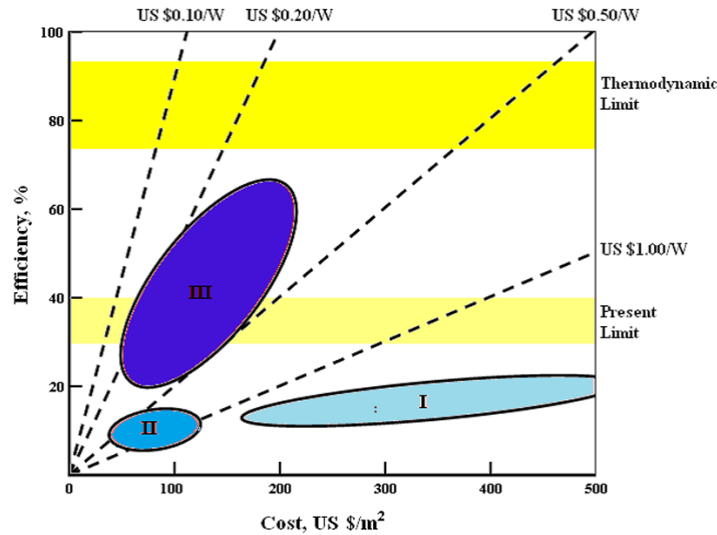
Figure 1. 2. Efficiency as a function of cost for PV generations [10].

1.1.1 How solar cell works

Consider a p-n homo-junction solar cell under illumination. Light intensity is decreased as it propagates within the structure due to absorption. In addition, as light propagates through the structure electron-hole pairs are generated at each point in the device due to the absorption of photons (Fig 1.3a,b,c). According to Fig 1.3a and b, the generation rate then has a direct correlation with the light intensity. It means generation is the maximum at the surface of the material, where the majority of the light is absorbed. On the other hand, generation is minimum when light intensity is minimum at the end of structure.

I_0 (Solar spectrum)

| p-type | n-type |

a)

$I = I_0 \exp(-\alpha x)$

b)

$G(\lambda, x) = I_0 \alpha e^{-\alpha x}$

$G (10^{18}/cm^3)$

c)
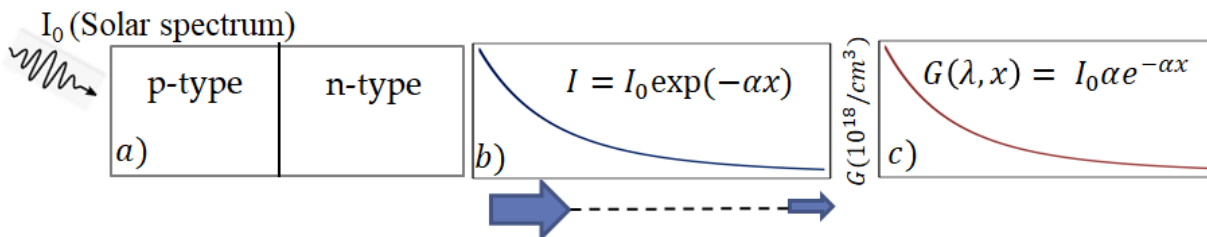
Figure 1. 3.a) p-n junction under solar illumination, b) Light intensity decrease during propagation through the structure, c) Generation rate inside the structure

The generated electron-hole pairs are moved randomly because there isn't any driving force to push them any specific direction. At p-n junction interface, some electrons diffuse to another side and recombine with hole and make a region which there isn't any free charge. Only space charges are located there. The created region is called depletion region which also forms an electric field from n to p side (from positive to negative charges). This electric filed plays an important role to act like a driving force for generated charge. When the light hits the depletion region, electron-hole pairs are generated, then the electric field in the depletion region drives the electrons and holes out of the depletion region. Electrons go toward n layer and holes leave the depletion region to p layer. If any load gets connected between regions electrons start to flow through the load. Electrons will recombine with the holes after completing their path so that the solar cell continuously gives direct current. Fig 1.4 a-e shows this process schematically.
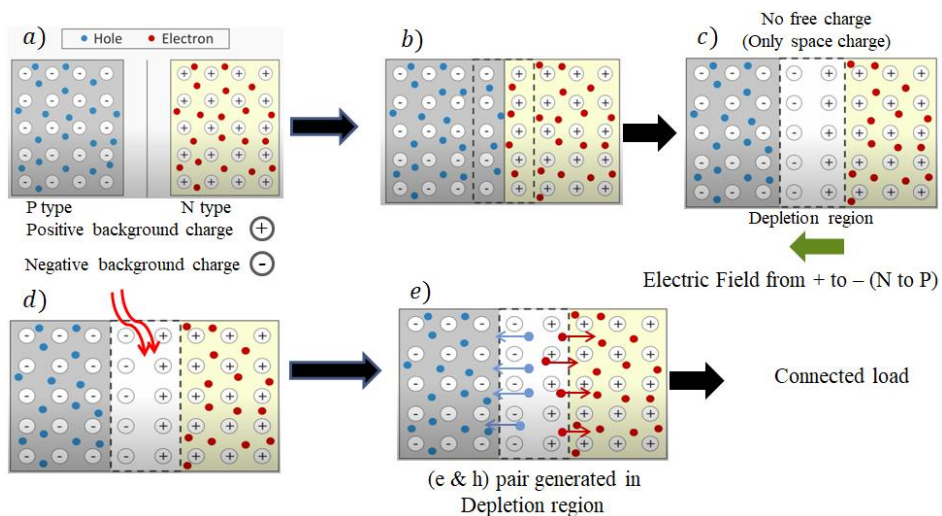
Figure 1. 4. a) introducing p and n layer , b) p-n homo-junction solar cell after joining p-n layers, c) introducing depletion region due lack of free charges, d) depletion region under illumination which creates e-h pair generation in e) which electric field in depletion region send them out of region. Then electrons are free to go through connected load continuously

1.2 Group III-V (Nitride) materials in solar cells

Binary and ternary alloys of group III nitride semiconductor materials such as GaN, InN, and InGaN are promising materials for many devices like lasers, ultraviolet detectors, high electron mobility transistors (HEMTs), solar cells, and thermo-electric devices[19]–[22]. The main important properties of these materials are wide bandgap, large breakdown voltage, an efficient electron transport, strong spontaneous and piezo-electric field[23], [24]. Tunable bandgap in $In_xGa_{1-x}N$ materials (by manipulating indium composition) is a great benefit in multi-junction solar cells which was studied in different reports [25]–[28].
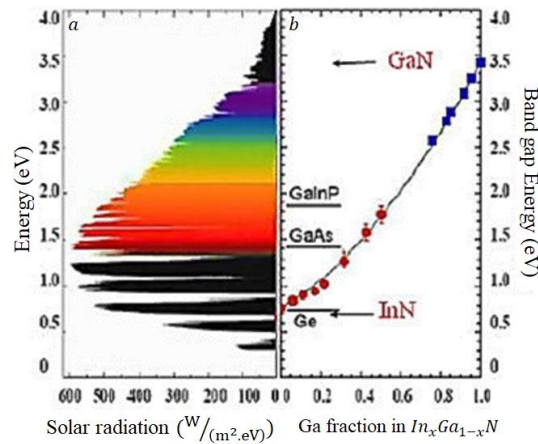
Figure 1. 5.a) solar spectrum (air mass 1.5), b) $In_xGa_{1-x}N$ bandgap energies as a function of Gallium fraction [29], [30]

The direct and tunable bandgap covering from 0.7 eV (InN) to 3.4 eV (GaN) in InGaN, which covers the whole range of solar spectrum[29],[30], as well as the high absorption coefficient ($\sim10^{-5}\ cm^{-1}$) allows for a large amount of incident sunlight to get absorbed in a very thin layer[29]–[34]. Figure 1.6a) shows the absorption coefficient for InGaN, with different alloy compositions and b) for several other materials, including Si and GaAs. The figure indicates that the InGaN absorption coefficient displays sharper function of the bandgap which is

due to the direct bandgap in these materials. In other words, a thin layer of InGaN can absorb much more light than Si.
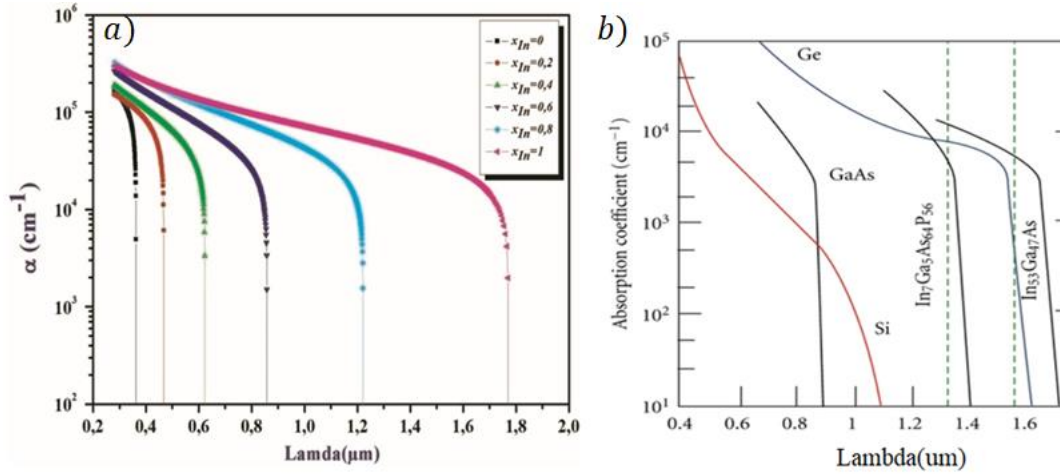
Figure 1. 6. a) Absorption coefficient for InGaN in different alloys, b) absorption coefficient for Si and GaAs [35].

Furthermore, InGaN alloys have high resistance to high photon irradiation (2 *MeV*) which is better than other alloys such as GaInP and GaAs[30]. Another great property of InGaN alloys like high electrical and thermal stability make them potentially even more useful under concentrated light[36]. Furthermore, high thermal and chemical stability, as well as radiation resistance of InGaN alloys make them suitable devices to operate in extreme conditions such as space based applications[30],[37]. Additionally, the InGaN conduction band edge is in the same level of Si valence band edge which removes the need for heavy doping at the InGaN/Si hetero-interface [38]. Fig.1. 5 shows that the $In_xGa_{1-x}N$ alloys cover almost the entire solar spectrum as the indium composition (*x*) is changed. The $In_xGa_{1-x}N$ energy band gap is given by:

$$E_g(In_xGa_{1-x}N) = xE_g(InN) + (1 - x)E_g(GaN) - bx(1 - x)$$ Equation 1. 1

in which b is called bowing parameter, $E_g(InN)$=0.7 eV, and $E_g(GaN)$= 3.4 eV. Different values are reported for the bowing parameter in the range of 1.4eV–3eV. The given wide range of bowing parameter is due to lack of enough knowledge of strain within the InGaN structures

[39]–[43]. Reported values for the bowing parameters include some composition dependency [44], [45] or not [46]–[48], however, the nextnano software uses the b=1.4 of given values [49]–[51]. The above equation is valid only when the lattice is fully relaxed.

Group III-nitride materials are the only materials among group III-V materials which exhibit spontaneous polarization (P_{sp}). The value of P_{sp} increases from GaN over InN to AlN (with a negative sign). Spontaneous polarization is created due to the non-centrosymmetric crystal structure and different electronegativity between Ga (1.81) and N (3.04) atoms in the GaN structure (Fig1.7c). An asymmetric crystal creates a condition that a polarization is generated between Ga(positive charge) and N(negative charge) atoms due to different electro-negativities [61],[62]. This is also called the pyroelectric charge. As it's seen in Figure 1. 7a), a symmetric structure has no spontaneous polarization and 7b), asymmetric structure creates spontaneous polarization. 7c) shows spontaneous polarization in the GaN unit cell. On the other hand, the presence of strain in a crystal introduces another source of polarization which is called piezoelectric polarization (P_{pz}). According to Figure 1. 7d, under relaxed, crystal doesn't show any polarization. Figure 1. 7e) shows forces which are due to strain in respect to substrate lattice constant. Figure 1. 7f) shows piezoelectric polarization due to strain.
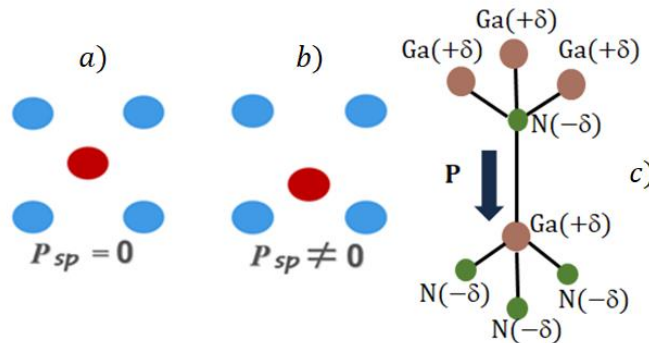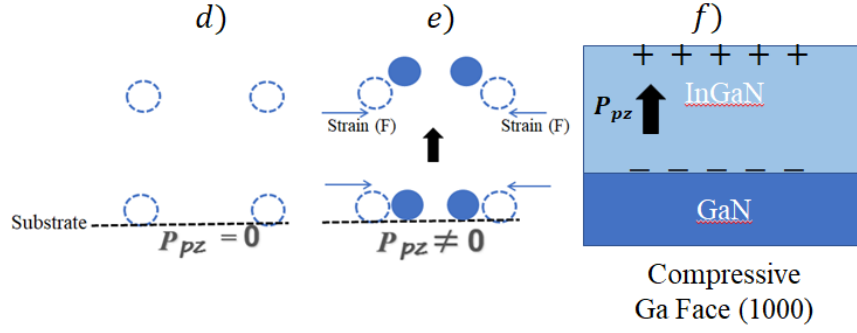
Figure 1. 7.Spontaneous polarization and piezoelectric polarization of InGaN displayed on a pseudo-substrate of GaN, a) symmetric, b) asymmetric structure and c) spontaneous polarization in GaN (Ga face 0001), d) crystal under relaxed, e) crystal under strained to substrate, f) piezoelectric polarization due to compressive strain.

The InGaN lattice constant is larger than the GaN lattice constant so InGaN layers grown on GaN substrates are under compressive strain, so the total polarization is given by $\vec{P} = \overrightarrow{P_{sp}} + \overrightarrow{P_{pz}}$.

The polarization which is built at the interface of InGaN/GaN contains spontaneous polarization (P^{sp}) and piezoelectric polarization (P^{pz})effects due to strain which are dependent on indium composition (x). Total polarization is defined by [23], [63], [64]:

$$P = \left[P^{sp}_{In_xGa_{1-x}N} - P^{pz}_{In_xGa_{1-x}N} \right] - P^{sp}_{GaN} \qquad \text{Equation 1. 2}$$

In addition, piezoelectric polarization for $In_xGa_{1-x}N$ is described by Vegard's law like [23], [63],[64]:

$$P^{pz}_{In_xGa_{1-x}N} = xP^{pz}_{InN}[\varepsilon(x)] + (1 - x)P^{pz}_{GaN}[\varepsilon(x)] \qquad \text{Equation 1. 3}$$

The equations for P^{sp} and P^{pz} are given as:

$$P^{pz}_{InN} = -1.373\varepsilon + 7.559\varepsilon^2 \qquad \text{Equation 1. 4}$$

$$P^{pz}_{GaN} = -0.918\varepsilon + 9.541\varepsilon^2 \qquad \text{Equation 1. 5}$$

$$P^{ps}_{In_xGa_{1-x}N} = -0.042x - 0.034(1 - x) + 0.038x(1 - x) \qquad \text{Equation 1. 6}$$

where ε is defined as the strain induced between the lattice parameter of a_s (substrate lattice constant) and a_e (epilayer lattice constant) by:

$$\varepsilon(x) = \frac{|a_s - a_e(x)|}{a_e(x)} \qquad \text{Equation 1. 7}$$

The discontinuity of P between GaN and InGaN produces a polarization charge with an interfacial density σ_s. Actually, the charge distribution is close to interface. The polarization charges are distributed in a few atomic layers thick ($w_{pz} = 1\ nm$) [65] then we consider that polarization charges describe for bulk charge density ρ_{pz}:

$$\rho_{pz} = \frac{(1 - R)P_{pz} + P_{sp}}{w_{pz}} \qquad \text{Equation 1. 8}$$

where R is the parameter correlated to the InGaN partial relaxation, and hence the degree of polarization charges. R=1 defines a fully relaxed lattice and R=0 is related to a fully strained InGaN layer [23].

1.3 Challenges of InGaN solar cells

In contrast with these benefits, some limiting factors are reported which affect the performance of the InGaN solar cell. Achieving a high indium composition in a thick layer is reported as a challenging process [52]. Meanwhile, many InGaN solar cell structures were fabricated with different designs such as homo-junction [53] and double hetero-junction [54], [55]. In majority of them, the solar efficiency was low. New structures like InGaN/GaN based semi-bulk and multiple quantum well (MQW) were fabricated to improve the conversion efficiency. Other reports claimed that growing InGaN alloys over the entire indium composition range when the layer is located within an InGaN/GaN double hetero structure don't show any phase separation [56]–[58]. In a graded structure with the indium composition linearly increasing from GaN to a maximum indium composition, x_{max}, then back to GaN in a symmetric structure

9

(like a Λ-shape), highly strained regions with high indium composition can be achieved while dislocations and phase separation are avoided[59],[60]. In simulation, getting a high efficiency was possible but the actual differences between simulation and experimental results have been allotted to the low quality of InGaN crystal. In addition, there are some reports on weak performance of InGaN in high indium composition thin films which restrict development for solar cells. Solar cells based on InGaN have been fabricated in low indium compositions (high bandgap energies) [66]–[69] which only allows photons with high energies (short wavelengths) to participate in absorption. To improve solar cell performance, increasing the indium composition will help to cover a major part of solar spectrum but solid phase immiscibility between GaN and InN causes phase separation in high indium composition in InGaN alloys which affect InGaN device performance [69]–[71]. Other challenges are explaining subsequently:

1.3.1 Lattice mismatch

There isn't any available lattice matched substrate to grow InGaN. The most common substrate to grow InGaN alloys on is sapphire with very large lattice mismatches for GaN (14%) and InN (29%), which create extensive defect states reducing the crystal quality. The common solution is to grow a thick GaN template layer to make an acceptable match to decrease dislocations. In addition, there is a lower lattice mismatch (11%) between InN and GaN compare with GaN/sapphire which slightly decrease strain at GaN/InGaN interface [72]. For $In_xGa_{1-x}N$, there is a critical thickness above which strain relaxes to form dislocations. The critical thickness is reported to be a few nanometers (5 nm) for $x > 20\%$ [73]. When the critical thickness is exceeded, dislocations form which can limit device performance. The resulting

threading dislocations (TD) can creating, so-called, V-defects [69],[70] resulting shadowing in solar cells due to absorption and recombination at the defects [71].

On the other hand, some reports on real devices claimed this low lattice mismatch still has destructive effects on their performance. For example, by growing InGaN/GaN multiple quantum wells (MQW) on sapphire, the strain-induced piezoelectric field creates c-plane compressive stress and quantum confined stark effect (QCSE) that decreases the performance of green LEDs by decreasing the electron-hole wave-function overlap, resulting in reduced relative recombination efficiency [72]–[81].

1.3.2 P type doping

Designing and providing p type layers in solar cell structures is crucial. However, providing p type doping in InGaN alloys is difficult. First, this is due to the high background electron concentration (10^{17} cm^3), which is created by defect states due to impurity atoms such as oxygen and hydrogen as well as vacancies of nitrogen [25],[26]. Second, this is due to the deep acceptor level of Mg in GaN of ~200 meV resulting in very small quantities of thermally excited holes. In comparison. Si as a donor atom, has an activation energy of 15 to 20 meV, resulting in much higher efficiency for n type doping. [27], [28], [87].

$$\approx 15 \ to \ 20 \ meV \updownarrow \begin{array}{l} \rule{6cm}{0.4pt} \ CB \\ - - - - \ \text{Donor level} \end{array}$$

$$\updownarrow \begin{array}{l} - - - - \ \text{Mg Acceptor level} \\ \approx 200 \ meV \\ \rule{6cm}{0.4pt} \ VB \end{array}$$
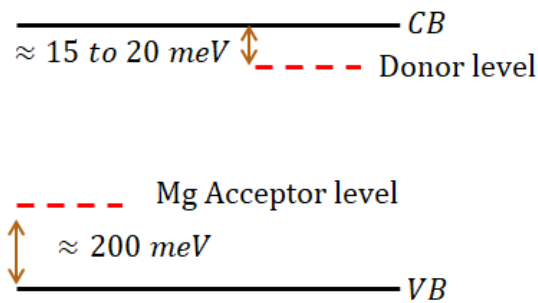
Figure 1. 8. Activation energy for donor and acceptor within the bandgap

In addition, theoretically, large hole concentration can get obtained when Indium composition is high. However, degeneration in crystal quality causes low hole concentration in

high Indium composition [88]. Using P-GaN/n-InGaN heterojunction instead of homojunction is provided as a solution for the p-type difficulty [21], [89], [90]. In this model, a highly conductive p-type GaN layer makes the hole contact and the top layer is an InGaN layer which has lower bandgap is located to absorb the incoming light. In addition, the GaN acts like a layer to reduce surface recombination. Burnham. et al grew a highly conductive p type GaN layer with resistivity less than 1.3 Ω cm which yield a low resistance window layer [91]. However, another report showed that the valence band in this model contains a discontinuity which increases with indium compositions. The reported discontinuity limits photo-generated holes from passing the heterojunction, which lowers the device efficiency [92].

1.4 Growing method-Molecular Beam Epitaxy (MBE)-advantages

The MBE growth method was developed early in the 1970's. However, others were working on epitaxial film before that [93]. MBE system works at very low pressures below 10^{-10} Torr, which is many orders of magnitude lower than competing techniques like MOCVD which generally operates around 10^{-7} Torr. Low pressure in the system creates low contamination from gasses such as CO_2, CO, N_2 and O_2. The quality of the growth material is highly correlated to the impurity of arrival atoms. In addition, another advantage of MBE growth is the low growth rate. The grow rate is approximately 180 nm/hour which allows better control of the crystal growth even down to the level of monolayers of the crystal [94]. Material sources and dopant materials are located in effusion cells. Solid materials are in different crucibles. Crucibles are made of pyrolytic boron nitride (PBN). Crucibles are heated until the materials evaporated. Heating is performed by either ohmic heating from a filament wound near the crucible or by electron beam heating. In the latter, thermionic electrons get accelerated toward the source materials by a few KV potential and deposit tens of watts, including heating in

the source material [95]. Heating type is chosen due to required flux for the materials and melting point of the material. For indium, the melting point is 156 °C but to achieve a suitable flux, the required temperature is more than 700 °C [96]. However, for Tungsten, the melting point and flux are different. According to above information, resistive filament heating is suitable for the indium evaporation.

In this work, double InGaN graded structures were designed and studied. The actual solar cells were made from $In_{0.03}Ga_{0.97}N$ instead of GaN. The correlation between temperature and indium flux isn't a linear equation:

$$T = 37.38 * log(Indium\ Flux) + 1363.7 \qquad \text{Equation 1. 9}$$
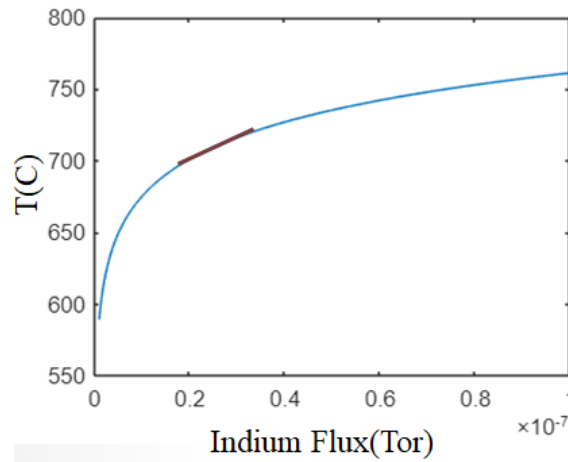
Figure 1. 9. Indium flux versus temperature in MBE growth

Going from 0 K to other temperatures would be time consuming and it would take several hours. So growing from GaN to any other alloys is impractical. The results show that changing temperature from 2%(3%) to higher indium composition is small change in temperature. So in this study, the samples were started at 3% to x_{max}. In this work, all samples contain $In_{3\%}Ga_{97\%}N$ then indium linearly increases to x_{max}.

The main advantage of using graded structure is to overcome the p type growth difficulty in the group III-nitride structures due to polarization doping. In graded structures, in which the

material composition is changing linearly versus position, the structure creates a region with a

fixed volume charge as polarization changing by:

$$N_D^{pol}(z) = \frac{(P(z_0) - P(0))}{z_0}$$

Equation 1. 10

$P(z_0)$ is assigned to the spontaneous and piezoelectric polarization of AlGaN, Al

composition is at z=z0. In case of grading from GaN to $Al_xGa_{1-x}N$ a linear charge is produced.

Along the growth direction which is the z direction, polarization changes. The fixed background

polarization charges are positive so electrons are attracted into the field, realizing the formation

of 3D gas, and make the graded layer (when Al composition is increasing) n type. In reverse

condition, when Al composition is decreasing the fixed background charges are negative so to

make a neutral area, holes are induced by polarization field over the graded AlGaN layer

continuously to form a mobile 3D hole gas and make the layer p type [96]. For InGaN the

direction of the polarization field and induced charge types are reverse. It means by increasing

indium composition the background fixed charges are negative which make a p type layer. On

the other hand, by decreasing indium composition the fixed background charges are positive

which make the layer n type.
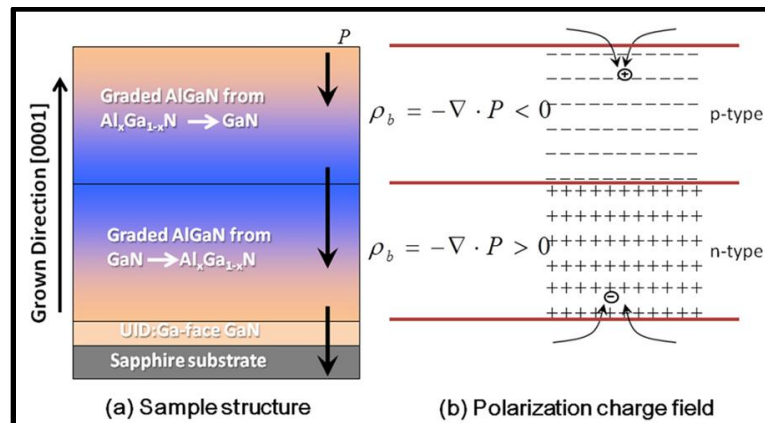
Figure 1. 10.(a) Sample structure of graded AlGaN pnjunction on Ga-face template, (b)
polarization charge field is created by grading AlGaN on GaN [97].

1.5 Photoluminescence

When a light source with equal or higher energy hits a semiconductor structure, it can excite an electron from the conduction band to the valence band. Quickly electron loses its energy by generating heat and going to the state with lowest energy. Then, electron recombines with a hole in the valence band resulting to generate a photon. Energy of this photon is measured in a spectrometer. As is shown in Fig 1.11, the laser gets concentrated on the sample through a reflective objective. A He-Cd UV (325 nm) laser is used for PL excitation. The laser passes through optical density (OD) filters. OD filters are using to manipulate laser power to measure PL in different laser power which is called power dependent PL. The laser line filter blocks all wavelengths except 325 nm. The laser is reflected toward sample with a beam splitter. A reflective objective concentrates the light on the sample. There is a UV transparent window in front of the reflective objective which the laser goes through without any loss. The sample is located in a cryostat in which the temperature can be decreased to 15 K. The reflected light from the sample goes to the spectrometer, however, another splitter sends the light to a CCD camera which is focused on the sample. A long pass filter in front of the spectrometer allows photons with low energies go through spectrometer.

The advantages of using mirrors in PL set up are:

- Wavelength independent

- Low loss UV system (laser power is the same during propagation until hitting the sample)(Most glass absorbs laser)
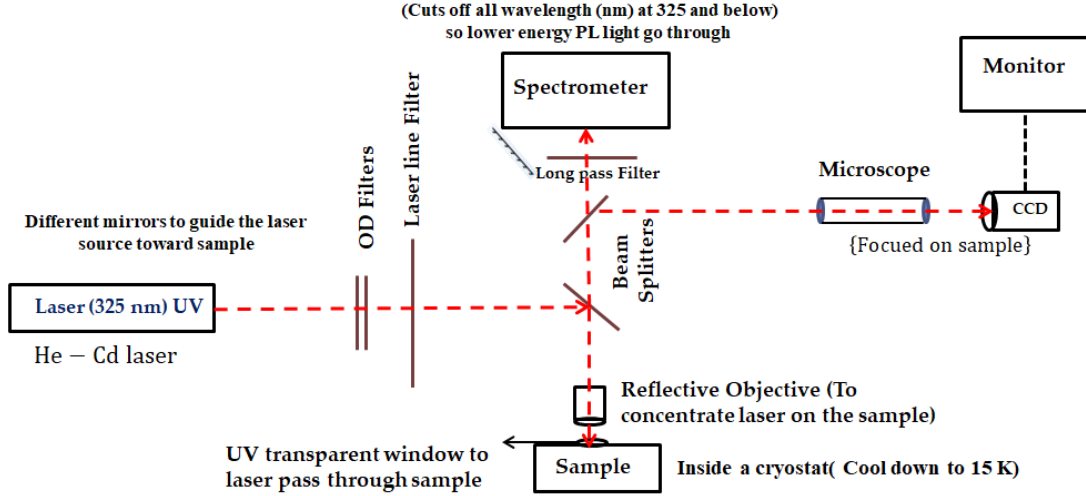
Figure 1. 11. Photoluminescence spectroscopy set up and components

To study the nature of each PL peak and recombination type correlated to each peak, power dependence PL was studied. The power of the laser is adjusted between 10 to 0.01 mW by using neutral density (ND) filters. ND filters are defined with their optical density (OD) which describes the amount of energy blocked by the filter.

Power law in PL explains, PL intensity relatively correlated to inserted carrier density for a constant spot of using light source which here is HeCd laser with 325 nm and initial 10 mw power.

$$I_{PL} = A \times I_{Laser}^{\alpha}$$ Equation 1. 11

For α<1, Free to bound transition & donor-acceptor pair recombination which is defined as transition between impurity and one of the energy bands or some neutral donor electrons recombine with neutral acceptor holes. For 1<α<2, it is called Shockley-Read-Hall (SRH) recombination which would occurs in either one or two step transition. An impurity due to a foreign atom or a structural defect is located within the bandgap causes SRH recombination which is considered as non-radiative. When α=1, it is called exciton transition when a bounded state of an electron and a hole which are attracted each other make an exciton.

When α=2 fFree carriers transition), it means an electron is free to fall down to the valence band (VB) to recombine with any hole.
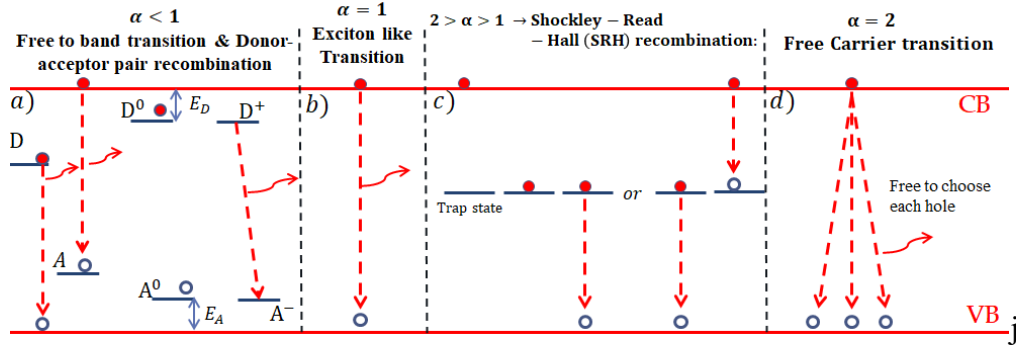
Figure 1. 12. Power law for different α; a) α<1, b) α=1, c) 1<α<2, d) α=2

To study the peak corresponded to the transition between ground state electron (hole) with other carriers, another PL study was reported. The experimental data were compared with simulation data. Simulation data confirm that the band to band transition and then recombination is due to ground state hole which recombines with all electrons in the conduction band. The transition probability vs energy gives the simulated PL which gets compared with experiment PL. For strained structures the result perfectly matches. On the other hand, for partially relaxed structures the experimental data is located between fully relaxed and fully strained simulation data.

In chapter 5 and 6, double graded structure solar cells are studied with nextnano software. An equation like Vegards law is defined to calculate the bandgap energy under strain. In addition, other parameters which are influenced by strain such as absorption coefficient and generation rate are obtained. In chapter 4, a Λ-shaped graded structure is studied in both features; strained to GaN lattice constant and relaxed. In chapter 5, A Flat Base Graded (FBG) InGaN solar cell structure is compared with two common InGaN structures; InGaN Homojunction and Square Well. In chapter 5, all structures are studied under strained to GaN lattice constant.

1.6 Nextnano software

Nextnano is a modeling software which can calculate, report and display semiconductor material (devices) optical and electrical properties in nano-scale. Nextnano solves Schrödinger, Poisson and current equations. Carriers are investigated within the effective mass approximation to find the quantization energies. Nextnano obtains the materials properties from its database. For group III-N materials theses information in the software are populated from Vurgaftman report for material properties [50]. In this modeling, graded well with ternary alloy (composition changes) between GaN to $In_{x_{max}}Ga_{1-x_{max}}N$ is assumed to changes linearly. Strain is considered in nextnano according to [98], bandgap energy of ternary alloys is calculated by interpolation between the binary alloys. For example for InGaN, conduction band and valence band energies are obtained by interpolation between GaN and InN as explained by Vegard's law earlier. Nextnano calculates and displays the optical and electrical properties of different semiconductor nanostructures. Due to the importance of strain in heterojunction semiconductor, strain gets solved separately from the main part of written program. Nextnano starts to calculate strain within continuum elastic approach. Effects of strain on conduction band and valence band are calculated by using band off set and deformation potential theory. Generally, strain is generated in crystal structure due lattice mismatch in the growth process, applied external force or stress to structure and phonon induced lattice vibration. Due to strain conduction band energy is shifted. To study and investigate conduction band energy shift, deformation potential theory was defined to calculate coupling between electrons and acoustic waves in solid. [99], [100] Then others [101] used this method to calculate transport in a semiconductor under strain. The deformation potential theory defines a new Hamiltonian $\mathcal{H}(\vec{\varepsilon})$. The effect of strain on crystal structure can be

18

studied by the new Hamiltonian. The Hamiltonian matrix elements are given below which is formed on first order perturbation energy.

$$\{\mathcal{H}(\vec{\varepsilon})\} = \sum_{\alpha,\beta=1}^{3} D_{ij}^{\alpha\beta} \varepsilon_{\alpha\beta}$$

<div align="right">Equation 1. 12</div>

$D^{\alpha\beta}$ is known as deformation potential operator which transforms under symmetry operation like a second rank tensor. [102] $\varepsilon_{\alpha\beta}$ is the strain tensor. In addition, ij indicates the matrix element of the operator $D^{\alpha\beta}$. Due to symmetry of strain tensor with respect to α and β, the deformation potential operator would follow this symmetry which means $D^{\alpha\beta} = D^{\beta\alpha}$. This fact decreases the number of independent deformation operators to six. Different methods performed to find the deformation potential constants. The methods such as empirical pseudo potential or ab initio can calculate deformation potential constants. Easier way is to fit the deformation potential to experimental results which are obtained by electrical, optical, microwave techniques or analyzing stress induced absorption edges. In spite of the fact that the theoretical prediction and measurements match well, deformation potential in literature and different methods vary from each other. Cubic crystal structures show induced energy shift for conduction band (for a degenerate energy level). Along the Δ symmetry line, $D^{\alpha\beta}$ (deformation potential operator) describes as scalar by one or two independent constants. The energy shift of the conduction band edge along the <111> and <100> directions is calculated by two independent deformation potential constants:

$$\delta E_0^{v_i} = \Xi_d^v \, Tr(\bar{\varepsilon}) + \Xi_u^v \, a_i^T \bar{\varepsilon} \, \vec{a}_i$$

<div align="right">Equation 1. 13</div>

Here, Ξ_u^v is uniaxial and Ξ_d^v is the dilatation deformation potential constants for valleys of the type $v = L, \Delta$. $\vec{a}_i$ is a unit vector parallel to $\vec{k}$ vector of valley i. The Γ conduction band minimum valley shift is calculated via a single deformation potential constant:

$$\delta E_0^\Gamma = \Xi_u^\Gamma Tr\ (\bar{\varepsilon})$$

Equation 1. 14

From the two above equations the valley splitting from uniaxial stress along arbitrary direction gets obtained. On the other hand, due to degeneracy at the maximum of the valence band, the deformation potential is different for the conduction band. $D^{\alpha\beta}$ isn't a scalar anymore and is described as a matrix 3*3. Due to symmetries the six independent operators are described through three independent entries, like *l,m,n* or *a,b,d* corresponded to set of eigenfuctions. For the basis $|x, s>, |y, s>, |z, s>$ with s=↑,↓ (spin state) the perturbation Hamiltonian is then defined as:

$$\bar{H}_{strain} = \begin{pmatrix} \bar{H} & 0_{3*3} \\ 0_{3*3} & \bar{H} \end{pmatrix}$$

Equation 1. 15

where $\bar{H}$ is a 3*3 matrix given by:

$$\bar{H} = \begin{cases} l\varepsilon_{xx} + m(\varepsilon_{yy} + \varepsilon_{zz}) & n\varepsilon_{xy} & n\varepsilon_{zx} \\ n\varepsilon_{xy} & l\varepsilon_{yy} + m(\varepsilon_{zz} + \varepsilon_{xx}) & n\varepsilon_{yx} \\ n\varepsilon_{zx} & n\varepsilon_{yz} & l\varepsilon_{zz} + m(\varepsilon_{xx} + \varepsilon_{yy}) \end{cases}$$

Then, the multi-band Schrödinger, Poisson and current equation get solved self-consistently. In addition, piezo and pyro-electric (spontaneous) charges are taken into account. Piezo-electric charges are created by strain. In addition, conduction band and valence band are influenced by strain. Moreover, strain influences the *k.p* Hamiltonian of the Schrödinger equation. The energy band diagram is obtained through a Poisson-solver or Schrodinger-solver. The Poisson equation explains electrostatics in a semiconductor device which is written as:

$$\varepsilon\nabla_x\varphi(x) = -\rho(x)$$

Equation 1. 16

where $\varphi(x)$ refers to the electrical potential and $\rho(x)$ is charge density. $\rho(x)$ contains carriers density and ionized concentration and is written as:

$$\rho(x) = q_0(p(x) - n(x) - N_a(x) + N_d(x))$$ Equation 1. 17

$n(x)$ and $p(x)$ are carrier densities (electrons and holes density respectively), N_a and N_b are

ionized donor and acceptor concentration.

At a given position x, the charge carrier density is given by:

$$n(x) = \int_{E_c}^{\infty} D_n(E, x) f_{FD}(E) dE$$ Equation 1. 18

$$p(x) = \int_{-\infty}^{E_v} D_p(E, x)(1 - f_{FD}(E)) dE$$ Equation 1. 19

where f_{FD} is the fermi Dirac distribution which shows the probability that the available state E is

occupied by electrons (holes) in the conduction (valence) band.

$$f_{FD}(E) = \frac{1}{1 + exp(\beta(E - E_f))}$$ Equation 1. 20

In addition, $D_n(E, x)$, $D_p(E, x)$ refer to Density of States (DOS) for electron and hole

respectively which are defined like:

$$D_n(E, x) = \sum_v \frac{g_v m_{n,v} v^{3/2}}{\hbar^2 \pi^2} \sqrt{2(E - E_c(x))}$$ Equation 1. 21

$$D_p(E, x) = \sum_v \frac{g_v m_{p,v} v^{3/2}}{\hbar^2 \pi^2} \sqrt{2(E_v(x) - E)}$$ Equation 1. 22

where $m_{n,v}$ and $m_{p,v}$. are effective masses of the electron and hole respectively, with degeneracy

of g_v where v indicates the valley index. E_c, E_v and E_f are conduction band valence band and

fermi energy. By considering the electrostatic potential $\varphi(x)$ in the conduction band $E_c(x)$ and

valence band $E_v(x)$, the VB and CB band edge are given as:

$$E_c(x) = E_{c,0} - q_0 \varphi(x)$$ Equation 1. 23

$$E_v(x) = E_{v,0} - q_0 \varphi(x)$$ Equation 1. 24

$E_{c,0}$ and $E_{v,0}$ refer to the conduction and valence band energy edge in flat band condition.

Poisson-solver solves equation 1.16-1.24 self consistent due to similar dependency of $\varphi(x)$, $p(x)$ and $n(x)$.

To explain the procedure of Poisson and Schrödinger-Poisson solver, two flow chart diagrams of newton iteration scheme are shown.
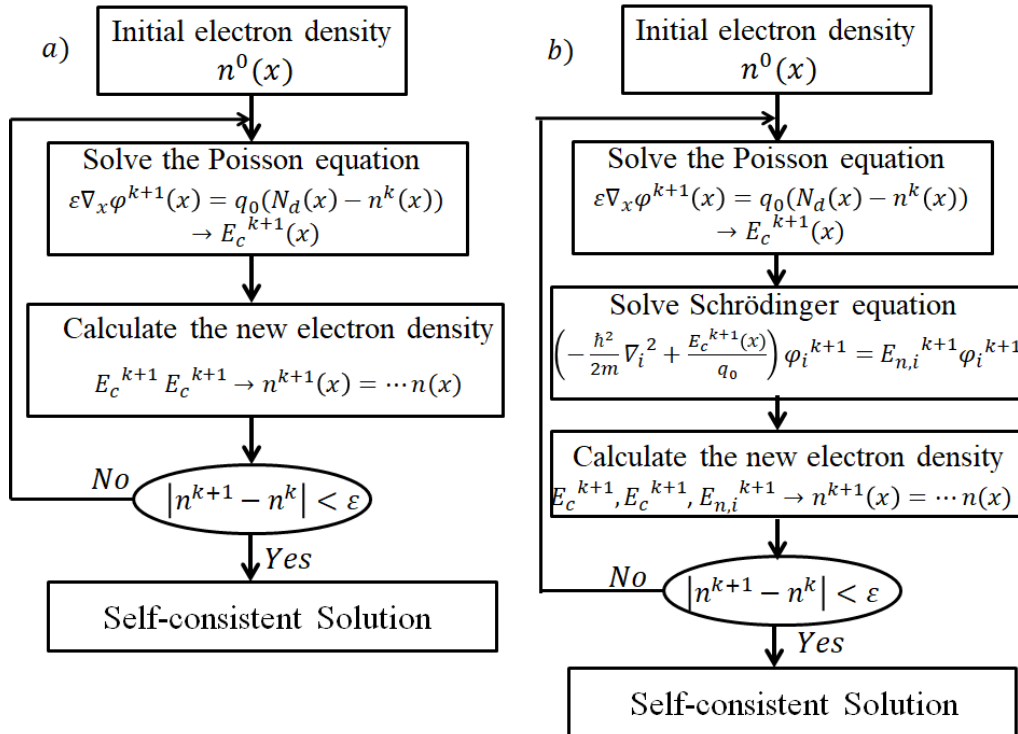
Figure 1. 13.a) Poisson and b) Poisson Schrodinger solving steps flow chart

As it's shown in Figure 1.13, the old electron density $n^k(x)$ enters to Poisson equation to obtain a new electrical potential $\varphi^{k+1}(x)$, then electron density $n^{k+1}(x)$ for this electrical potential gets calculated. The Poisson solver uses semi-classical equation $(n(x))$ to obtain new electron density. On the other hand, Schrödinger-Poisson equation determines bound state to study the new electron density $n^{k+1}(x)$. By obtaining new $n^{k+1}(x)$, the loop for iteration is continued at Poisson step until $|n^{k+1}(x) - n^k(x)|$ to decrease lower than a certain limit ε.

Carrier densities can get calculated by single quasi-bound states of electrons and holes:

$$n(x) = \int_{E_{n,0}}^{E_{lim,n}} \sum_v g_v \frac{m_{n,v,yz}}{\hbar^2 \pi} \sum_i \Theta\left(E - E_{n,i}\right)\left|\psi_{n,i}(x)\right|^2 f_{FD}(E) dE \qquad \text{Equation 1. 25}$$

$$p(x) = \int_{E_{lim,p}}^{E_{p,0}} \sum_v g_v \frac{m_{p,v,yz}}{\hbar^2 \pi} \sum_i \Theta\left(E - E_{p,i}\right)\left|\psi_{p,i}(x)\right|^2 \left(1 - f_{FD}(E)\right) dE \qquad \text{Equation 1. 26}$$

where Θ is defined as:

$$\Theta(x) = \begin{cases} 1, & x \geq 0 \\ 0, & x < 0 \end{cases} \qquad \text{Equation 1. 27}$$

$E_{n,i}$ is defined as energy of quasi-bound state i.and $\psi_{n,i}$ is the corresponding wave-function.

The single sub-bands of quasi-bound states add up to the electron DOS within the potential well which is between $E_c(x)$ and $E_{lim,n}$. For holes, the quasi-bound states $E_{p,i}$ with wave-function $\psi_{p,i}$ creates a sub-band between $E_v(x)$ and $E_{lim,p}$. For band diagram calculation, both Poisson and Schrodinger should be solved self-consistently because both are coupled through $\varphi(x)$ (electrostatic potential), *n(x)* and *p(x)* (charge carrier concentration) which were defined earlier. In a Schrodinger-Poisson solver, this system of coupled equations is treated using a self-consistent iteration method like given flow-chart on top.

The band structure is simulated in the envelope function approximation using a single-band effective mass approximation [103]. For a free electron the kinetic energy (*E*) is given by:

$$E = \frac{\hbar^2 k^2}{2m_0} = \frac{p^2}{2m_0} \qquad \text{Equation 1. 28}$$

where *k* is the wave vector, and *p* is momentum. The group velocity relating to energy and momentum is given by:

$$v_g = \frac{dE}{dp} = \frac{1}{\hbar}\frac{dE}{dk} \qquad \text{Equation 1. 29}$$

To study the electron dynamics in a lattice, effect of force on envelope function is investigated:

$$dE = Fdx = Fv_g dt \qquad \text{Equation 1. 30}$$

$$F = \frac{1}{v_g}\frac{dE}{dt} = \frac{1}{v_g}\frac{dE}{dk}\frac{dk}{dt} \qquad \text{Equation 1. 31}$$

$$v_g = \frac{dE}{dp} = \frac{1}{\hbar}\frac{dE}{dk} \qquad \text{Equation 1. 32}$$

$$\rightarrow F = \frac{d(\hbar k)}{dt} \qquad \text{Equation 1. 33}$$

Then, the acceleration is given by the time derivative of v_g:

$$a = \frac{dv_g}{dt} = \frac{1}{\hbar}\frac{d}{dt}\left(\frac{dE}{dk}\right) = \frac{1}{\hbar^2}\left(\frac{d^2E}{dk^2}\right)\frac{d(\hbar k)}{dt} \qquad \text{Equation 1. 34}$$

$$m^* = \frac{1}{\frac{1}{\hbar^2}\frac{d^2E}{dk^2}} \qquad \text{Equation 1. 35}$$

The electron acceleration in three dimensional crystals isn't isotropic so an effective mass tensor

is introduced as:

$$\frac{dv_g}{dt} = m_{xx}^{-1}F_x\hat{x} + m_{yx}^{-1}F_x\hat{y} + m_{zx}^{-1}F_x\hat{z} \qquad \text{Equation 1. 36}$$

$$\frac{1}{m^*} = \begin{matrix} m_{xx}^{-1} & m_{xy}^{-1} & m_{xz}^{-1} \\ m_{yx}^{-1} & m_{yy}^{-1} & m_{yz}^{-1} \\ m_{zx}^{-1} & m_{zy}^{-1} & m_{zz}^{-1} \end{matrix} \qquad \text{Equation 1. 37}$$

k-space is aligned to the main axes of the system centered at band edge. All off diagonal

components in m^* get eliminated and as an example with parabolic approximation the conduction

band effective mass can be approximated (m_e^*). According to E-k diagram for E, $\frac{dE}{dk}$ and $\frac{dE}{dk}$ in the

first BZ at $k=0$ for CB, it is shown that m_e^* is positive near the bottom of all bands and is

negative near the top of all bands.

For parabolic bands, the electron moves like a free particle with m^* which is related to the curvature of the band. When the band is not parabolic, m^* is not constant so the slope and curvature of *E-k* relationship should be taken to account to calculate v_g from *E* using Eq. 1.32.

$$E = E_c + \frac{\hbar^2 k^2}{2m_e^*} \qquad \text{Equation 1. 38}$$

$$E = E_v - \frac{\hbar^2 k^2}{2m_h^*} \qquad \text{Equation 1. 39}$$

For narrow bandgap semiconductors, the interaction between conduction band and valence band must be considered, so k.p perturbation theory is taken to account. Perturbation uses the fact that the cell periodic functions for the electrons for any $\vec{k}$ form a complete set which the wave function is written like:

$$\psi = \psi_{n\vec{k}}(\vec{r})\, exp(i\vec{k}.\vec{r}) = \left[\sum c_m U_{m\vec{k}_0}(r)\right] exp(i\vec{k}.\vec{r}) \qquad \text{Equation 1. 40}$$

By using ψ in the Schrödinger equation by considering that at $k=k_0$ wave-function can be written like:

$$\psi(k = k_0) = exp(i\vec{k}.\vec{r})\, U_{m.\vec{k}}(\vec{r}) \qquad \text{Equation 1. 41}$$

$$\left[-\frac{\hbar^2}{2m}\nabla^2 + \frac{\hbar}{m_0}\vec{k_0}.\vec{p} + \frac{\hbar^2 k^2}{2m_0} + V(\vec{r})\right] U_{m.\vec{k_0}}(r) = E_m(\vec{k_0}) U_{m.\vec{k_0}}(r) \qquad \text{Equation 1. 42}$$

$$E_m(\vec{k}) = E_m(0) + \frac{\hbar^2 k^2}{2m_0} + \left(\frac{\hbar}{m_0}\right)^2 \sum_{n \neq m} \frac{|\vec{k}.\hat{p}_{nm}|}{E_m(0) - E_n(0)} \qquad \text{Equation 1. 43}$$

1.7 References

[1]   "Perez, R. and M. Perez, (2009): A fundamental look at energy reserves for the planet. The International Energy Agency SHC Programme Solar Update, Volume 50, pp. 2-3, April 2009"

[2]   M. A. Green, "The path to 25% silicon solar cell efficiency: History of silicon cell evolution," Prog. Photovolt: Res. Appl., vol. 17, no. 3, pp. 183–189, May 2009, doi: 10.1002/pip.892.

[3]   M. A. Green, Y. Hishikawa, E. D. Dunlop, D. H. Levi, J. Hohl-Ebinger, and A. W. Y. Ho-Baillie, "Solar cell efficiency tables (version 51)," Prog Photovolt Res Appl, vol. 26, no. 1, pp. 3–12, Jan. 2018, doi: 10.1002/pip.2978.

[4]   K. Masuko et al., "Achievement of More Than 25% Conversion Efficiency With Crystalline Silicon Heterojunction Solar Cell," IEEE J. Photovoltaics, vol. 4, no. 6, pp. 1433–1435, Nov. 2014, doi: 10.1109/JPHOTOV.2014.2352151.

[5]   W. Shockley and H. J. Queisser, "Detailed Balance Limit of Efficiency of *p-n* Junction Solar Cells," *Journal of Applied Physics*, vol. 32, no. 3, pp. 510–519, Mar. 1961, doi: 10.1063/1.1736034.

 [6]   M. T. Kibria, A. Ahammed, S. M. Sony, and F. Hossain, ""A Review : Comparative studies on different generation solar cells technology"," Int. Conf. Environ. Asp. Bangladesh, pp. 51–53, 2014.

[7]   G. Conibeer, "Third-generation photovoltaics," Materials Today, vol. 10, no. 11, pp. 42–50, Nov. 2007, doi: 10.1016/S1369-7021(07)70278-X.

[8]   I. Almansouri, A. Ho-Baillie, S. P. Bremner, and M. A. Green, "Supercharging Silicon Solar Cell Performance by Means of Multijunction Concept," IEEE J. Photovoltaics, vol. 5, no. 3, pp. 968–976, May 2015, doi: 10.1109/JPHOTOV.2015.2395140.

[9]   X. Li et al., "Silicon heterojunction-based tandem solar cells: past, status, and future prospects," Nanophotonics, vol. 10, no. 8, pp. 2001–2022, Jun. 2021, doi: 10.1515/nanoph-2021-0034.

[10]   M. Yamaguchi, K.-H. Lee, K. Araki, and N. Kojima, "A review of recent progress in heterogeneous silicon tandem solar cells," J. Phys. D: Appl. Phys., vol. 51, no. 13, p. 133002, Apr. 2018, doi: 10.1088/1361-6463/aaaf08.

[11]   N. Yastrebova, "High-efficiency multi-junction solar cells : Current status and future potential,", 2008, Accessed: Jun. 23, 2022. [Online]. Available: http://sunlab.site.uottawa.ca/pdf/whitepapers/HiEfficMjSc-CurrStatus&FuturePotential.pdf

[12]   M. A. Green, "Third generation photovoltaics: Ultra-high conversion efficiency at low cost," Prog. Photovolt: Res. Appl., vol. 9, no. 2, pp. 123–135, Mar. 2001, doi: 10.1002/pip.360.

[13]   J. P. Connolly et al., "Simulating multiple quantum well solar cells," in Conference Record of the Twenty-Eighth IEEE Photovoltaic Specialists Conference - 2000 (Cat. No.00CH37036), Anchorage, AK, USA, 2000, pp. 1304–1307. doi: 10.1109/PVSC.2000.916130.

[14]   X. Huang et al., "Energy band engineering of InGaN/GaN multi-quantum-well solar cells via AlGaN electron- and hole-blocking layers," Appl. Phys. Lett., vol. 113, no. 4, p. 043501, Jul. 2018, doi: 10.1063/1.5028530.

[15]   G. Moses, X. Huang, Y. Zhao, M. Auf der Maur, E. A. Katz, and J. M. Gordon, "InGaN/GaN multi-quantum-well solar cells under high solar concentration and elevated temperatures for hybrid solar thermal-photovoltaic power plants," Prog Photovolt Res Appl, vol. 28, no. 11, pp. 1167–1174, Nov. 2020, doi: 10.1002/pip.3326.

[16]   I. Sayed and S. M. Bedair, "Quantum Well Solar Cells: Principles, Recent Progress, and Potential," IEEE J. Photovoltaics, vol. 9, no. 2, pp. 402–423, Mar. 2019, doi: 10.1109/JPHOTOV.2019.2892079.

[17]   S. Watanabe et al., "Two-step photocurrent generation enhanced by miniband formation in InAs/GaAs quantum dot superlattice intermediate-band solar cells," Appl. Phys. Lett., vol. 110, no. 19, p. 193104, May 2017, doi: 10.1063/1.4983288.

[18]   R. E. Welser, S. J. Polly, M. Kacharia, A. Fedorenko, A. K. Sood, and S. M. Hubbard, "Design and Demonstration of High-Efficiency Quantum Well Solar Cells Employing Thin Strained Superlattices," Sci Rep, vol. 9, no. 1, p. 13955, Dec. 2019, doi: 10.1038/s41598-019-50321-x.

[19]   X. Chen, K. D. Matthews, D. Hao, W. J. Schaff, and L. F. Eastman, "Growth, fabrication, and characterization of InGaN solar cells," phys. stat. sol. (a), vol. 205, no. 5, pp. 1103–1105, May 2008, doi: 10.1002/pssa.200778695.

[20]   B. Chouchen, M. H. Gazzah, A. Bajahzar, and H. Belmabrouk, "Numerical modeling of InGaN/GaN p-i-n solar cells under temperature and hydrostatic pressure effects," AIP Advances, vol. 9, no. 4, p. 045313, Apr. 2019, doi: 10.1063/1.5092236.

[21]   C. J. Neufeld, N. G. Toledo, S. C. Cruz, M. Iza, S. P. DenBaars, and U. K. Mishra, "High quantum efficiency InGaN/GaN solar cells with 2.95 eV band gap," Appl. Phys. Lett., vol. 93, no. 14, p. 143502, Oct. 2008, doi: 10.1063/1.2988894.

[22]   K. Wang et al., "P-type InGaN across the entire alloy composition range," Appl. Phys. Lett., vol. 102, no. 10, p. 102111, Mar. 2013, doi: 10.1063/1.4795718.

[23]   R. Belghouthi, J. P. Salvestrini, M. H. Gazzeh, and C. Chevallier, "Analytical modeling of polarization effects in InGaN double hetero-junction p-i-n solar cells," Superlattices and Microstructures, vol. 100, pp. 168–178, Dec. 2016, doi: 10.1016/j.spmi.2016.09.016.

[24]   B. Monemar and B. E. Sernelius, "Defect related issues in the 'current roll-off' in InGaN based light emitting diodes," Appl. Phys. Lett., vol. 91, no. 18, p. 181103, Oct. 2007, doi: 10.1063/1.2801704.

[25]   C. G. Van de Walle and D. Segev, "Microscopic origins of surface states on nitride surfaces," Journal of Applied Physics, vol. 101, no. 8, p. 081704, Apr. 2007, doi: 10.1063/1.2722731.

[26]   J. W. L. Yim et al., "Effects of surface states on electrical characteristics of InN and In 1 − x Ga x N," Phys. Rev. B, vol. 76, no. 4, p. 041303, Jul. 2007, doi: 10.1103/PhysRevB.76.041303.

[27]   T. Narita et al., "Progress on and challenges of p-type formation for GaN power devices," Journal of Applied Physics, vol. 128, no. 9, p. 090901, Sep. 2020, doi: 10.1063/5.0022198.

[28]   S. Brochen, J. Brault, S. Chenot, A. Dussaigne, M. Leroux, and B. Damilano, "Dependence of the Mg-related acceptor ionization energy with the acceptor concentration in p-type GaN layers grown by molecular beam epitaxy," Appl. Phys. Lett., vol. 103, no. 3, p. 032102, Jul. 2013, doi: 10.1063/1.4813598.

[29]   J. Wu et al., "Small band gap bowing in In1−xGaxN alloys," Appl. Phys. Lett., vol. 80, no. 25, pp. 4741–4743, Jun. 2002, doi: 10.1063/1.1489481.

[30]   J. Wu et al., "Superior radiation resistance of In1−xGaxN alloys: Full-solar-spectrum photovoltaic material system," Journal of Applied Physics, vol. 94, no. 10, pp. 6477–6482, Nov. 2003, doi: 10.1063/1.1618353.

[31]   X. M. Cai et al., "Study of InGaN/GaN Multiple Quantum Well Solar Cells With Different Barrier Thicknesses," physica status solidi (a), vol. 215, no. 10, p. 1700581, May 2018, doi: 10.1002/pssa.201700581.

[32]   S. R. Routray and T. R. Lenka, "InGaN-based solar cells: a wide solar spectrum harvesting technology for twenty-first century," CSI Transactions on ICT, vol. 6, no. 1, pp. 83–96, Mar. 2018, doi: 10.1007/s40012-017-0181-9.

[33]   E. Vadiee et al., "InGaN solar cells with regrown GaN homojunction tunnel contacts," Applied Physics Express, vol. 11, no. 8, p. 082304, Aug. 2018, doi: 10.7567/APEX.11.082304.

[34]   J. Wu, "When group-III nitrides go infrared: New properties and perspectives," Journal of Applied Physics, vol. 106, no. 1, p. 011101, Jul. 2009, doi: 10.1063/1.3155798.

[35]   Z. Fang and C. Z. Zhao, "Recent Progress in Silicon Photonics: A Review," ISRN Optics, vol. 2012, pp. 1–27, Mar. 2012, doi: 10.5402/2012/428690.

[36]   K.-C. Shen, T.-Y. Wang, D.-S. Wuu, and R.-H. Horng, "High indium content InGaN films grown by pulsed laser deposition using a dual-compositing target," Opt. Express, vol. 20, no. 14, p. 15149, Jul. 2012, doi: 10.1364/OE.20.015149.

[37]   D.-H. Lien et al., "Harsh photovoltaics using InGaN/GaN multiple quantum well schemes," Nano Energy, vol. 11, pp. 104–109, Jan. 2015, doi: 10.1016/j.nanoen.2014.10.013.

[38]   L. Hsu and W. Walukiewicz, "Modeling of InGaN/Si tandem solar cells," Journal of Applied Physics, vol. 104, no. 2, p. 024507, Jul. 2008, doi: 10.1063/1.2952031.

[39]   M. Kurouchi, T. Araki, H. Naoi, T. Yamaguchi, A. Suzuki, and Y. Nanishi, "Growth and properties of In-rich InGaN films grown on (0001) sapphire by RF-MBE," phys. stat. sol. (b), vol. 241, no. 12, pp. 2843–2848, Oct. 2004, doi: 10.1002/pssb.200405121.

[40]   M. D. McCluskey, C. G. Van de Walle, C. P. Master, L. T. Romano, and N. M. Johnson, "Large band gap bowing of InxGa1−xN alloys," Appl. Phys. Lett., vol. 72, no. 21, pp. 2725–2726, May 1998, doi: 10.1063/1.121072.

[41]   M. Moret et al., "Optical, structural investigations and band-gap bowing parameter of GaInN alloys," Journal of Crystal Growth, vol. 311, no. 10, pp. 2795–2797, May 2009, doi: 10.1016/j.jcrysgro.2009.01.009.

[42]   J. Wu, "When group-III nitrides go infrared: New properties and perspectives," Journal of Applied Physics, vol. 106, no. 1, p. 011101, Jul. 2009, doi: 10.1063/1.3155798.

[43]   S. N. Alam, V. Z. Zubialevich, B. Ghafary, and P. J. Parbrook, "Bandgap and refractive index estimates of InAlN and related nitrides across their full composition ranges," Sci Rep, vol. 10, no. 1, p. 16205, Dec. 2020, doi: 10.1038/s41598-020-73160-7.

[44]   M. A. Caro, S. Schulz, and E. P. O'Reilly, "Theory of local electric polarization and its relation to internal strain: Impact on polarization potential and electronic properties of group-III nitrides," Phys. Rev. B, vol. 88, no. 21, p. 214103, Dec. 2013, doi: 10.1103/PhysRevB.88.214103.

[45]   P. G. Moses, M. Miao, Q. Yan, and C. G. Van de Walle, "Hybrid functional investigations of band gaps and band alignments for AlN, GaN, InN, and InGaN," The Journal of Chemical Physics, vol. 134, no. 8, p. 084703, Feb. 2011, doi: 10.1063/1.3548872.

[46]   F. Bouzid and L. Hamlaoui, "Investigation of InGaN/Si double junction tandem solar cells," J. Fundam and Appl Sci., vol. 4, no. 2, p. 108, Sep. 2015, doi: 10.4314/jfas.v4i2.1.

[47]   A. Mesrane, F. Rahmoune, A. Mahrane, and A. Oulebsir, "Design and Simulation of InGaN p - n Junction Solar Cell," International Journal of Photoenergy, vol. 2015, pp. 1–9, 2015, doi: 10.1155/2015/594858.

[48]   M. Nawaz and A. Ahmad, "A TCAD-based modeling of GaN/InGaN/Si solar cells," Semicond. Sci. Technol., vol. 27, no. 3, p. 035019, Mar. 2012, doi: 10.1088/0268-1242/27/3/035019.

[49]   J. Wu et al., "Small band gap bowing in In1−xGaxN alloys," Appl. Phys. Lett., vol. 80, no. 25, pp. 4741–4743, Jun. 2002, doi: 10.1063/1.1489481.

[50]   I. Vurgaftman and J. R. Meyer, "Band parameters for nitrogen-containing semiconductors," Journal of Applied Physics, vol. 94, no. 6, pp. 3675–3696, Sep. 2003, doi: 10.1063/1.1600519.

[51]   I. Vurgaftman, J. R. Meyer, and L. R. Ram-Mohan, "Band parameters for III–V compound semiconductors and their alloys," Journal of Applied Physics, vol. 89, no. 11, pp. 5815–5875, Jun. 2001, doi: 10.1063/1.1368156.

[52]   Y. El Gmili et al., "Multilayered InGaN/GaN structure vs. single InGaN layer for solar cell applications: A comparative study," Acta Materialia, vol. 61, no. 17, pp. 6587–6596, Oct. 2013, doi: 10.1016/j.actamat.2013.07.041.

[53]   S.-W. Feng, C.-M. Lai, C.-Y. Tsai, Y.-R. Su, and L.-W. Tu, "Modeling of InGaN p-n junction solar cells," Optical Materials Express, vol. 3, no. 10, p. 1777, Oct. 2013, doi: 10.1364/OME.3.001777.

[54]   Q. Deng et al., "An investigation on In x Ga $1-x$ N/GaN multiple quantum well solar cells," J. Phys. D: Appl. Phys., vol. 44, no. 26, p. 265103, Jul. 2011, doi: 10.1088/0022-3727/44/26/265103.

[55]   R. Dahal, B. Pantha, J. Li, J. Y. Lin, and H. X. Jiang, "InGaN/GaN multiple quantum well solar cells with long operating wavelengths," Applied Physics Letters, vol. 94, no. 6, p. 063505, Feb. 2009, doi: 10.1063/1.3081123.

[56]   R. Dahal, B. Pantha, J. Li, J. Y. Lin, and H. X. Jiang, "InGaN/GaN multiple quantum well solar cells with long operating wavelengths," Applied Physics Letters, vol. 94, no. 6, p. 063505, Feb. 2009, doi: 10.1063/1.3081123.

[57]   R. Singh, D. Doppalapudi, T. D. Moustakas, and L. T. Romano, "Phase separation in InGaN thick films and formation of InGaN/GaN double heterostructures in the entire alloy composition," Applied Physics Letters, vol. 70, no. 9, pp. 1089–1091, Mar. 1997, doi: 10.1063/1.118493.

[58]   A. Tabata et al., "Phase separation suppression in InGaN epitaxial layers due to biaxial strain," Applied Physics Letters, vol. 80, no. 5, pp. 769–771, Feb. 2002, doi: 10.1063/1.1436270.

[59]   N. Miller et al., "Low-temperature grown compositionally graded InGaN films," phys. stat. sol. (c), vol. 5, no. 6, pp. 1866–1869, May 2008, doi: 10.1002/pssc.200778719.

[60]   Md. A. Hossain, Md. R. Islam, M. K. Hossain, A. Hashimoto, and A. Yamamoto, "Dislocation reduction in heteroepitaxial In x Ga1-xN using step-graded interlayer for future solar cells," Mater Renew Sustain Energy, vol. 3, no. 1, p. 20, Mar. 2014, doi: 10.1007/s40243-013-0020-3.

[61]   E. S. Hellman, "The Polarity of GaN: a Critical Review," MRS Internet j. nitride semicond. res., vol. 3, p. e11, 1998, doi: 10.1557/S1092578300000831.

[62]   F. Bernardini, V. Fiorentini, and D. Vanderbilt, "Spontaneous polarization and piezoelectric constants of III-V nitrides," Phys. Rev. B, vol. 56, no. 16, pp. R10024–R10027, Oct. 1997, doi: 10.1103/PhysRevB.56.R10024.

[63]   R. Belghouthi, S. Taamalli, F. Echouchene, H. Mejri, and H. Belmabrouk, "Modeling of polarization charge in N-face InGaN/GaN MQW solar cells," Materials Science in Semiconductor Processing, vol. 40, pp. 424–428, Dec. 2015, doi: 10.1016/j.mssp.2015.07.009.

[64]   R. Belghouthi and M. Aillerie, "Temperature Dependence of InGaN / GaN Multiple Quantum Well Solar Cells," Energy Procedia, vol. 157, pp. 793–801, Jan. 2019, doi: 10.1016/j.egypro.2018.11.245.

[65]   Y. Zhang, Y. Yang, and Z. L. Wang, "Piezo-phototronics effect on nano/microwire solar cells," Energy Environ. Sci., vol. 5, no. 5, p. 6850, 2012, doi: 10.1039/c2ee00057a.

[66]   C. J. Neufeld et al., "Effect of doping and polarization on carrier collection in InGaN quantum well solar cells," Appl. Phys. Lett., vol. 98, no. 24, p. 243507, Jun. 2011, doi: 10.1063/1.3595487.

[67]   Y. Kuwahara et al., "Realization of Nitride-Based Solar Cell on Freestanding GaN Substrate," Appl. Phys. Express, vol. 3, no. 11, p. 111001, Oct. 2010, doi: 10.1143/APEX.3.111001.

[68]   N. G. Young et al., "High performance thin quantum barrier InGaN/GaN solar cells on sapphire and bulk (0001) GaN substrates," Appl. Phys. Lett., vol. 103, no. 17, p. 173903, Oct. 2013, doi: 10.1063/1.4826483.

[69]   U. K. Kumawat, K. Kumar, P. Bhardwaj, and A. Dhawan, "Indium-rich InGaN/GaN solar cells with improved performance due to plasmonic and dielectric nanogratings," Energy Sci Eng, vol. 7, no. 6, pp. 2469–2482, Dec. 2019, doi: 10.1002/ese3.436.

[70]   A. Yamamoto, Md. T. Hasan, A. Mihara, N. Narita, N. Shigekawa, and M. Kuzuhara, "Phase separation of thick (~1 µm) In x Ga 1− x N (x ∼ 0.3) grown on AlN/Si(111): Simultaneous emergence of metallic In–Ga and GaN-rich InGaN," Appl. Phys. Express, vol. 7, no. 3, p. 035502, Mar. 2014, doi: 10.7567/APEX.7.035502.

[71]   R. Singh, D. Doppalapudi, T. D. Moustakas, and L. T. Romano, "Phase separation in InGaN thick films and formation of InGaN/GaN double heterostructures in the entire alloy composition," Applied Physics Letters, vol. 70, no. 9, pp. 1089–1091, Mar. 1997, doi: 10.1063/1.118493.

[72]   C. J. Lu, L. A. Bendersky, H. Lu, and W. J. Schaff, "Threading dislocations in epitaxial InN thin films grown on (0001) sapphire with a GaN buffer layer," Appl. Phys. Lett., vol. 83, no. 14, pp. 2817–2819, Oct. 2003, doi: 10.1063/1.1616659.

[73]   D. Holec, Y. Zhang, D. V. S. Rao, M. J. Kappers, C. McAleese, and C. J. Humphreys, "Equilibrium critical thickness for misfit dislocations in III-nitrides," Journal of Applied Physics, vol. 104, no. 12, p. 123514, Dec. 2008, doi: 10.1063/1.3033553.

[74]   A. V. Lobanova, A. L. Kolesnikova, A. E. Romanov, S. Yu. Karpov, M. E. Rudinsky, and E. V. Yakovlev, "Mechanism of stress relaxation in (0001) InGaN/GaN via formation of V-shaped dislocation half-loops," Appl. Phys. Lett., vol. 103, no. 15, p. 152106, Oct. 2013, doi: 10.1063/1.4824835.

[75]   A. S. Yusof et al., "The dependence of indium incorporation on specified temperatures in growing InGaN/GaN heterostructure using MOCVD technique," Materials Research Bulletin, vol. 137, p. 111176, May 2021, doi: 10.1016/j.materresbull.2020.111176.

[76]   I.-H. Kim, H.-S. Park, Y.-J. Park, and T. Kim, "Formation of V-shaped pits in InGaN/GaN multiquantum wells and bulk InGaN films," Appl. Phys. Lett., vol. 73, no. 12, pp. 1634–1636, Sep. 1998, doi: 10.1063/1.122229.

[77]   H. Hu, S. Zhou, H. Wan, X. Liu, N. Li, and H. Xu, "Effect of strain relaxation on performance of InGaN/GaN green LEDs grown on 4-inch sapphire substrate with sputtered AlN nucleation layer," Sci Rep, vol. 9, no. 1, p. 3447, Dec. 2019, doi: 10.1038/s41598-019-40120-9.

[78]   A. Even et al., "Enhanced In incorporation in full InGaN heterostructure grown on relaxed InGaN pseudo-substrate," Appl. Phys. Lett., vol. 110, no. 26, p. 262103, Jun. 2017, doi: 10.1063/1.4989998.

[79]   K. Chung, J. Sui, B. Demory, C.-H. Teng, and P.-C. Ku, "Monolithic integration of individually addressable light-emitting diode color pixels," Appl. Phys. Lett., vol. 110, no. 11, p. 111103, Mar. 2017, doi: 10.1063/1.4978554.

[80]   K. Lekhal et al., "Strain-compensated (Ga,In)N/(Al,Ga)N/GaN multiple quantum wells for improved yellow/amber light emission," Appl. Phys. Lett., vol. 106, no. 14, p. 142101, Apr. 2015, doi: 10.1063/1.4917222.

[81]   K. Lekhal et al., "Optimized In composition and quantum well thickness for yellow-emitting (Ga,In)N/GaN multiple quantum wells," Journal of Crystal Growth, vol. 434, pp. 25–29, Jan. 2016, doi: 10.1016/j.jcrysgro.2015.10.026.

[82]   Q. Li et al., "Optical performance of top-down fabricated InGaN/GaN nanorod light emitting diode arrays," Opt. Express, vol. 19, no. 25, p. 25528, Dec. 2011, doi: 10.1364/OE.19.025528.

[83]   M. Liu et al., "An InGaN/GaN Superlattice to Enhance the Performance of Green LEDs: Exploring the Role of V-Pits," Nanomaterials, vol. 8, no. 7, p. 450, Jun. 2018, doi: 10.3390/nano8070450.

[84]   D. Teng, M. Wu, L. Liu, and G. Wang, "Size- and current-density-controlled tunable wavelength in gan-based leds for potential dense wavelength-division multiplexing application," IEEE Wireless Commun., vol. 22, no. 2, pp. 74–79, Apr. 2015, doi: 10.1109/MWC.2015.7096288.

[85]   T. Wang, "Topical Review: Development of overgrown semi-polar GaN for high efficiency green/yellow emission," Semicond. Sci. Technol., vol. 31, no. 9, p. 093003, Sep. 2016, doi: 10.1088/0268-1242/31/9/093003.

[86]   Z.-H. Zhang et al., "InGaN/GaN multiple-quantum-well light-emitting diodes with a grading InN composition suppressing the Auger recombination," Appl. Phys. Lett., vol. 105, no. 3, p. 033506, Jul. 2014, doi: 10.1063/1.4891334.

[87]   H. Obloh et al., "Self-compensation in Mg doped p-type GaN grown by MOCVD," Journal of Crystal Growth, vol. 195, no. 1–4, pp. 270–273, Dec. 1998, doi: 10.1016/S0022-0248(98)00578-8.

[88]   S. Yamasaki et al., "p -type conduction in Mg-doped Ga 0.91 In 0.09 N grown by metalorganic vapor-phase epitaxy," Appl. Phys. Lett., vol. 66, no. 9, pp. 1112–1113, Feb. 1995, doi: 10.1063/1.113829.

[89]   O. Jani, I. Ferguson, C. Honsberg, and S. Kurtz, "Design and characterization of GaN∕InGaN solar cells," Appl. Phys. Lett., vol. 91, no. 13, p. 132117, Sep. 2007, doi: 10.1063/1.2793180.

[90]   X. Zheng et al., "High-quality InGaN∕GaN heterojunctions and their photovoltaic effects," Appl. Phys. Lett., vol. 93, no. 26, p. 261108, Dec. 2008, doi: 10.1063/1.3056628.

[91]   S. D. Burnham, G. Namkoong, D. C. Look, B. Clafin, and W. A. Doolittle, "Reproducible increased Mg incorporation and large hole concentration in GaN using metal modulated epitaxy," Journal of Applied Physics, vol. 104, no. 2, p. 024902, Jul. 2008, doi: 10.1063/1.2953089.

[92]   G. F. Brown, J. W. Ager, W. Walukiewicz, and J. Wu, "Finite element simulations of compositionally graded InGaN solar cells," Solar Energy Materials and Solar Cells, vol. 94, no. 3, pp. 478–483, Mar. 2010, doi: 10.1016/j.solmat.2009.11.010.

[93]   A. Y. Cho, "How molecular beam epitaxy (MBE) began and its projection into the future," Journal of Crystal Growth, vol. 201–202, pp. 1–7, May 1999, doi: 10.1016/S0022-0248(98)01265-2.

[94]   F. Rinaldi, "Basics of Molecular Beam Epitaxy (MBE)," 2003. https://www.semanticscholar.org/paper/Basics-of-Molecular-Beam-Epitaxy-(-MBE-)-Rinaldi/c4b463caba1e85265210a62b5cb42b8dba4ce0fd (accessed Feb. 21, 2022).

[95]   A. Chambers, Modern vacuum physics. Boca Raton, Fla.: Chapman & Hall/CRC Press, 2005.

[96]   J. M. Lafferty and J. M. Lafferty, Eds., Foundations of vacuum science and technology. New York, NY: Wiley, 1998.

[97]   S. Li et al., "Polarization induced pn-junction without dopant in graded AlGaN coherently strained on GaN," Appl. Phys. Lett., vol. 101, no. 12, p. 122103, Sep. 2012, doi: 10.1063/1.4753993.

[98]   M. P. C. M. Krijn, "Heterojunction band offsets and effective masses in III-V quaternary alloys," Semicond. Sci. Technol., vol. 6, no. 1, pp. 27–31, Jan. 1991, doi: 10.1088/0268-1242/6/1/005.

[99]   W. Shockley and J. Bardeen, "Energy Bands and Mobilities in Monatomic Semiconductors," Phys. Rev., vol. 77, no. 3, pp. 407–408, Feb. 1950, doi: 10.1103/PhysRev.77.407.

[100]   J. Bardeen and W. Shockley, "Deformation Potentials and Mobilities in Non-Polar Crystals," Phys. Rev., vol. 80, no. 1, pp. 72–80, Oct. 1950, doi: 10.1103/PhysRev.80.72.

[101]   C. Herring and E. Vogt, "Transport and Deformation-Potential Theory for Many-Valley Semiconductors with Anisotropic Scattering," Phys. Rev., vol. 101, no. 3, pp. 944–961, Feb. 1956, doi: 10.1103/PhysRev.101.944.

[102]   J. M. Hinckley and J. Singh, "Influence of substrate composition and crystallographic orientation on the band structure of pseudomorphic Si-Ge alloy films," Phys. Rev. B, vol. 42, no. 6, pp. 3546–3566, Aug. 1990, doi: 10.1103/PhysRevB.42.3546.

[103]   "qcl:electronic_band_structure [nextnano.NEGF - Software for Quantum Transport]." https://nextnano-docu.northeurope.cloudapp.azure.com/dokuwiki/doku.php?id=qcl:electronic_band_structure (accessed Oct. 05, 2021).

CHAPTER 2

Luminescence properties of GaN/In$_x$Ga$_{1-x}$N/In$_y$Ga$_{1-y}$N double graded structures (zig-zag quantum wells)

Authors: Mirsaeid Sarollahi, Pijush K Ghosh, Manal A. Aldawsari , Andrian Kuchuk,

Morgan.E.Ware

2.1 Abstract

We have designed graded InGaN quantum well (QW) structures with the In composition increasing then decreasing in a zig-zag pattern. Through polarization doping, this naturally creates a p-n junction. Separate structures are designed by varying the maximum In composition but maintaining a constant QW thickness. This is both in order to test the limits of the molecular beam epitaxy growth control in terms of the deposition source ramping rates and to determine the limits of the maximum In composition within a narrow QW. The composition, x, of In$_x$Ga$_{1-x}$N is varied for all structures starting from a minimum of x_{min} = ~3%, and increasing to different maximum compositions, x_{max}, then finally decreased back to ~3%. The samples are characterized for their structural and luminescent properties. The results of the photoluminescence studies on samples with x_{max} ranging up to 35% demonstrate broadband emission covering wavelengths between 380 and 700nm. Additionally, although the general emission of structures with increasing x_{max} shifts to lower energy, the observed luminescence is comprised of several individual peaks which are currently being investigated as to their particular origin.

2.2 Introduction

An important class of materials for current solid state lighting technologies is the InGaN ternary alloy [1]–[3]. In addition, a direct and tunable bandgap covering the entire range of the solar spectrum along with high thermal conductivity, high optical absorption, and high radiation

resistance [4] make InGaN very interesting for applications in the photovoltaics industry. As a result, InGaN continues to receive attention in the research community both fundamentally and with a strong push towards photovoltaics [5]–[9].At the same time, there have been several reports in which strain is claimed to suppress phase separation in InxGa1-xN alloys. It was claimed that InGaN alloys across the entire composition range without phase separation can be grown when the layer is located within an InGaN/GaN double heterostructure [10]–[12]. Therefore, more complex structures may be possible. In Ref. (13) multiple graded quantum wells (GQWs), where each QW was formed by a single grade from *GaN* to *$In_xGa_{1-x}N$*, or the reverse, were grown in a device structure in order to improve the efficiency droop as well as study the polarization field effect on the efficiency droop in light emitting diodes (LEDs). The initial results indicate the quantum efficiency using a GQW structure is higher than that for a typical LED structure. It was determined that efficiency droop due to electron leakage for high current injection levels was reduced in the GQW LED due to the reduction in polarization field in the active layer. Additionally, it was shown that multiple InGaN GQWs show improved overlap of the electron and hole wave functions in the active layer, while also creating a barrier to prevent carrier overflow for high injection currents [13]. Graded-composition multiple quantum barriers (GQB) were also introduced to improve the hole transfer to the active layer and reduce efficiency droop. This, again resulted in improved electron and hole overlap and in improved light output power and internal quantum efficiency (IQE) of LEDs [14]–[15]. Several additional groups have similarly reported improved electron and hole wave-function overlap in the active regions using similar graded structures [16]–[19]. The reduced charge separation improves the IQE. Using a graded structure in QWs also allows for the design of a wider well in order to reduce carrier densities and similarly non-radiative recombination through Auger recombination. Such a

36

mechanism becomes important in reducing LED efficiency droop [20],[21] when carrier densities become large. In commercial (InGaN/GaN) QW LEDs the abrupt InGaN well is limited to 3 nm due to crystal quality consideration. In graded structures of InGaN the thickness was increased to 5 nm which allows for higher light output power. Using GQWs also reduces the polarization-induced interface charge density. In a typical MQW LED the polarization-induced interface charge density was about $0.54*10^{17}$ e/m^2, whereas for similar graded structures it was $0.3*10^{17}$ e/m^2. At the same time, the graded structure creates a bulk charge density in the well which will screen the electric field. So, the electric field inside the well becomes screened. This reduces the effects of the quantum confined Stark effect, which normally acts to pull apart electrons and holes reducing light emission. It was also confirmed that the electron-hole wave-function overlap increases along with the optical recombination in graded structures in comparison with typical quantum wells [22].

Generally (striking) while, GaN and InN have different spontaneous crystal polarizations, P, resulting from the non-centrosymmetric nature of their wurtzite structures. In a compositionally graded structure of InGaN, the polarization changes proportionally to the changing composition resulting in a fixed charge field given by, $-\nabla \cdot P = \rho < 0$. Grading the composition from GaN to $In_xGa_{1-x}N$ results in a negative charge field and attracts free holes for *p-type* doping. While the reverse grading, $In_xGa_{1-x}N$ to GaN, results in a positive polarization charge and attracts free electrons for n-type doping [23]. It has been demonstrated that AlN polarization charge fields are reversed in comparison with InN. In other words, by increasing the aluminum composition from GaN $\rightarrow$ $Al_xGa_{1-x}N$ a positive polarization charge field is created which attracts electrons (n-type), and $Al_xGa_{1-x}N$ $\rightarrow$ GaN attracts holes (*p-type*) [24]. This is due to the relative spontaneous polarization of AlN and InN to GaN.

2.3 Structure and Measurements

The $GaN/In_xGa_{1-x}N/In_yGa_{1-y}N$ graded structures have been grown by molecular beam epitaxy (MBE) at 575 °C with a 400nm unintentionally doped *GaN* buffer grown at 800 °C. Figure 1 shows the sample structure. The 88 nm graded zig-zag QW structures with different x_{max} In compositions were growth on top of the 400 nm thick *GaN* buffer layer. The designed maximum In compositions, x_{max}, were 0.15 and 0.20. However, initial x-ray diffraction (XRD) measurements have indicated that the grading results in a slightly different calibration for the growth in terms of the thicknesses and the compositions as shown in table. I The bandgap of the alloys were calculated using the following equation (Vegards law), including a bowing factor of $b = 1.6$:

$$\mathbf{E_g(In_xGa_{1-x}N) = xE_g(InN) + (1 - x)E_g(GaN) - bx(1 - x)}$$

Equation 2. 1

Table 2. 1 Maximum indium composition based on XRD measurement and bandgap based on Vegards law

Sample No	x_{max}	$E_g(eV)$
A	19.5%	2.7
B	22.5%	2.62
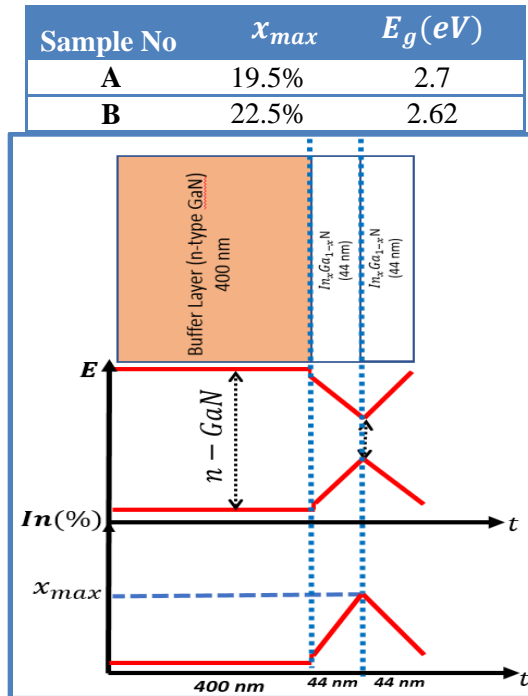
Figure 2.1. Top to bottom: Structure of samples with the given thickness of each layer; schematic energy band diagram, and indium composition vs layer thickness

Figure 2 (a) shows the symmetric XRD 2θ-ω curves. Using a simple fitting algorithm and assuming fully strained material, the thicknesses were determined to be both 88nm, while the x_{max} values were determined to be 0.195 and 0.225 for samples A and B, respectively. Detailed analysis and fitting of these XRD data will be reported elsewhere. Low temperature photoluminescence (PL) was also obtained for all samples in a closed cycle helium cryostat at ~16 K. Continuous wave excitation was provided by a HeCd laser emitting at 325 nm. All spectra are taken at a relatively low spectral resolution of ~50nm to enhance the signal intensity and reduce detection time. Since the spectrometer is linear in wavelength, this converts to a spectral resolution of ~0.1eV at 600nm and ~0.5eV at 350nm As a result, any narrow features such as the emission from the GaN substrate appear artificially broadened. However, using higher resolution settings, all spectra were determined to be exhibiting their fundamental peak shapes. I.e., all observed features are very broad with linewidths greater than 50nm.

Figure 2(b) shows an example PL spectrum taken of each of these two samples at low temperature. The GaN peak from the buffer and template layers appear in both samples at ~3.5 eV. Additionally, the bandgap of bulk $In_xGa_{1-x}N$ for $x = x_{max}$ for each sample (see Table I) is indicated by vertical lines for comparison. Also, the data range over which the analysis was performed is indicated by the vertical red lines. Above 3.5eV is not considered in analyzing the film characteristics, and below ~ 1.75 eV all light is considered as second order diffraction in the spectrometer.
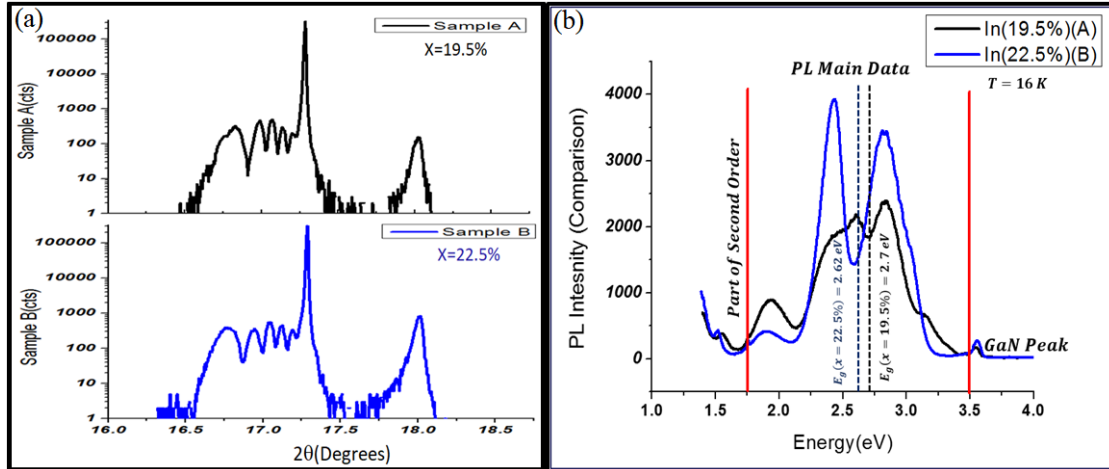
Figure 2.2. (a):The XRD measurement, for both samples(x=19.5% & 22.5%). (b): PL spectra for both samples. The bandgaps of bulk maximum indium containing InGaN for each sample is shown as a vertical dashed line.

The peak positions along with the bulk bandgap energies for x_{max} are summarized in Fig. 3. Comparison of the two samples confirms that the peak energies generally shift to lower values with increasing the maximum In content of the wells. This reinforces the idea that all features of this luminescence are due to the zig-zag QW structure and not to the substrate. Additionally, we find that for both samples there exists peaks both above and below the energy of the bulk bandgaps. These features are currently under consideration as to their origin.
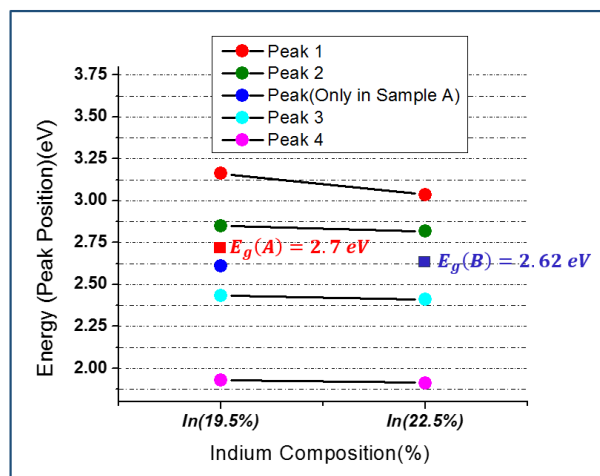
Figure 2.3. Comparison of Energy (central wavelength) (eV) for both samples for each individual peak in high laser power, Samples bandgaps are shown with square.

40

2.4 Photoluminescence Power Dependence

In order to gain some understanding as to the nature of the PL peaks and the recombination mechanisms responsible for the radiative transitions in each, the dependence of excitation intensity was studied. The power of the excitation laser was varied between 10 to 0.01 mW. The results are shown in Fig. 4. Again, here the results from samples A (x = 19.5%) and B (x = 22.5%) are compared.
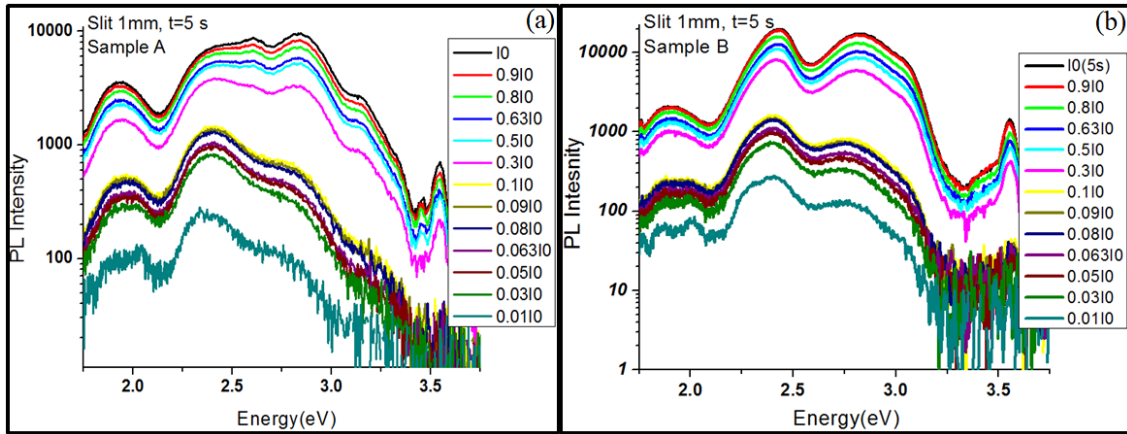
Figure 2.4. PL spectra for a) sample A & b) sample B for various excitation power (laser power).

Peak fitting using multiple Gaussians was performed on all the power dependent PL. An example is shown in Figs.5a and b for both samples with their highest excitation power (I_0) and a low excitation power ($0.1I_0$) at a low temperature of 16 K. Here it can be seen that the PL spectra of the zig-zag QWs of sample A are well fit by four peaks in the low power regime and five peaks in the high power regime. For sample B, the PL spectrum is fit well by four peaks in both the high and low power regime.
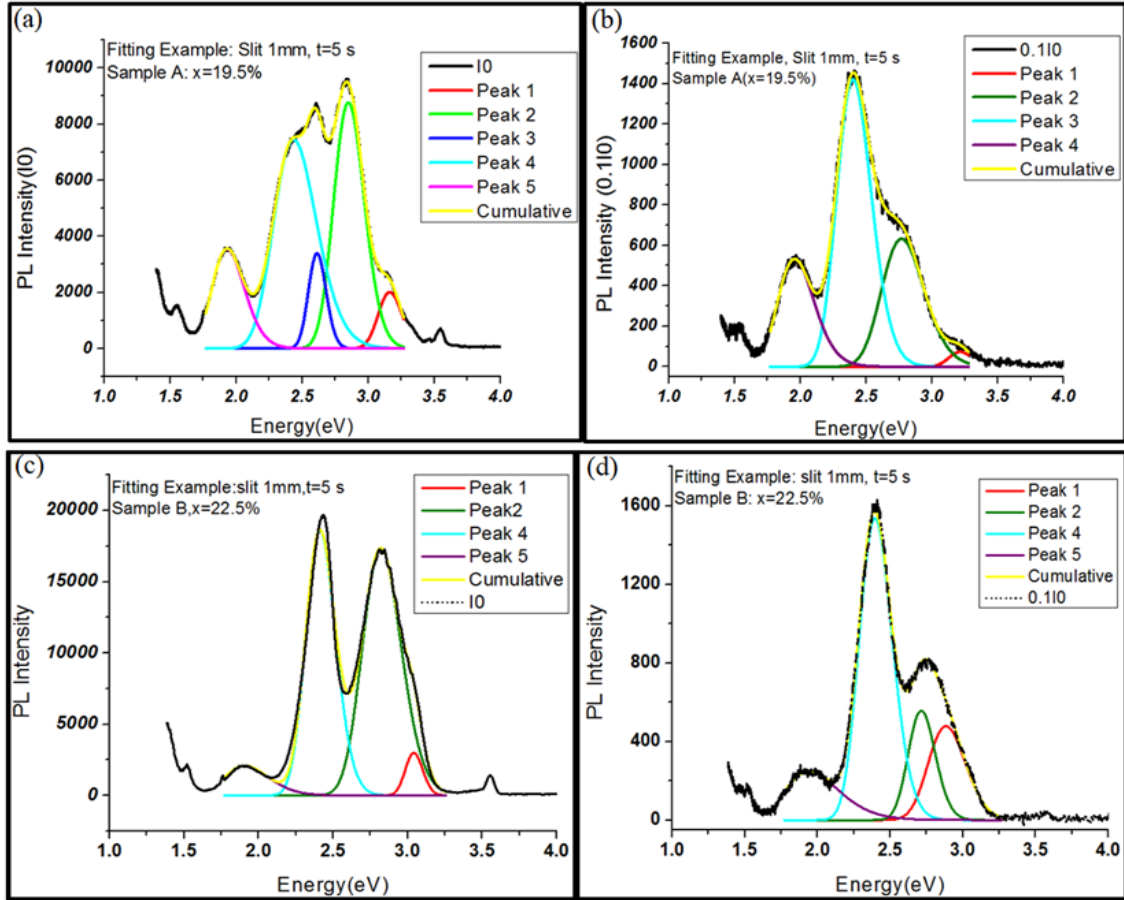
Figure 2.5. Fitting example for both samples in high and low laser excitation power regimes. a) sample A in high power, b) sample A in low power, c) sample B in high power, d) sample B in low power

Before doing full scale modeling, schematic bandgap diagrams can be used to begin to understand where multiple PL peaks may be derived from. According to the schematic energy band diagrams in Fig.6 which includes a conceptual understanding of polarization doping in a graded structure, we suggest that the strongest peak is from the bottom of the well or the center of the pn junction and the highest energy peak is from the buffer to p-type interface. While the lowest energy peak is probably from some defect band which follows either the conduction or the valence band in the structure. There could, in principle, be several defect states which result in multiple emission peaks.
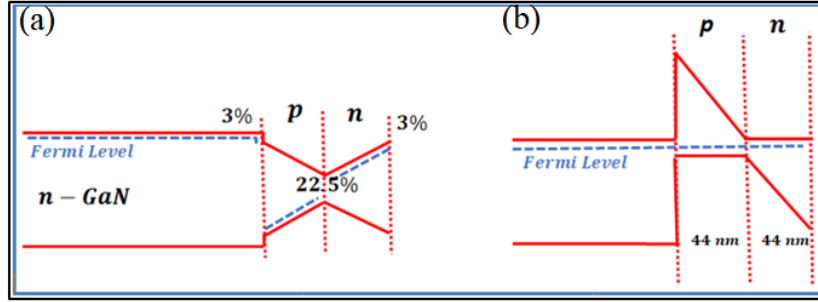
Figure 2.6. Polarization doping for increasing and decreasing indium composition in the designed graded structure. a) shows the diagram before equalization of the fermi level and b) after.

2.5 Power laws and luminescence

Generally, we can relate the PL emission intensity to the injected carrier density by a power law [25],[26]. Here, we suppose that the excitation intensity (I_{Laser}) is proportional to the injected carrier density for a constant spot size of the laser [27]. Thus, a generalized power law can be written as:

$$I_{PL} = AI_{Laser}^{\alpha}$$

Equation 2. 2

Here, the value of α can reflect different recombination processes. Generally, if α is equal to 1, it indicates an exciton like radiative transition which results from an electron and a hole bound to each other in the form of an exciton prior to recombination [27]–[29]. If α=2, it indicates free carrier recombination where a free electron in the conduction band can recombine with any free hole in the valence band. If $\alpha > 1$, it indicates that a Shockley-Read-Hall (SRH) defect mediated non-radiative recombination is competing with free carrier, radiative recombination [27] . A value of α < 1 suggests a radiative recombination mechanism including defects or impurities such as free-to-bound and donor-acceptor pair transitions which is a spatially indirect transition between an electron bound to a donor and a hole bound to an acceptor [28], [29].

To determine the power law factor, α, Eq. 2 should be linearized as well as the associated data, Fig. 7. This is necessary in order to not weight the larger values preferentially in the fitting. The given equation for the power law can then be written as:

$$I_{PL} = AI^{\alpha}_{Laser} \Rightarrow Log\,(I_{PL}) = Log\,(A) + \alpha\,Log\,(I_{Laser})$$ Equation 2. 3

Such that the slope can be taken from a linear fit to be the power law factor.
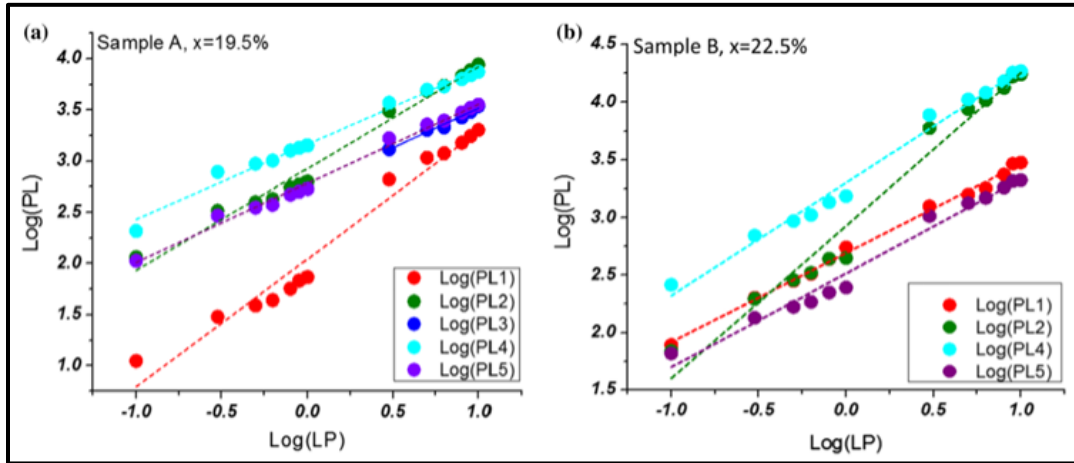
Figure 2. 7. Linearization of PL intensity versus laser power for both samples a): A (19.5%), b): B (22.5%)

Table 2. 2. Power law exponent is given for each peak in both samples

Sample $-\alpha$	α_1	α_2	α_3	α_4	α_5
A(x = 19.5%)	1.25±0.065	0.99±0.04	0.77±0.053	0.73±0.024	0.77±0.02
B(x = 22.5%)	0.77±0.015	1.32±0.07	N/A	0.98±0.03	0.81±0.03

Exciton-like transitions likely dominate the optical emission in peaks 1 and 2 in sample A. However, α_1 is large enough to suspect it has a significant free carrier character with some competition with non-radiative channels. At the same time, free-to-bound or bound-to-bound transitions likely contribute to all other peaks. For sample B, the second and forth peaks appear to be exciton-like transitions, again with the higher energy peak (this is peak 2 for this sample)

showing some free carrier character. On the other hand, the first and last peaks appear to be the result of free-to-bound or bound-to-bound transitions.

Figure 8 summarizes the PL peak positions as functions of the laser power (LP) for each of the different luminescent bands. In polar materials like the III-nitrides, PL from QWs exhibit the quantum confined stark effect [30] in which the PL energy is shifted to lower values due to the built-in electric fields. This is more directly observed when increasing the excitation power results in a shift of the peaks to higher energy (a blueshift,) which is the result of screening the electric field by the high concentrations of confined charges. For sample A, there is an obvious blueshift in peaks 2 and 4, while a general redshift appears in peaks 1 and 5. For sample B, we see that peaks 1, 2, and 4 exhibit blueshifts with increasing power, while peak 5 shows an overall redshift. The redshift is not as well understood, and could be the result of essentially "bleaching" the non-radiative recombination channels with higher excitation power causing the radiative lifetime to lengthen [31], [32]. This longer lifetime may result in carriers finding lower energy radiative states to recombine from. Therefore, we would expect a redshift from those peaks which have a power law of $\alpha > 1$, because this indicates that the radiative state is in competition with a non-radiative transition. Indeed, we find that for peak 1 in Sample A, with $\alpha_1 = 1.25$, there is a significant redshift. However, there is also a small redshift for peak 5. At the same time, we find peak 2 in Sample B has a power law of $\alpha_2 = 1.32$, but does not exhibit a redshift, while again peak 5 exhibits a small redshift. These unexplained redshifts may be influenced by surface states in the samples,[152] but this is beyond the scope of this paper.
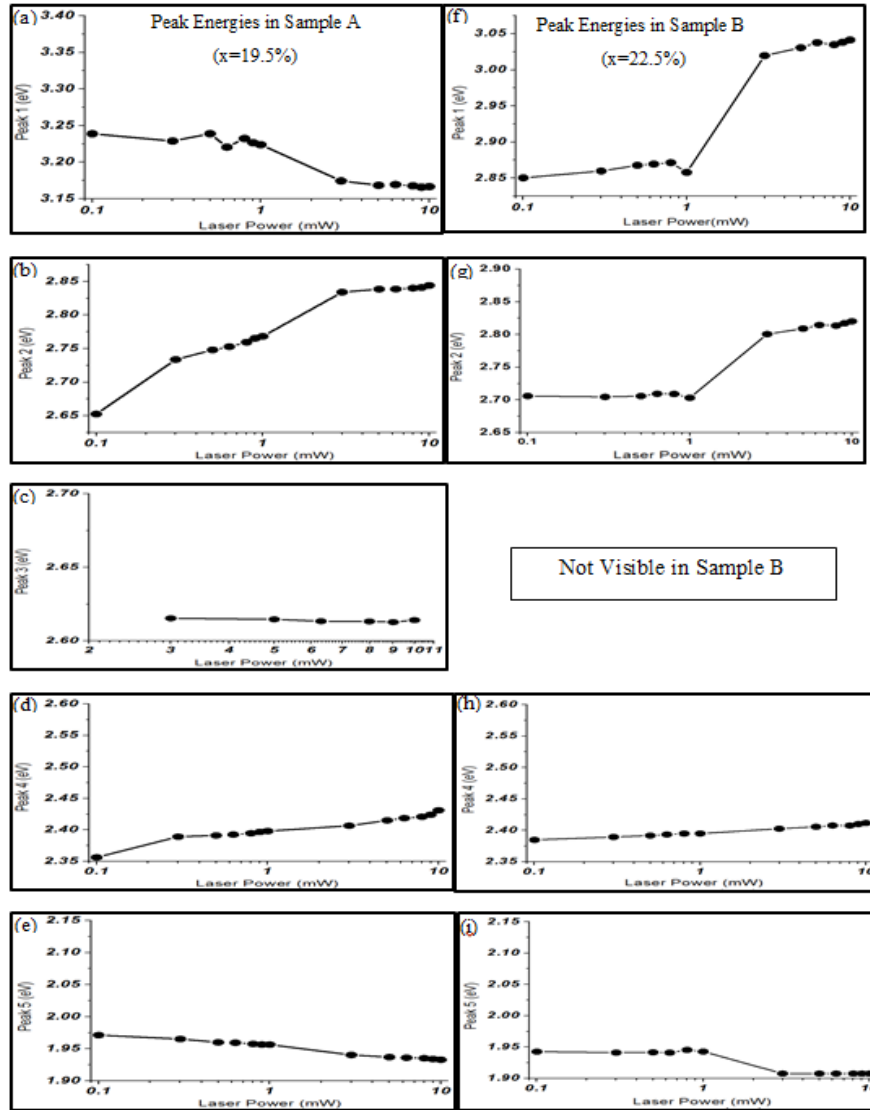
Figure 2. 8. Peak position Vs Power (peak position Shifting) Left: Sample A, Right sample B. (x axes is in Log scale)

2.6 Conclusion

We have grown and characterized graded quantum well structures of InGaN with the In composition increasing then decreasing in a zigzag pattern. The resulting polarization doping causes an effective pn-junction to form within the QW creating several possible locations for charge to accumulate and recombination to occur. This, along with the potential for radiative recombination to occur through not only band-to-band and exciton-like processes, but also defect

mediated free-to-bound or bound-to-bound processes, results in several distinct, very broad emission peaks. The emission intensity of each peak was characterized according to its power law dependence on the excitation power. The exponents, α, of these power laws were further classified according to their range as follows: $\alpha = 2$, free carrier recombination; $2 > \alpha > 1$, free carrier recombination with competition from non-radiative recombination; $\alpha = 1$, free exciton recombination; and $\alpha < 1$, radiative recombination through mid-gap bound states. According to these power laws the sources of peaks 1 and 2 in sample A are exciton like transitions. However, α_1 is large enough to suspect it has a significant free carrier character with some competition with non-radiative channels. This idea is corroborated by the fact that peak 1 in Sample A exhibits a strong redshift with excitation power. This can be the direct result of bleaching the non-radiative channel, allowing for longer lifetime carriers to find lower energy radiative states. Similarly, we find peaks 2 and 4 in Sample B (peak 3 is not evident) to be exciton-like transitions, again with the higher energy peak (this is peak 2 for this sample) showing some free carrier character. For this sample, however the redshift of the $\alpha > 1$ peak is replaced by a blueshift indicating screening of the quantum confined stark effect. All other peaks in both samples appear to be due to radiative defect states with power laws of $\alpha \approx 0.75$. The deeper understanding of these zig-zag quantum wells and the radiative processes which they exhibit will help in the development of future optoelectronic devices which can exploit their unique emission properties.

2.7 References

[1]   S. Nakamura, M. Senoh, N. Iwasa, S. Nagahama, T. Yamada, and T. Mukai, "Superbright Green InGaN Single-Quantum-Well-Structure Light-Emitting Diodes," *Jpn. J. Appl. Phys.*, vol. 34, no. Part 2, No. 10B, pp. L1332–L1335, Oct. 1995, doi:10.1143/JJAP.34.L1332

[2]   S. Nakamura *et al.*, "InGaN-Based Multi-Quantum-Well-Structure Laser Diodes," *Jpn. J. Appl. Phys.*, vol. 35, no. Part 2, No. 1B, pp. L74–L76, Jan. 1996, doi:10.1143/JJAP.35.L74

[3] G. Pozina, J. P. Bergman, B. Monemar, T. Takeuchi, H. Amano, and I. Akasaki, "Origin of multiple peak photoluminescence in InGaN/GaN multiple quantum wells," *J. Appl. Phys.*, vol. 88, no. 5, pp. 2677–2681, Sep. 2000, doi:10.1063/1.1287124

[4] A. David and M. J. Grundmann, "Influence of polarization fields on carrier lifetime and recombination rates in InGaN-based light-emitting diodes," *Appl. Phys. Lett.*, vol. 97, no. 3, p. 033501, Jul. 2010, doi:10.1063/1.3462916

[5] S. R. Routray and T. R. Lenka, "InGaN-based solar cells: a wide solar spectrum harvesting technology for twenty-first century," *CSI Trans. ICT*, vol. 6, no. 1, pp. 83–96, Mar. 2018. doi:10.1007/s40012-017-0181-9

[6] E. Vadiee *et al.*, "InGaN solar cells with regrown GaN homojunction tunnel contacts," *Appl. Phys. Express*, vol. 11, no. 8, p. 082304, Aug. 2018, doi:10.7567/APEX.11.082304

[7] X. M. Cai *et al.*, "Study of InGaN/GaN Multiple Quantum Well Solar Cells With Different Barrier Thicknesses," *Phys. Status Solidi A*, vol. 215, no. 10, p. 1700581, May 2018, doi:10.1002/pssa.201700581

[8] J. Wu, "When group-III nitrides go infrared: New properties and perspectives," *J. Appl. Phys.*, vol. 106, no. 1, p. 011101, Jul. 2009, doi:10.1063/1.3155798.

[9] G. F. Brown, J. W. Ager, W. Walukiewicz, and J. Wu, "Finite element simulations of compositionally graded InGaN solar cells," *Sol. Energy Mater. Sol. Cells*, vol. 94, no. 3, pp. 478–483, Mar. 2010, doi:10.1016/j.solmat.2009.11.010

[10] R. Dahal, B. Pantha, J. Li, J. Y. Lin, and H. X. Jiang, "InGaN/GaN multiple quantum well solar cells with long operating wavelengths," *Appl. Phys. Lett.*, vol. 94, no. 6, p. 063505, Feb. 2009, doi:10.1063/1.3081123

[11] R. Singh, D. Doppalapudi, T. D. Moustakas, and L. T. Romano, "Phase separation in InGaN thick films and formation of InGaN/GaN double heterostructures in the entire alloy composition," *Appl. Phys. Lett.*, vol. 70, no. 9, pp. 1089–1091, Mar. 1997, doi:10.1063/1.118493

[12] A. Tabata *et al.*, "Phase separation suppression in InGaN epitaxial layers due to biaxial strain," *Appl. Phys. Lett.*, vol. 80, no. 5, pp. 769–771, Feb. 2002, doi:10.1063/1.1436270

[13] Li-Hong Zhu *et al.*, "Efficiency Droop Improvement in InGaN/GaN Light-Emitting Diodes by Graded-Composition Multiple Quantum Wells," *IEEE Photonics J.*, vol. 5, no. 2, pp. 8200208–8200208, Apr. 2013, doi:10.1109/JPHOT.2013.2245881

[14] G. Verzellesi *et al.*, "Efficiency droop in InGaN/GaN blue light-emitting diodes: Physical mechanisms and remedies," *J. Appl. Phys.*, vol. 114, no. 7, p. 071101, Aug. 2013, doi:10.1063/1.4816434

[15] C. H. Wang *et al.*, "Hole transport improvement in InGaN/GaN light-emitting diodes by graded-composition multiple quantum barriers," *Appl. Phys. Lett.*, vol. 99, no. 17, p. 171106, Oct. 2011, doi:10.1063/1.3655903

[16] H. Zhao, G. Liu, J. Zhang, J. D. Poplawsky, V. Dierolf, and N. Tansu, "Approaches for high internal quantum efficiency green InGaN light-emitting diodes with large overlap quantum wells," *Opt. Express*, vol. 19, no. S4, p. A991, Jul. 2011, doi:10.1364/OE.19.00A991

[17] R. A. Arif, Y.-K. Ee, and N. Tansu, "Polarization engineering via staggered InGaN quantum wells for radiative efficiency enhancement of light emitting diodes," *Appl. Phys. Lett.*, vol. 91, no. 9, p. 091110, Aug. 2007, doi:10.1063/1.2775334

[18] H. P. Zhao *et al.*, "Design and characteristics of staggered InGaN quantum-well light-emitting diodes in the green spectral regime," *IET Optoelectron.*, vol. 3, no. 6, pp. 283–295, Dec. 2009, doi:10.1049/iet-opt.2009.0050

[19] H. Zhao *et al.*, "Growths of staggered InGaN quantum wells light-emitting diodes emitting at 520–525 nm employing graded growth-temperature profile," *Appl. Phys. Lett.*, vol. 95, no. 6, p. 061104, Aug. 2009, doi:10.1063/1.3204446

[20] A. David and M. J. Grundmann, "Droop in InGaN light-emitting diodes: A differential carrier lifetime analysis," *Appl. Phys. Lett.*, vol. 96, no. 10, p. 103504, Mar. 2010. doi:10.1063/1.3330870

[21] Y. C. Shen, G. O. Mueller, S. Watanabe, N. F. Gardner, A. Munkholm, and M. R. Krames, "Auger recombination in InGaN measured by photoluminescence," *Appl. Phys. Lett.*, vol. 91, no. 14, p. 141101, Oct. 2007, doi:10.1063/1.2785135

[22] Z.-H. Zhang *et al.*, "InGaN/GaN multiple-quantum-well light-emitting diodes with a grading InN composition suppressing the Auger recombination," *Appl. Phys. Lett.*, vol. 105, no. 3, p. 033506, Jul. 2014, doi:10.1063/1.4891334

[23] Y.-J. Lee, Y.-C. Yao, and Z.-P. Yang, "Numerical Analysis on Polarization-Induced Doping III-Nitride n-i-p Solar Cells," *IEEE Photonics J.*, vol. 7, no. 1, pp. 1–9, Feb. 2015, doi:10.1109/JPHOT.2015.2392374

[24] S. Li *et al.*, "Polarization induced pn-junction without dopant in graded AlGaN coherently strained on GaN," *Appl. Phys. Lett.*, vol. 101, no. 12, p. 122103, Sep. 2012, doi:10.1063/1.4753993

[25] X. A. Cao, E. B. Stokes, P. M. Sandvik, S. F. LeBoeuf, J. Kretchmer, and D. Walker, "Diffusion and tunneling currents in GaN/InGaN multiple quantum well light-emitting diodes," *IEEE Electron Device Lett.*, vol. 23, no. 9, pp. 535–537, Sep. 2002, doi:10.1109/LED.2002.802601

[26] I. Mártil, E. Redondo, and A. Ojeda, "Influence of defects on the electrical and optical characteristics of blue light-emitting diodes based on III–V nitrides," *J. Appl. Phys.*, vol. 81, no. 5, pp. 2442–2444, Mar. 1997, doi:10.1063/1.364294

[27] H. Wang *et al.*, "Influence of excitation power and temperature on photoluminescence in InGaN/GaN multiple quantum wells," *Opt. Express*, vol. 20, no. 4, p. 3932, Feb. 2012, doi:10.1364/OE.20.003932

[28] D. Kaplan *et al.*, "Excitation intensity dependence of photoluminescence from monolayers of MoS $_2$ and WS $_2$ /MoS $_2$ heterostructures," *2D Mater.*, vol. 3, no. 1, p. 015005, Jan. 2016, doi:10.1088/2053-1583/3/1/015005

[29] T. Schmidt, K. Lischka, and W. Zulehner, "Excitation-power dependence of the near-band-edge photoluminescence of semiconductors," *Phys. Rev. B*, vol. 45, no. 16, pp. 8989–8994, Apr. 1992, doi:10.1103/PhysRevB.45.8989

[30] C. X. Ren, "Polarisation fields in III-nitrides: effects and control," *Mater. Sci. Technol.*, pp. 1–16, Mar. 2016, doi:10.1179/1743284715Y.0000000103

[31] A. Slimane *et al.*, "On the phenomenon of large photoluminescence red shift in GaN nanoparticles," *Nanoscale Res. Lett.*, vol. 8, no. 1, p. 342, 2013, doi10.1186/1556-276X-8-342

[32] H. Sun *et al.*, "Transfer and recombination mechanism of carriers in phase-separated InGaN quantum wells," *J. Appl. Phys.*, vol. 114, no. 9, p. 093508, Sep. 2013, doi:10.1063/1.4820395

CHAPTER 3

Experiment-simulation comparison of luminescence properties of GaN/InGaN/GaN double graded structures

Authors: Mirsaeid Sarollahi, Pijush K. Ghosh, Manal A. Aldawsari, Shiva Davari, Malak I. Refaei, Reem Alhelais, Yuriy I. Mazur, Morgan E. Ware

3.1 Abstract

Graded InGaN structures have been designed by increasing the indium composition from 3% to a maximum value then back to 3%. This results in a Zig-Zag quantum well (QW) structure with a composition grading and subsequent polarization doping, which forms a p-n junction. Separate structures are designed by varying the maximum In composition but maintaining a constant QW thickness. This is both in order to test the limits of the molecular beam epitaxy growth control in terms of the deposition source ramping rates and to determine the limits of the maximum In composition within a narrow QW. The results indicate that by increasing the maximum indium composition, the overall emission, while very broad, shifts to lower energies. The broadband emission covers wavelengths between 360 and 700 nm. Simulations identify the lowest energy, band-to-band transition for fully strained structures with a noticeable shift resulting from partial relaxation in samples with higher indium content. This type of novel polarization doped structure has useful applications in optoelectronic devices; therefore the presented understanding of its optical transitions will be beneficial to their design and implementation.

3.2 Introduction

The optical properties of InGaN ternary alloys make them interesting materials for photovoltaic devices [1]–[3]. Properties such as direct and tunable bandgaps which cover the

whole range of the solar spectrum as well as high thermal conductivity, high optical absorption, and high radiation resistance are center to this interest [4], [5]. As a result, InGaN continues to receive attention in the research community both fundamentally and with a strong push towards photovoltaics [6]–[9]. Phase separation in InGaN has been studied and shown to be suppressible [10], [11]. As a result, growth of InGaN alloys have been demonstrated across the entire composition range without phase separation within an InGaN/GaN double heterostructure [12], [13]. Hence, more complicated structures may be designed. In Ref.14, they compared the effects of adding two or three staggered InGaN layers within a QW. This significantly reduced the radiative lifetime, thus enhancing the radiative efficiency. They claim employing a staggered InGaN QW design enhances the electron-hole wave function overlap in order to increase the radiative recombination rate (Rsp) and radiative efficiency of the QW for LEDs application [14].

Additionally, others have reported LEDs with triangle shaped QWs having reduced operation voltage and higher light output power than those with rectangular MQWs. This is due to the density and uniform distribution of QDs which form in the triangle QWs and act as radiative recombination centers. TEM demonstrates that QD sizes in triangle QW are much smaller (20-50 nm) than those in rectangular QWs (100 nm) [15]. In addition, other work using trapezoidal QW structures show that electron-hole wave function overlap is enhanced, which allows for a lower operating voltage at high current densities and an improved efficiency droop with a low crossover current density of 5 A/cm2, which was a significant improvement over conventional LEDs that use rectangular wells. The external quantum efficiency was increased by 20% at a current density of 70 A/cm2 [16]. A similar report is given for comparison of trapezoidal-shaped well and rectangular-shaped well. The device featuring a trapezoidal well exhibited improved EQE and alleviated efficiency droop relative to those of the device featuring

a rectangular well. The decreased Auger loss has been proposed as the main reason for the greater maximum efficiency that occurred at high current density (>50 A/cm2) [17]. Additionally, there is a simulation report about conductivity in p-type GaN/InGaN-graded super-lattices. Simulation results indicate that significantly improved electrical conductivity can be achieved by using composition graded p-type layers. Graded super-lattice design leads to an improvement of more than eleven orders of magnitude in the vertical electrical conductivity, σv, compared to typical super-lattices [18]. Multiple graded quantum wells (GQWs) used in LEDs, where each QW was formed by a single grade from GaN to InxGa1-xN, or the reverse, were grown in a device structure in order to improve the efficiency droop as well as study the polarization field effect on the efficiency droop in light emitting diodes (LEDs). The initial results claim the GQW structure increases quantum efficiency in comparison with typical LED structures. Also, efficiency droop due to electron leakage for high current injection levels was reduced in the GQW LED due to the reduction in polarization field in the active layer. Additionally, it was shown that multiple InGaN GQWs show enhanced overlap of the electron and hole wave functions in the active layer, while also creating a barrier to prevent carrier overflow for high injection currents [19]. Graded-composition multiple quantum barriers (GQB) were designed to enhance the hole transfer to the active layer and reduce efficiency droop. Furthermore, they reported improving electron-hole wave-function overlap and enhancing light output power and internal quantum efficiency (IQE) in LEDs [20], [21]. Several groups have similarly reported enhanced electron-hole wave-function overlap using graded structures [22]–[24]. In typical commercial (InGaN/GaN) QW LEDs the abrupt InGaN well is limited to 3 nm due to crystal quality consideration. In graded structures of InGaN the thickness was increased to 5 nm which allows for higher light output power. Using GQWs also reduces the polarization-

53

induced interface charge density. In a typical MQW LEDs the polarization-induced interface charge density was about $0.54*1017$ e/m^2, whereas for similar graded structures it was $0.3*1017$ e/m^2. Also, the graded structure creates a bulk charge density in the well which will screen the electric field. This reduces the effects of the quantum confined Stark effect, which normally acts to pull apart electrons and holes reducing light emission. It was again confirmed that the electron-hole wave-function overlap increases along with the optical recombination in graded structures in comparison with typical quantum wells [25]. The reduced charge separation improves the IQE. Using a graded QW also allows for the design of a wider well in order to reduce carrier densities and similarly non-radiative recombination through Auger recombination. Such a mechanism becomes important in reducing LED efficiency droop [26], [27].

In the past, graded structures (generally single grades) have been investigated in general for their strain relieving properties[28], [29]. Graded films of III-nitride materials additionally exhibit polarization doping which has been demonstrated to achieve very high levels of doping, without the use of additional impurities in the lattice. This is explained as follows. InN and GaN have different spontaneous crystal polarizations, P. When a compositionally graded structure of InGaN is grown, polarization doping is introduced proportional to the increasing (decreasing) composition resulting in a fixed charge field given by, $-\nabla.P=\rho$. When the compositional grading is from GaN to InGaN for metal polar growth, the background charges are negative ($-\nabla.P=\rho<0$) which attracts holes to create p-type doping. In the reverse condition, when the grading is from InGaN to GaN for metal polar growth, the background charges are positive ($-\nabla.P=\rho>0$) which attracts free electrons to create n-type doping. [30] .It has been shown that AlGaN polarization charge fields are reversed in comparison with InGaN. In other words, when the alloy is graded from GaN to Al$_x$Ga1-xN for metal polar growth, a positive polarization charge field is created

which attracts electrons (n-type), and when the alloy is graded from $Al_xGa_{1-x}N$ to GaN holes are attracted (p-type) [31]. This is due to the relative spontaneous polarizations of AlN, InN, and GaN.

In this study low temperature photoluminescence (PL) spectroscopy of three zig-zag QW samples with *xmax* =19.5%, 22.5%, and 26% for samples A, B, and C, respectively, has been measured using a HeCd laser at 325 nm and simulated to examine in more details the luminescent mechanisms. Our structures are GaN/InGaN/GaN double graded structures in which the indium composition increases from 3% to x_{max}, then decreases again to 3%. Our study here has been designed to begin to understand what the active optical transitions are due to. Simulations have been performed in order to understand the source of several observed peaks in each sample. The energy found for the maximum transition probability between the conduction band (CB) and the valence band (VB) has been compared with experimental data in order to understand which observed peaks are due to band-to-band transitions. Finally, the positions of the electron and hole wave-functions are determined in order to understand where, within the structure, the main luminescence is originating from.

3.3 Structure and Measurement

Molecular Beam Epitaxy (MBE) was used to grow the GaN/$In_xGa_{1-x}N$/$In_yGa_{1-y}N$ graded quantum wells as detailed in [32], [33]. The 88 nm graded structures with different maximum indium compositions (x_{max}) were grown at 575°C on top of an unintentionally doped 400 nm thick GaN buffer layer grown at 800°C. See Figure 1. The maximum In compositions, *xmax*, were determined by x-ray diffraction (XRD) measurements and simulations and are given in Table 1 along with the associated minimum bandgap, E_{g_min}, given by:

$$\mathbf{E_g(In_xGa_{1-x}N) = xE_g(InN) + (1-x)E_g(GaN) - bx(1-x)} \qquad \text{Equation 3. 1}$$

Large discrepancies are observed in the published values of b varying in the range of 1.4eV–2.8eV. Such a broad range of values of b is generally thought to be linked to the strain state rate of the studied $In_xGa_{1-x}N$ layers as well as localization affects due alloy fluctionations [32]–[38]. Also previous studies have indicated that the bowing parameter is composition dependent [40], [41]. Additionally, the bandgap recombination which is modeled by nextnano is located at the $GaN/In_{0.03}Ga_{0.97}N$ interface for which the effects of bowing parameter are negligible due to the low indium content.

Table I: maximum indium composition based on XRD measurement and bandgap based on Vegards law

Sample No	x_{max}	$E_{g\_min}(eV)$
A	19.5%	2.53
B	22.5%	2.4
C	26%	2.26
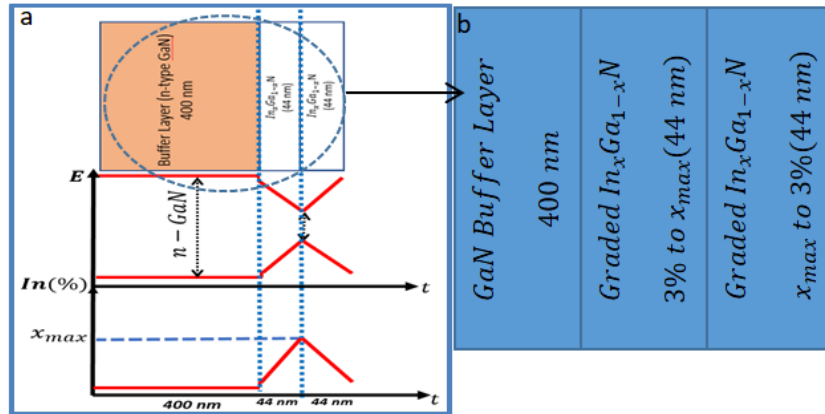
Figure 3. 1. a) Top to bottom: Structure of samples with the given thickness of each layer; schematic energy band diagram (Polarization doping disregarded), and indium composition vs layer thickness, b) Structure of samples (Zoom out)

Polarization doping, resulting from the graded $In_xGa_{1-x}N$, should leave the bottom graded layer p-type and the top graded n-type doping. This results in a narrow p-n junction structure.
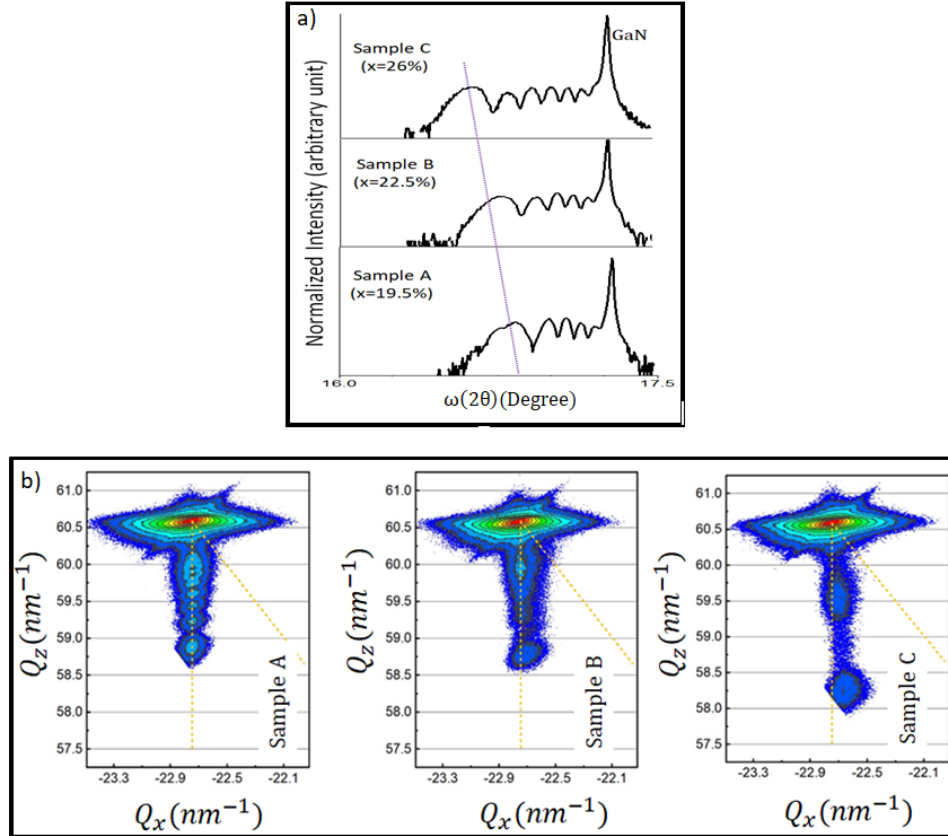
Figure 3. 2. a) Top to bottom: Structure of samples with the given thickness of each layer; schematic energy band diagram (Polarization doping disregarded), and indium composition vs layer thickness. b) Structure of samples (Zoom out)

Figure 2a shows symmetric XRD 2θ-ω curves. Using a simple fitting algorithm and assuming fully strained material; the thicknesses were determined to be ~88nm, while the x_{max} values were determined to be 0.195, 0.225, and 0.260 for samples A, B, and C, respectively. Detailed analysis and fitting of these data will be reported elsewhere. Figure 2b shows XRD reciprocal space maps for all samples. Samples A & B are fully strained, while sample C shows signs of slight relaxation in that the vertical tail, which is a signature of the grading, is shifted slightly from directly below the GaN spot. These data indicate, to within our range of interest that the grading is uniform and there are no noticeable alloy fluctuations.

Additionally, low temperature photoluminescence (PL) was obtained for all samples in a closed cycle cryostat at ~15 K. Continuous wave excitation was provided by a HeCd laser emitting at 325 nm.

The low temperature photoluminescence measurements for all samples, A through C, are shown in Fig.3a. A significant GaN substrate peak appears at 3.51 eV in each sample with the peak magnitude decreasing as x_{max} increases. This is expected as the absorption of the laser in the QW region will increase as the In composition increases, therefore reducing the amount of excitation light reaching the substrate. Additionally, we see a phonon replica of the main GaN peak at 70 meV lower in energy in all samples. The peaks seen between ~3.2 and 3.35 eV, shown in close-up in Fig.3b, are believed to be the only band-to-band luminescence present in the spectra and appear significantly above the minimum bandgaps of each structure, shown by the vertical lines in Fig.3a, as will be discussed below. We believe that all of the other spectral features to lower energies are generally the result of defect related recombination within the zig-zag QW due to the fact that they generally shift to lower energies as x_{max} increases. All of these features can be closely identified with commonly known defect state luminescence observed in GaN, which will be discussed below.
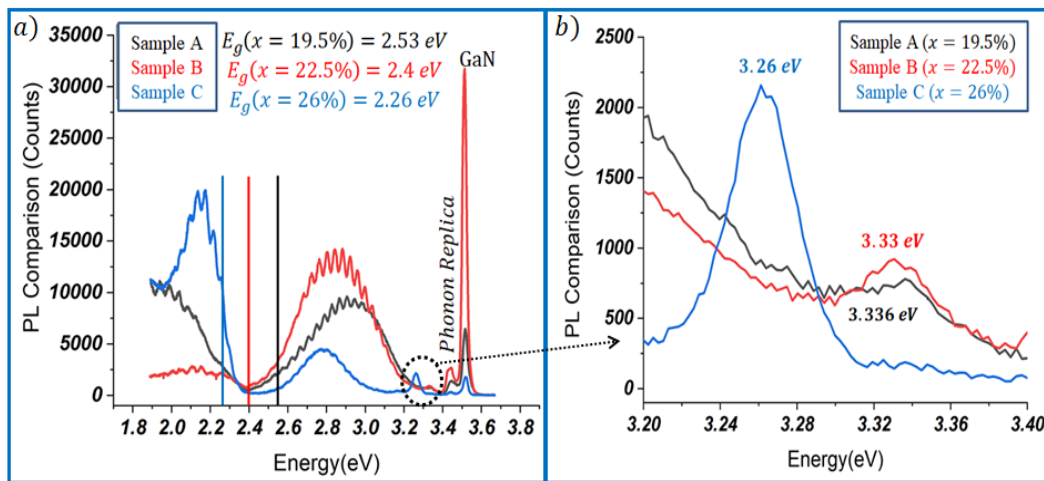
Figure 3. 3. a) PL for all samples of graded In$_x$Ga$_{1-x}$N with x=x$_{max}$ for to each sample, the bandgap energy of each x_{max} is shown by a vertical line. Black (for sample A: x=19.5%), red (for sample B: x=22.5%) and blue (for sample C: x=26%), b) expanded view around high energy peaks believed to be the band to band transitions.

3.4 Simulation Details and comparison with experiment data

In order to begin to understand the spectral dependence of the photoluminescence, the band structure of the device was simulated through self-consistent Schrödinger-Poisson calculations using the software package Nextnano3, with the goal of calculating the optical transition probabilities. These band structure simulations are shown in Fig.4a .In GaN molecular beam epitaxy, unintentional doping (background doping) can sensitively affect both the optical and electronic properties as discussed above, and can vary significantly with growth temperatures and composition, and can often be as high as $\sim 10^{17} cm^{-3}$[42]. Therefore, for the purpose of the simulation, the background doping was varied between $8 * 10^{16}$ to $2 * 10^{17}$ cm^{-3} in order to find the best match between simulation and experimental luminescence peaks with a focus on strictly band to band recombination. This match was determined with a background n-type doping concentration of $1.3 * 10^{17}$ cm^{-3}, which was subsequently used in all final simulation throughout the entire thickness of the structure. Additionally, the results of polarization doping from the compositional grading is displayed in Fig.4b. This produces holes in the first grade and electrons in the second grade, both at a concentration of $\sim 4 * 10^{18}$ cm^{-3} and resulting in an effective pn-junction in the surface region. It can be seen in Fig.4a that increasing the in composition generally decreases the bandgap, however with the large built-in field resulting from the pn-junction, there is very little chance for seeing recombination in the region of the minimum bandgap. This is the first indication that the luminescence seen in Fig. 3 would likely not have a band corresponding to the alloy with the highest composition of Indium. According to the charge

density and the energy band diagrams in Fig.4, the free charges (holes) are localized at the interface between the substrate (GaN) and the graded structure.
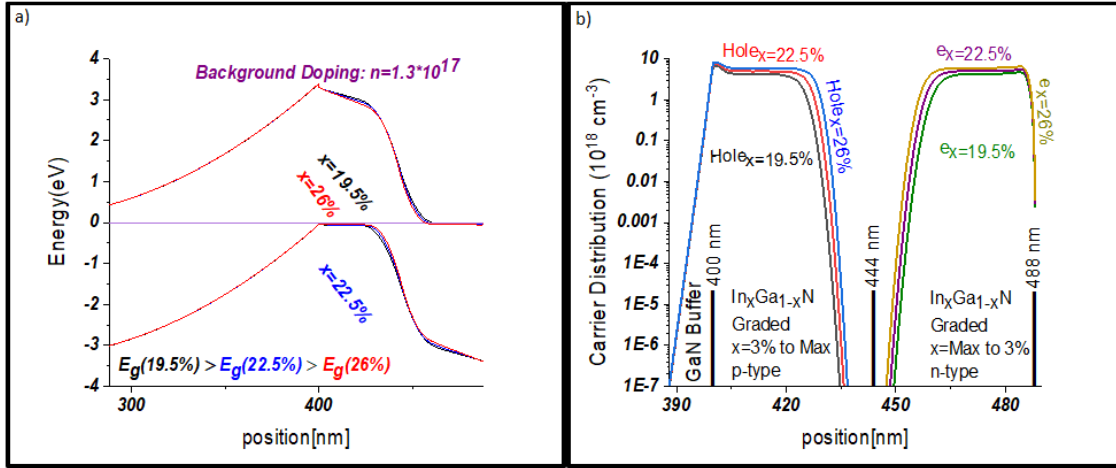
Figure 3. 4. a) Energy band diagram Comparison for all samples b) Charge distribution in p & n parts due to polarization doping in all samples.

The transition probabilities were calculated by Nextnano3 by determining the wavefunctions for electrons in a pseudo-continuum between position 400 nm and ~480 nm along with the wavefunctions for the holes in the same range assuming the valence band in the region between ~350 nm and ~450 nm formed a confined well for holes. The pseudo-continuum is considered as the set of nearly free electron states bound by the band maximum at the GaN/InGaN interface and the surface of the crystal. These wil be discussed in more details below. Electrons and holes outside of these ranges were considered, but showed negligable transition probabilities. For the purpose of this study, we were interested in determining the band-to-band transition at the low excitation powers used. Therefore, we only show the ground state hole wavefunction along with the local wavefunctions for the electrons. Again, higher excited state holes were considered, but the presence of luminescence from these excited states is unlikely due to the low excitation power used, experimentally. The wavefunctions, which contribute to the highest transition probabilities along with the local bandstructures for each

sample are shown in Fig. 5. As a result of these, we can determine that the band-to-band luminescence of these types of samples originates at the back interface between the intitial grading and the GaN buffer layer as a result of the suden band offset due to the nonzero In composition of the initial deposition. The wave-function of the ground state hole and the 4 electrons, which were shown to have the maximum transition probabilities of this system, are displayed within the band-diagram as functions of position in Fig.5. In addition, the transition energies and probabilities for each transition are shown. In considering fully strained material, the hole wave-functions are confined at the interface of GaN buffer layer and the initial grading of the thin film. On the other hand, the wave-functions of electrons are distributed roughly evenly along the conduction band edge in Fig5a, b, & c. The decreasing transition probabilities of the ground state holes from 18.96% in sample A to 18.4% in sample B indicates that the PL intensity of this band to band transistion should also decrease. If strain is considered to fully relax, the localized hole is found ~10nm deeper inside the graded film as shown in Fig 5.d for sample C. This in fact increases the overlap of the elecrons and the hole wavefunctions, increasing the transition probability to 22.24%. As a result of these simulations, the most intense transition energies are predicted to be 3.332, 3.320, and 3.303 eV for samples A, B, and C, respectively. In addition, the transition energy for sample C when fully relaxed is shown to be 3.075 eV.

In general, we make no comment regarding the relative intensities of these luminescent states, however it is noted that in Fig. 3, the emission from sample C is considerably more intense than the others while it is conjectured to be slightly relaxed by inclusion of dislocations. We believe that having the hole wavefunction localized away from the interface as can be seen in Fig. 5d due to the partial strain relaxation allows it to recombine free from any interface state

influences as well as being more symmetric and slightly broader is can potentially recombine with a larger electron density of states.
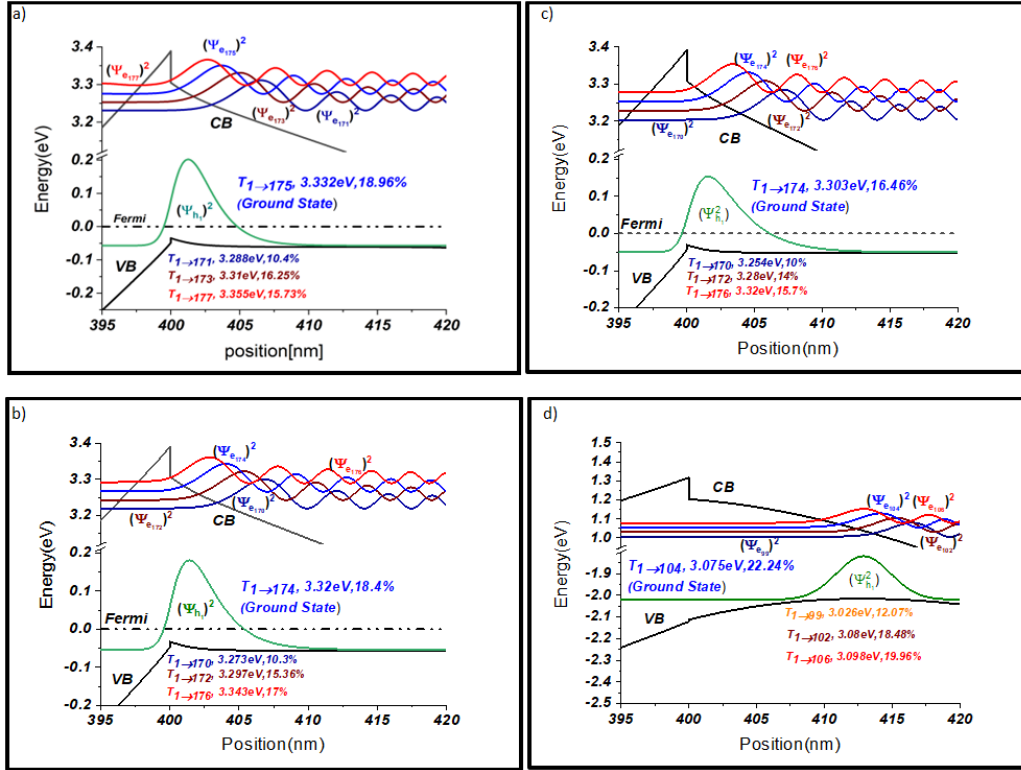
Figure 3. 5. a),b),c) (Fully strained condition for sample A, B, and C, respectively) and d) (No strain for sample C) show the position of ground state wave-function (in VB) and 4 electron wave-functions (in CB) which have the maximum transition probabilities within the bandgap. In addition, transition probabilities and transition energies are given for each transition between electron and hole states.

The results of these calculation are shown in Fig. 6 for all sample structures. Shown here are the transition probabilities for each sample around the local maximum probability. Notably, the probabilites alternate between ~0 and a varying nonzero value. This results from the alternating even and odd nature of the electron wavefunctions. Those probabilities that evaluate to ~0 can be ignored now, but are included here for completeness. It can be seen that for increasing maximum In content in the structures there is a monotonic decrease in the energy of the maximum probability. This would be generally expected, but the corresponding energies of

the bandgaps for $In_{xmax}Ga_{1-xmax}N$ are ~0.6 eV lower than these predicted recombination energies. This is a result of the fact that these transitions are restricted to the area just above the GaN buffer layer, just inside the beginning of the grade in composition.

The result of analyzing the electron-hole transitions through the dipole transition probabilities results in alternating symmetric and anti-symmetric electron-hole overlap integrals. This is evident in the nearly zero transition probabilities alternating with the non-zero transition probabilities. In the resulting simulated PL the near zero transition probabilities would simply not be observed, leaving the positive transition probabilities to create the envelope of the predicted PL as is shown in Fig.6.
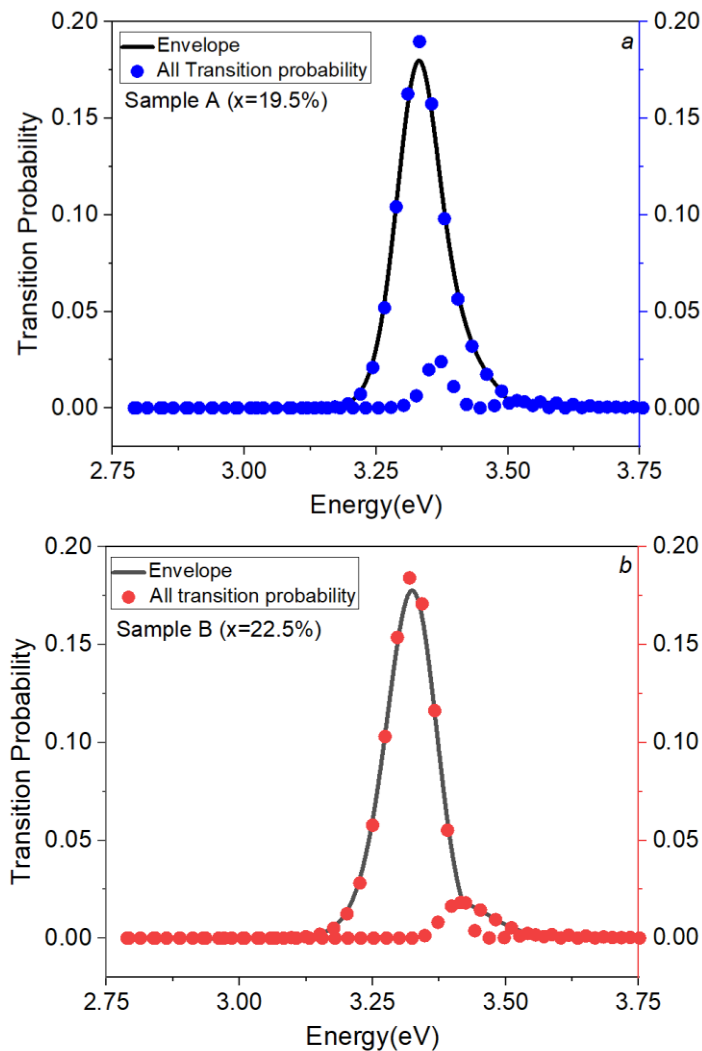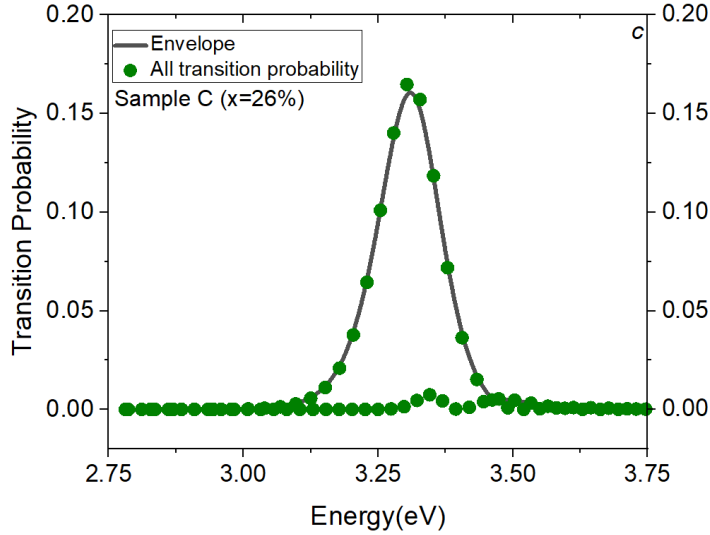
Figure 3. 6. a),b),c) Transition probability versus energy for envelop (line plot) which predicts PL. All conditions (dot plot) for all samples at background doping $1.3*10^{17}$ respectively for sample A, B and C.

Next, the effects of strain relaxation on the energy band diagram, the electron and hole wave-functions, and the transition probability are shown in Fig. 7a and b for Sample C. As shown above in Fig. 2, the XRD data show some partial relaxation for the sample with $x_{max}=26\%$. In order to understand the effect of this relaxation on the luminescence, the simulation for this sample was performed again assuming a strain free, completely relaxed growth. The results of this are shown in Fig. 8a along with the strained results again, and the PL spectra. This shows that the PL peak is located between the two extremes of strain and no strain, which is as expected. But, it is interesting to see the range of variation resulting from relaxation in the layer. This demonstrates that this band-to-band transition can vary by nearly 0.2 eV simply by relaxing the strain. The effect of strain and relaxation on the energy band diagram is shown in Fig.7b, where a dramatic change in the structure of the valence band edge can be seen, which in turn affects the hole wavefunctions. The inset of Fig. 7b, shows these hole wavefunctions which result in the maximum recombination probability for both the fully strained and the un-strained structures. So, it is evident that the strain not only shifts the recombination

energy, but it also results in a shift in the location of maximum recombination by ~15 nm. Taking to account all experiment and simulation uncertainties, we consider a shift of + or – 0.01 eV to be negligible as in samples A and B, and therefore the model represents the data very well. Additionally, in Fig.7a which shows the modeled peak for Sample C shifting by $-0.43\ eV$ away from the fully strained prediction, we can see that the peak is shifting towards the relaxed or no strain position. This generally indicates that this anomalous shift is the result of the partial strain relaxation, which correlates with the XRD RSM data in Fig. 2b.
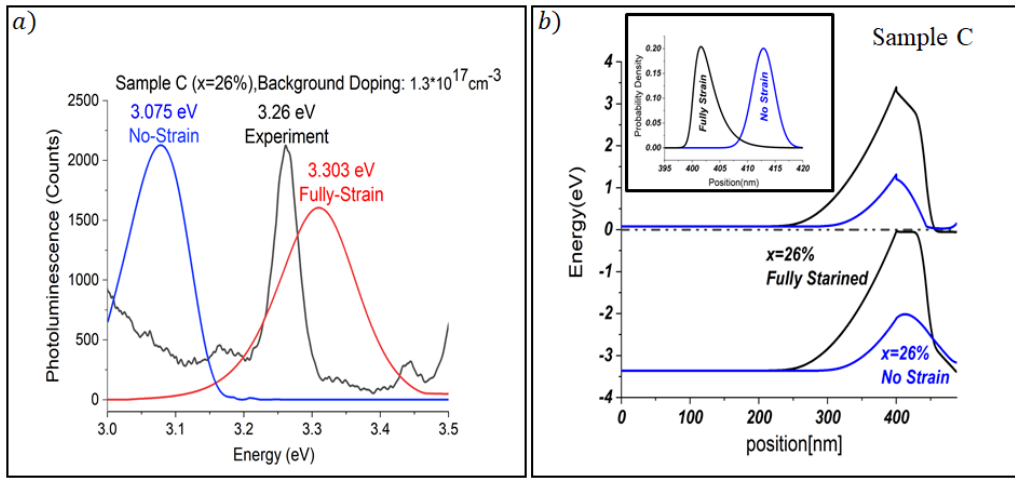
Figure 3. 7. Comparison for Experiment, Fully Strained and No Strain in sample C(x=26%), lines (blue and red) are corresponded to envelopes similar to Fig.6. b) Energy Band Diagram with & without strain. In addition, ground state wave functions are shown with & without strain in inserted plot.

For the other two samples, A and, B with lower indium compositions, the XRD results show fully strained InGaN. In these cases the experimental PL matches almost exactly with the simulated luminescence peak when for a background n-type doping density of $1.3 * 10^{17}\ cm^{-3}$. Comparisons between the experimental PL spectra and the simulated luminescence peaks for samples A and B are shown in Figs. 8a and 8b for samples A and B, respectively. Here, a very good correlation between experiment and simulation can be seen for both samples, which demonstrates that the peak at 3.336 eV for sample A, and at 3.33 eV for sample B are the band-

to-band transitions, along with the peak at 3.26 eV for sample C (Fig. 7a), for each of the samples. According to this, we assign the remaining peaks in Fig.3a to defect states within the Zigzag quantum well.

Another mechanism to consider is alloy fluctuations, which might result in localization of charges similar to defects. In Ref.[43], general alloy fluctuations are shown to affect the band edge and emission energy of InGaN thin films by less than ~100 meV at ~20% In and only ~40 meV at ~3 % In. As a result, we rule out these effects in our discussion as the variability (linewidth) resulting from the localization of the carriers at the interface between the GaN buffer and the beginning of the graded film due to the sudden band offset is more than that due to any possible alloy fluctuations.

One of the main features of GaN is the appearance in the luminescence spectra of a broad, so-called, yellow band emission centered around 2.2–2.3eV. Defect bands are widely reported in GaN by photoluminescence measurements which show a broad yellow band, YL, and a less common green band. GL [44]–[46]. The nature of the yellow band is currently understood to be a transition between the conduction band and a deep acceptor [44], [47]. Carbon [39] and oxygen [35], [36] are common residual impurities forming complexes with Ga vacancies, denoted as $V_{Ga}C_N$, and $V_{Ga}O_N$. A singly charged state of the latter complex can also be the origin of a green band emission observed in freestanding material [44]. From studying the excitation dependence of PL, the YL and GL luminescence bands were assigned to two charge states of, presumably the $V_{Ga}O_N$ pair [48]. These defects are commonly introduced during the growth process. Moreover, it is not possible to avoid contamination of other elements such as Si and O, which are always present during growth [49]. Additionally, A variety of the V_{Ga}-containing

complexes may form acceptor-like defect levels in the lower half of the band gap and therefore be responsible for some transitions observed in luminescence experiments [50].

In our samples, as mentioned above, high energy peaks (around 2.8 to 2.9 eV) are considered as defect states. Due to n-type background doping which is common in these samples, $O - V_{Ga}$, and $Si - V_{Ga}$ are likely. However, the story for sample C due to partial relaxation is different. As can be seen the peak around 2.2 eV (for sample C) isn't located like other peaks (for samples A & B). This strong peak shifted to higher energies can be considered as combination of V_{Ga}, and its complexes, such as the $V_{Ga}O_N$, pair and partial relaxation in sample C. For sample A & B at lower energies defect peaks are likely, which are complexes between the cation vacancy and oxygen because they have even lower energies than the isolated vacancy[48]. According to Ref.[51], in contrast with investigations that the YL correlated with concentrations of V_{Ga} O_N, and Si_{Ga}, they reported that the YL band is weaker in the un-doped GaN sample with relatively higher concentration of oxygen and V_{Ga}, as compared to a C-doped sample. This result may indicate that a V_{Ga}-O_N complex is not the only defect responsible for the broad emission near 2.2 eV in n-type GaN so the lower energy defects states for sample A and B (less than 2.2 eV) are likely as explained above. In particular, transitions from the deep donor to the shallow acceptor would have a low probability in un-doped GaN due to negligible overlap of the hole and electron wave functions for widely spaced deep donors and acceptors[50].
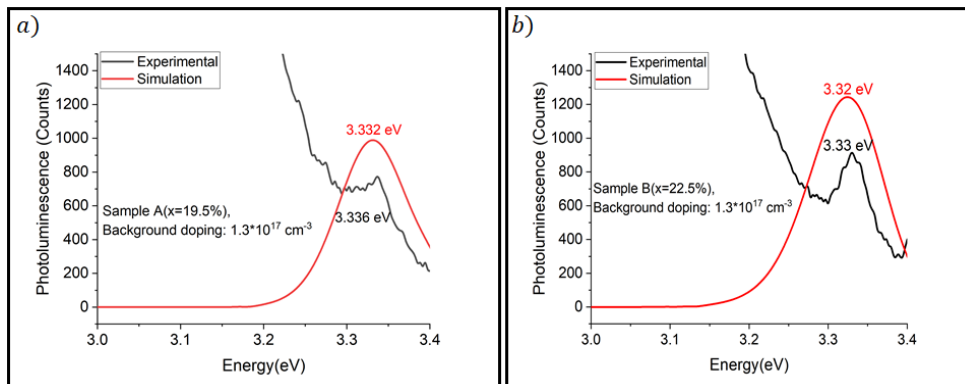
Figure 3. 8. Experiment & Simulation comparison for a) Sample A (x=19.5%) &b) Sample B (x=22.5%). Red lines are corresponded to envelope in Fig.6.

3.5 Conclusion

Simulations of the InGaN zig-zag quantum wells have shown that the ground state hole wave function confined at the interface of the GaN buffer layer and the first graded layer due to the small nonzero In composition at the base of the grade. Transition probabilities were calculated by using a pseudo-continuum set of electron states in the conduction band. The energy of highest transition probability in samples A and B is match well with the highest energy peak in the PL spectra that is not associated with the GaN substrate. The other peaks in the spectra are assumed to be defect states, normally seen in III-nitride semiconductors. The high energy peak in sample C, similarly coincides with the simulated energy of maximum transition probability, however there is some notable shift which is explained as being due to partial strain relaxation in the layer.

3.6 References

[1]   S. Nakamura, M. Senoh, N. Iwasa, S. Nagahama, T. Yamada, and T. Mukai, "Superbright Green InGaN Single-Quantum-Well-Structure Light-Emitting Diodes," Japanese Journal of Applied Physics, vol. 34, no. Part 2, No. 10B, pp. L1332–L1335, Oct. 1995, doi: 10.1143/JJAP.34.L1332.

[2]   S. Nakamura et al., "InGaN-Based Multi-Quantum-Well-Structure Laser Diodes," Japanese Journal of Applied Physics, vol. 35, no. Part 2, No. 1B, pp. L74–L76, Jan. 1996, doi: 10.1143/JJAP.35.L74.

[3]   G. Pozina, J. P. Bergman, B. Monemar, T. Takeuchi, H. Amano, and I. Akasaki, "Origin of multiple peak photoluminescence in InGaN/GaN multiple quantum wells," Journal of Applied Physics, vol. 88, no. 5, pp. 2677–2681, Sep. 2000, doi: 10.1063/1.1287124.

[4]   A. G. Bhuiyan, K. Sugita, A. Hashimoto, and A. Yamamoto, "InGaN Solar Cells: Present State of the Art and Important Challenges," IEEE Journal of Photovoltaics, vol. 2, no. 3, pp. 276–293, Jul. 2012, doi: 10.1109/JPHOTOV.2012.2193384.

[5]   A. David and M. J. Grundmann, "Influence of polarization fields on carrier lifetime and recombination rates in InGaN-based light-emitting diodes," Applied Physics Letters, vol. 97, no. 3, p. 033501, Jul. 2010, doi: 10.1063/1.3462916.

[6]   G. F. Brown, J. W. Ager, W. Walukiewicz, and J. Wu, "Finite element simulations of compositionally graded InGaN solar cells," Solar Energy Materials and Solar Cells, vol. 94, no. 3, pp. 478–483, Mar. 2010, doi: 10.1016/j.solmat.2009.11.010.

[7]   X. M. Cai et al., "Study of InGaN/GaN Multiple Quantum Well Solar Cells With Different Barrier Thicknesses," physica status solidi (a), vol. 215, no. 10, p. 1700581, May 2018, doi: 10.1002/pssa.201700581.

[8]   S. R. Routray and T. R. Lenka, "InGaN-based solar cells: a wide solar spectrum harvesting technology for twenty-first century," CSI Transactions on ICT, vol. 6, no. 1, pp. 83–96, Mar. 2018, doi: 10.1007/s40012-017-0181-9.

[9]   E. Vadiee et al., "InGaN solar cells with regrown GaN homojunction tunnel contacts," Applied Physics Express, vol. 11, no. 8, p. 082304, Aug. 2018, doi: 10.7567/APEX.11.082304.

[10]   M. D. Mccluskey et al., "Phase Separation in InGaN/GaN Multiple Quantum Wells," MRS Proc., vol. 482, p. 985, 1997, doi: 10.1557/PROC-482-985.

[11]   S. Yu. Karpov, "Suppression of phase separation in InGaN due to elastic strain," MRS Internet j. nitride semicond. res., vol. 3, p. e16, 1998, doi: 10.1557/S1092578300000880.

[12]   R. Singh, D. Doppalapudi, T. D. Moustakas, and L. T. Romano, "Phase separation in InGaN thick films and formation of InGaN/GaN double heterostructures in the entire alloy composition," Applied Physics Letters, vol. 70, no. 9, pp. 1089–1091, Mar. 1997, doi: 10.1063/1.118493.

[13]   A. Tabata et al., "Phase separation suppression in InGaN epitaxial layers due to biaxial strain," Applied Physics Letters, vol. 80, no. 5, pp. 769–771, Feb. 2002, doi: 10.1063/1.1436270.

[14]   H. P. Zhao et al., "Design and characteristics of staggered InGaN quantum-well light-emitting diodes in the green spectral regime," IET Optoelectronics, vol. 3, no. 6, pp. 283–295, Dec. 2009, doi: 10.1049/iet-opt.2009.0050.

[15]   R. J. Choi, Y. B. Hahn, H.-W. Shim, E.-K. Suh, C. H. Hong, and H. J. Lee, "Improvement of electrical and optical properties of ingan/ganbased lightemitting diodes with triangular quantum well structure," Korean J. Chem. Eng., vol. 20, no. 6, pp. 1134–1137, Nov. 2003, doi: 10.1007/BF02706949.

[16]   S.-H. Han et al., "Improvement of efficiency droop in InGaN/GaN multiple quantum well light-emitting diodes with trapezoidal wells," J. Phys. D: Appl. Phys., vol. 43, no. 35, p. 354004, Sep. 2010, doi: 10.1088/0022-3727/43/35/354004.

[17]   R.-M. Lin, M.-J. Lai, L.-B. Chang, C.-H. Huang, and C.-H. Chen, "Effect of Trapezoidal-Shaped Well on Efficiency Droop in InGaN-Based Double-Heterostructure Light-Emitting Diodes," International Journal of Photoenergy, vol. 2012, pp. 1–5, 2012, doi: 10.1155/2012/917159.

[18]   M. Z. Kauser, A. Osinsky, A. M. Dabiran, and S. J. Pearton, "Optimization of conductivity in p-type GaN∕InGaN-graded superlattices," Journal of Applied Physics, vol. 97, no. 8, p. 083715, Apr. 2005, doi: 10.1063/1.1884247.

[19]   Li-Hong Zhu et al., "Efficiency Droop Improvement in InGaN/GaN Light-Emitting Diodes by Graded-Composition Multiple Quantum Wells," IEEE Photonics Journal, vol. 5, no. 2, pp. 8200208–8200208, Apr. 2013, doi: 10.1109/JPHOT.2013.2245881.

[20]   G. Verzellesi et al., "Efficiency droop in InGaN/GaN blue light-emitting diodes: Physical mechanisms and remedies," Journal of Applied Physics, vol. 114, no. 7, p. 071101, Aug. 2013, doi: 10.1063/1.4816434.

[21]   C. H. Wang et al., "Hole transport improvement in InGaN/GaN light-emitting diodes by graded-composition multiple quantum barriers," Appl. Phys. Lett., vol. 99, no. 17, p. 171106, Oct. 2011, doi: 10.1063/1.3655903.

[22]   H. Zhao, G. Liu, J. Zhang, J. D. Poplawsky, V. Dierolf, and N. Tansu, "Approaches for high internal quantum efficiency green InGaN light-emitting diodes with large overlap quantum wells," Opt. Express, vol. 19, no. S4, p. A991, Jul. 2011, doi: 10.1364/OE.19.00A991.

[23]   R. A. Arif, Y.-K. Ee, and N. Tansu, "Polarization engineering via staggered InGaN quantum wells for radiative efficiency enhancement of light emitting diodes," Appl. Phys. Lett., vol. 91, no. 9, p. 091110, Aug. 2007, doi: 10.1063/1.2775334.

[24]   H. Zhao et al., "Growths of staggered InGaN quantum wells light-emitting diodes emitting at 520–525 nm employing graded growth-temperature profile," Appl. Phys. Lett., vol. 95, no. 6, p. 061104, Aug. 2009, doi: 10.1063/1.3204446.

[25]   Z.-H. Zhang et al., "InGaN/GaN multiple-quantum-well light-emitting diodes with a grading InN composition suppressing the Auger recombination," Appl. Phys. Lett., vol. 105, no. 3, p. 033506, Jul. 2014, doi: 10.1063/1.4891334.

[26]   A. David and M. J. Grundmann, "Droop in InGaN light-emitting diodes: A differential carrier lifetime analysis," Appl. Phys. Lett., vol. 96, no. 10, p. 103504, Mar. 2010, doi: 10.1063/1.3330870.

[27]   Y. C. Shen, G. O. Mueller, S. Watanabe, N. F. Gardner, A. Munkholm, and M. R. Krames, "Auger recombination in InGaN measured by photoluminescence," Appl. Phys. Lett., vol. 91, no. 14, p. 141101, Oct. 2007, doi: 10.1063/1.2785135.

[28]   E. A. Fitzgerald et al., "Totally relaxed Ge x Si 1− x layers with low threading dislocation densities grown on Si substrates," Appl. Phys. Lett., vol. 59, no. 7, pp. 811–813, Aug. 1991, doi: 10.1063/1.105351.

[29]   F. K. LeGoues, B. S. Meyerson, J. F. Morar, and P. D. Kirchner, "Mechanism and conditions for anomalous strain relaxation in graded thin films and superlattices," Journal of Applied Physics, vol. 71, no. 9, pp. 4230–4243, May 1992, doi: 10.1063/1.350803.

[30]   Y.-J. Lee, Y.-C. Yao, and Z.-P. Yang, "Numerical Analysis on Polarization-Induced Doping III-Nitride n-i-p Solar Cells," IEEE Photonics J., vol. 7, no. 1, pp. 1–9, Feb. 2015, doi: 10.1109/JPHOT.2015.2392374.

[31]   S. Li et al., "Polarization induced pn-junction without dopant in graded AlGaN coherently strained on GaN," Appl. Phys. Lett., vol. 101, no. 12, p. 122103, Sep. 2012, doi: 10.1063/1.4753993.

[32]   P. K. Ghosh et al., "Investigation of the Structural and Optical Properties of Compositionally V-Graded Strained In x Ga 1− x N Layers," physica status solidi (b), vol. 257, no. 4, p. 1900591, Apr. 2020, doi: 10.1002/pssb.201900591.

[33]   M. Sarollahi, P. K. Ghosh, M. A. Aldawsari, A. Kuchuk, and M. E. Ware, "Luminescence Properties of GaN/InxGa1−xN/InyGa1−yN Double Graded Structures (Zigzag Quantum Wells)," Journal of Electronic Materials, vol. 49, no. 6, pp. 3512–3519, Jun. 2020, doi: 10.1007/s11664-020-08033-w.

[34]   T. Aschenbrenner et al., "Optical and structural characterization of AlInN layers for optoelectronic applications," Journal of Applied Physics, vol. 108, no. 6, p. 063533, Sep. 2010, doi: 10.1063/1.3467964.

[35]   M. Kurouchi, T. Araki, H. Naoi, T. Yamaguchi, A. Suzuki, and Y. Nanishi, "Growth and properties of In-rich InGaN films grown on (0001) sapphire by RF-MBE," phys. stat. sol. (b), vol. 241, no. 12, pp. 2843–2848, Oct. 2004, doi: 10.1002/pssb.200405121.

[36]   M. D. McCluskey, C. G. Van de Walle, C. P. Master, L. T. Romano, and N. M. Johnson, "Large band gap bowing of InxGa1−xN alloys," Appl. Phys. Lett., vol. 72, no. 21, pp. 2725–2726, May 1998, doi: 10.1063/1.121072.

[37]   M. Moret et al., "Optical, structural investigations and band-gap bowing parameter of GaInN alloys," Journal of Crystal Growth, vol. 311, no. 10, pp. 2795–2797, May 2009, doi: 10.1016/j.jcrysgro.2009.01.009.

[38]   J. Wu et al., "Small band gap bowing in In1−xGaxN alloys," Appl. Phys. Lett., vol. 80, no. 25, pp. 4741–4743, Jun. 2002, doi: 10.1063/1.1489481.

[39]   J. Wu, "When group-III nitrides go infrared: New properties and perspectives," Journal of Applied Physics, vol. 106, no. 1, p. 011101, Jul. 2009, doi: 10.1063/1.3155798.

[40] M. A. Caro, S. Schulz, and E. P. O'Reilly, "Theory of local electric polarization and its relation to internal strain: Impact on polarization potential and electronic properties of group-III nitrides," Phys. Rev. B, vol. 88, no. 21, p. 214103, Dec. 2013, doi: 10.1103/PhysRevB.88.214103.

[41] P. G. Moses, M. Miao, Q. Yan, and C. G. Van de Walle, "Hybrid functional investigations of band gaps and band alignments for AlN, GaN, InN, and InGaN," The Journal of Chemical Physics, vol. 134, no. 8, p. 084703, Feb. 2011, doi: 10.1063/1.3548872.

[42] T. Tingberg, T. Ive, and A. Larsson, "Investigation of Si and O Donor Impurities in Unintentionally Doped MBE-Grown GaN on SiC(0001) Substrate," Journal of Elec Materi, vol. 46, no. 8, pp. 4898–4902, Aug. 2017, doi: 10.1007/s11664-017-5484-y.

[43] R. Butté et al., "Optical absorption edge broadening in thick InGaN layers: Random alloy atomic disorder and growth mode induced fluctuations," Appl. Phys. Lett., vol. 112, no. 3, p. 032106, Jan. 2018, doi: 10.1063/1.5010879.

[44] M. A. Reshchikov, H. Morkoç, S. S. Park, and K. Y. Lee, "Two charge states of dominant acceptor in unintentionally doped GaN: Evidence from photoluminescence study," Appl. Phys. Lett., vol. 81, no. 26, pp. 4970–4972, Dec. 2002, doi: 10.1063/1.1531227.

[45] M. A. Reshchikov, H. Morkoç, S. S. Park, and K. Y. Lee, "Yellow and green luminescence in a freestanding GaN template," Appl. Phys. Lett., vol. 78, no. 20, pp. 3041–3043, May 2001, doi: 10.1063/1.1371961.

[46] C. Díaz-Guerra, J. Piqueras, A. Castaldini, A. Cavallini, and L. Polenta, "Time-resolved cathodoluminescence and photocurrent study of the yellow band in Si-doped GaN," Journal of Applied Physics, vol. 94, no. 4, pp. 2341–2346, Aug. 2003, doi: 10.1063/1.1592296.

[47] K. Saarinen et al., "Observation of Native Ga Vacancies in GaN by Positron Annihilation," Phys. Rev. Lett., vol. 79, no. 16, pp. 3030–3033, Oct. 1997, doi: 10.1103/PhysRevLett.79.3030.

[48] T. Mattila and R. M. Nieminen, "Point-defect complexes and broadband luminescence in GaN and AlN," Phys. Rev. B, vol. 55, no. 15, pp. 9571–9576, Apr. 1997, doi: 10.1103/PhysRevB.55.9571.

[49] C. G. Van de Walle and J. Neugebauer, "First-principles calculations for defects and impurities: Applications to III-nitrides," Journal of Applied Physics, vol. 95, no. 8, pp. 3851–3879, Apr. 2004, doi: 10.1063/1.1682673.

[50] M. A. Reshchikov and H. Morkoç, "Luminescence properties of defects in GaN," Journal of Applied Physics, vol. 97, no. 6, p. 061301, Mar. 2005, doi: 10.1063/1.1868059.

[51]   R. Armitage et al., "Contributions from gallium vacancies and carbon-related defects to the 'yellow luminescence' in GaN," Appl. Phys. Lett., vol. 82, no. 20, pp. 3457–3459, May 2003, doi: 10.1063/1.1578169.

CHAPTER 4

Effects of numbers of wells on optical properties of periodic InGaN graded structure

Authors: Mirsaeid. Sarollahi, Rohith Allaparthi, Reem Alhelais, Manal A. Aldawsari, Malak A. Refaei, Md Helal Uddin Maruf , Morgan E. Ware

4.1 Abstract

The optical properties of periodic graded GaN/InGaN are studied. We have designed graded InGaN quantum well (QW) structures with the indium composition increasing then decreasing in a zigzag pattern. Through polarization doping, this naturally creates alternating p-type and n-type regions. Separate structures are designed by varying the number of repeating periods (1 to 3), while maintaining constant overall structure thicknesses. Calculation of the transition probabilities and the electron and hole wave-functions between the conduction band and the valence band reveals a complex energy structure which predicts the photoluminescence peaks for band to band transitions.

4.2 Introduction

Ternary alloys of Group III-N materials are promising materials to be used in future photovoltaic devices due to high thermal conductivity, high optical absorption, and high radiation resistance[1],[2] as well as a direct bandgap tunable over most of the solar spectrum[3], [4]. Studies of the optical properties of InGaN graded structures have been reported, which experimentally determine photoluminescence peaks as being the result of mechanisms such as band to band transitions, impurities, etc., by using power law measurements, for example. In addition, x-ray diffraction of graded structures have been simulated and compared with reciprocal space mapping data. The data claims in low indium composition (17.5, 19.5 and 22.5%) the crystal structure is fully strained but increasing indium composition shows partial

relaxation[5],[6]. Simulation reports for solar cell graded structure predict 28.9% efficiency for a p-GaN/n-In$_x$Ga$_{1-x}$N/n-In$_{0.5}$Ga$_{0.5}$N/p-Si/n-Si tandem structure using realistic material parameters. The thickness and doping concentration of the graded region was found to substantially affect the performance of the cells[7]. Others identified key structural parameters useful for the optimization of InGaN solar cells, as well as accurate estimates of the performances of p-GaN/grad-InGaN/i-In$_{0.53}$Ga$_{0.47}$N/grad-InGaN/n-ZnO where Grad-InGaN corresponds to an InGaN layer with a graded composition[8]. The effects of graded InGaN in LEDs have been studied, and they claim that using a staggered InGaN QW design improves the electron-hole wave function overlap in increasing the radiative recombination rate, R_{sp}, and the radiative efficiency of the QW for LED applications. Using graded structures also reduced the radiative lifetime and thus enhanced the radiative efficiency[9]. At the same time, there have been several recent studies of graded III-nitride films and how they result in doping without impurities, or polarization doping, as a result of a gradient in the internal polarization [10]. This adds a significant functionality to device design for devices made from III-nitride semiconductors [10], [11].

In this study, simulations for one, two and three periodic graded structures have been performed in order to understand their optical properties in respect to the number of periods (wells). The main electron and hole wave functions are calculated in order to determine the observable band-to-band transitions which would be found in photoluminescence experiments. The energies are determined for these maximum probability transitions.

4.3 Structure and simulation method

Nextnano was used to design and study the GaN/In$_x$Ga$_{1-x}$N/In$_y$Ga$_{1-y}$N graded quantum wells. Figure 1 shows the different structures which were graded up and down over 500 nm each

on top of a GaN buffer layer doped n-type at 10^{17} cm^{-3} to match realistic background densities[12]. The maximum In composition in each case is 20%. Sample A is graded up and down once, symmetrically to 20% In. Sample B is graded twice symmetrically, and sample C is graded three times. This effectively results in one, two, and three wells in the structures, respectively.
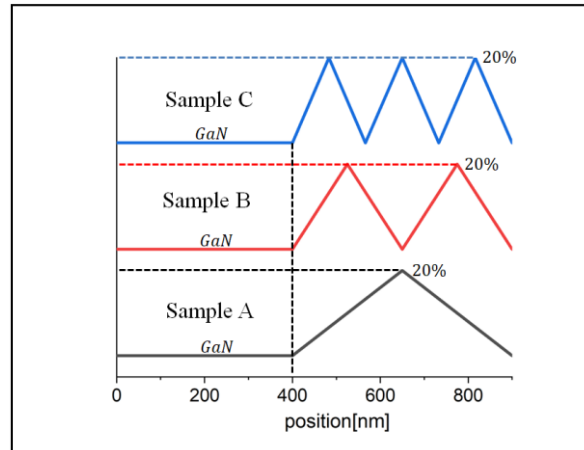
Figure 4. 1. Structure of samples with the given thickness of each layer

As mentioned above, in each graded structure a p-n junction is created. Energy band diagrams confirm this fact. These are shown in Figure 2a. In all samples, there is a depletion region between the GaN buffer layer and the initial graded film due to the intentional background n type doping in the buffer layer. Additionally, degenerate doping is obvious in samples B and C in Figures 1b and 1c, respectively.
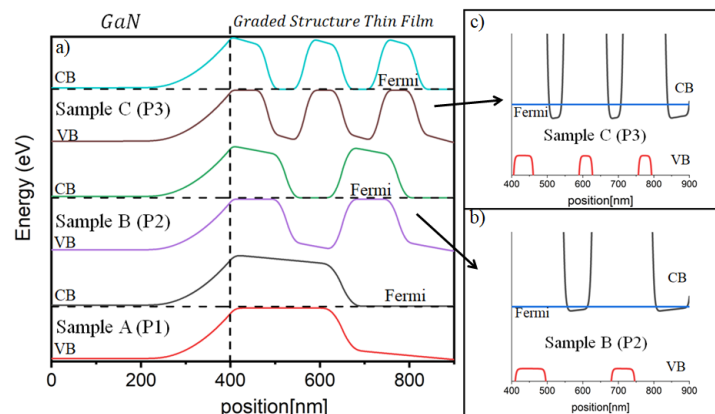
Figure 4. 2. a) Energy-Band diagrams for all samples. P- and n-type doping due to polarization doping can be seen in the graded layers. Additionally, depletion region in interface of GaN buffer layer and thin film is shown. b & c) Degenerate doping for Sample B and C .

For sample A, the electron (hole) ground state wave-functions can be seen inside the structure in figure 3a (3c). Additionally, 3 holes (electrons) which result in the maximal transition probabilities are displayed within the structure in the area overlapping with the ground state electron (hole) wave-function. These are shown on a closer scale in figures 3b (3d) in order to see the structure of the overlapping wave functions.
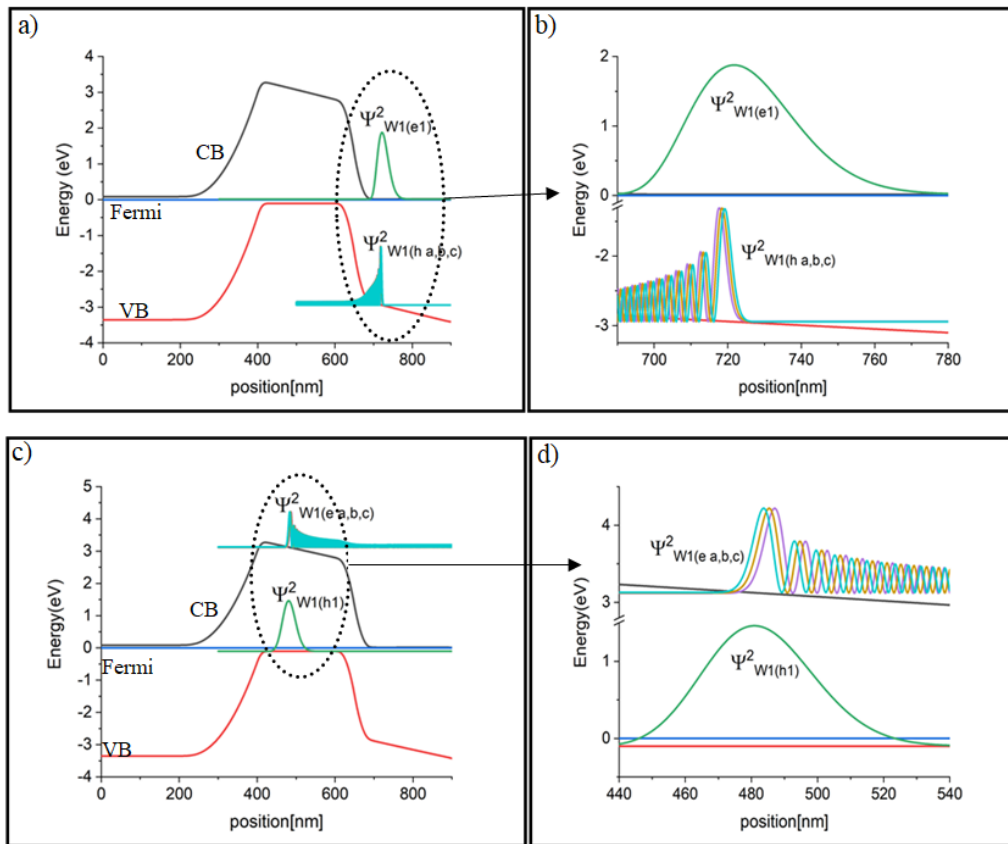
Figure 4. 3. Ground state electron(hole) wave-function with three holes (electrons) which have maximum transition probabilities (a&c respectively). zoom out (b,d).

To predict the photoluminescence due to the ground state electron (hole), transition probabilities between the ground state electron (hole) with all holes (electrons) are considered. The resulting simulated PL is simply the result of the envelope of the non-zero electron-hole

overlap integrals. Figure 4 shows this for both the ground state electron and hole. The transition intensity for the ground state hole is twice more than that of the ground state ground state electron. This is likely due to the electron states being broader and more spread out in Figure 3d resulting in larger overlap integrals. In addition, the simulation shows the energies of maximal transition probabilities for the ground state electron and hole are $E_{W1\ (h1)}$ = 3.2238 eV and$E_{W1\ (e1)}$ = 2.9605 eV, respectively, which would be the predicted PL energies in sample A.
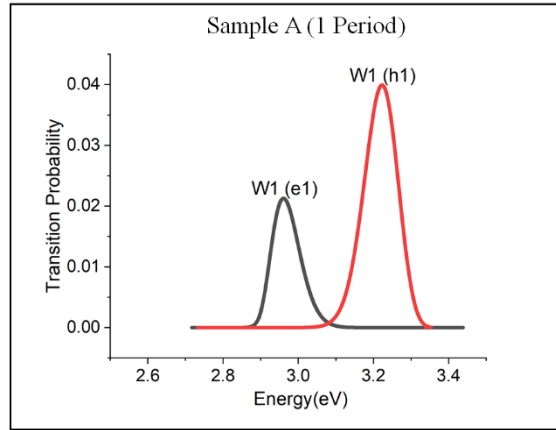
Figure 4. 4. Predicted PL for sample A due to electron and hole ground state.

The same strategy is followed for sample B (2 periods graded structure). The ground state electron (hole) in each well is shown in figure 5a (5b) along with the 3 hole (electron) wavefunctions which result in the most probable transitions.
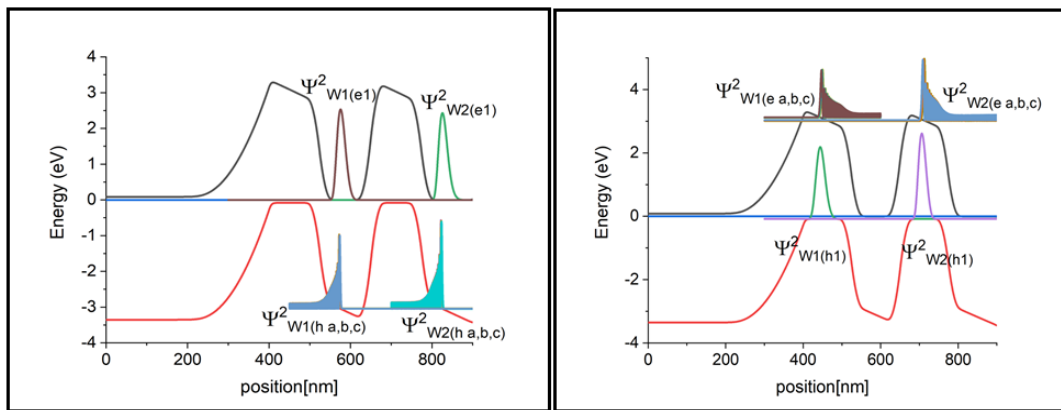
Figure 4. 5. Ground state electron(hole) wave-function with three holes (electrons) which have maximum transition probabilities (a&b) in each well.

Then, to predict the PL for sample B, the transition probabilities of the electron (hole) in each well are calculated with all possible holes (electrons). Four peaks resulting from the envelopes of these transition probabilities are shown in Figure 6. It can be seen here that the transition probabilities of the hole ground states are stronger than the transition probabilities of the electron ground states. In other words, the hole effects in predicted PL are stronger than the electron effects. Like sample A, for sample B, the transition probability for the ground state hole with electrons as well as the ground state electron with holes in each well are given. In addition, the energy of maximum transition probability for ground state electron and hole (for well 1) are $E_{W1\,(h1)} = 3.1311$ eV, $E_{W1\,(e1)} = 3.0336$ eV, respectively. Moreover, for well 2, the energy of maximum transition probability for ground state electron and hole are $E_{W2\,(h1)} = 3.198$ eV and $E_{W2(e1)} = 3.04$ eV, respectively.
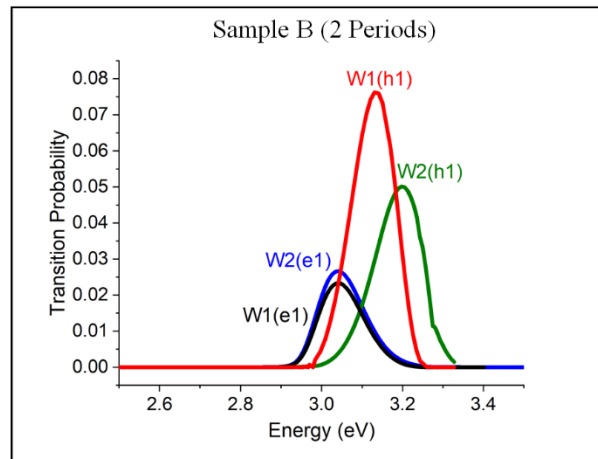
Figure 4. 6. Predicted PL for Sample B (2 Periods) due to transition probability of ground state electrons (holes) in each well.

Similar to the two other samples, figure 7a (7b) shows the wavefunctions of the three ground state electrons (holes) from each well for sample C. And again, as it was shown for samples A and B, the wavefunctions of the three holes (electrons) which demonstrate the maximum transition probabilities are shown in each well.
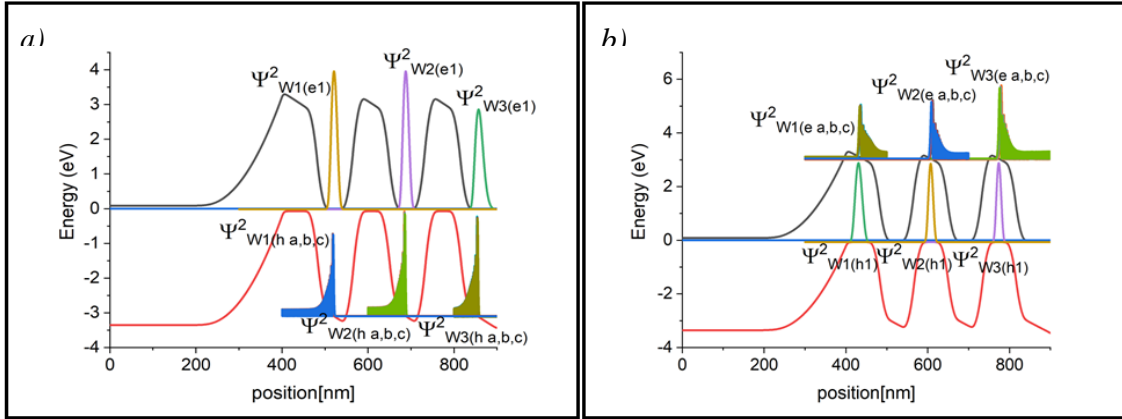
Figure 4. 7. Ground state electron (hole) wave-function with three holes (electrons) which have maximum transition probabilities (a&b respectively) in each well.

Finally, similar to samples A and B the predicted PL for sample C is shown in Figure 8 as the envelopes of the calculated transition probabilities in each well. Here, we see a relative convergence of the luminescence from all of the wells and from both the electrons and holes. For sample C, the transition probability for ground state hole with electrons as well as ground state electron with holes in each well are given. In well 1, the energies of maximal transition probabilities for the ground state electron and hole are $E_{W1\,(h1)} = 3.1811$ eV and $E_{W1\,(e1)} = 3.095$ eV respectively. The same parameter for well 2 is $E_{W2\,(h1)} = 3.108$ eV and $E_{W2(e1)} = 3.075$ eV. Finally, for well 3 the energies of maximal transition probabilities are $E_{W3\,(h1)} = 3.1$ eV and $E_{W2(e1)} = 3.076$ eV. For well 1, the transition intensity for the ground state hole is almost twice more than that of the ground state.
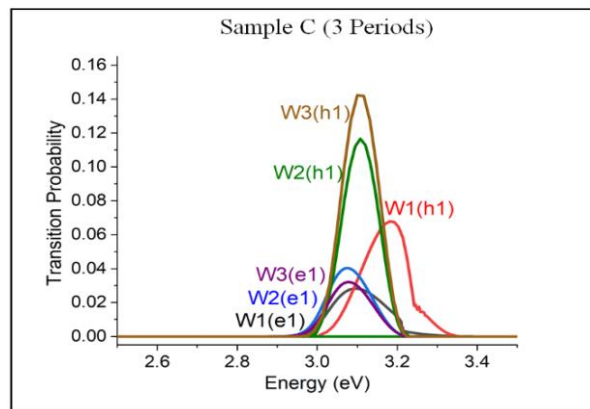
Figure 4. 8. Predicted PL for Sample C (three wells) due to transition probability of ground state electrons (holes) in each well.

The above details for the predicted PL from all of the samples show the ground state electron in well 1 shifted to higher energies, however this energy for the ground state hole in well 1 decreases in sample B and again increases in sample C. Additionally, the PL due to the ground state electron in well 2 is increasing from sample B to sample C. However, the PL due to the holes in the wells is decreasing from sample B to sample C. Furthermore, for all samples, the PL due to the ground state hole in all wells occurs at higher energies than the electrons in the same well.

4.4 Conclusion

The predicted PL for sample A shows two peaks including transitions between the ground state electron with all of the possible holes and the ground state hole with all of the possible electrons. However, for sample B the predicted PL due to 2 electrons and 2 holes in the two wells should show 4 peaks, but convergence of these peaks displays only three, because the peak energies for the electrons in well 1 and 2 are nearly degenerate. There are 6 peaks due to 3 electrons and 3 holes in 3 wells in sample C which are all nearly the same energies. These results should be of interest to the community developing optoelectronic device structures out of III-N materials.

4.5 References

[1]   S. Nakamura et al., "InGaN-Based Multi-Quantum-Well-Structure Laser Diodes," Jpn. J. Appl. Phys. 35(Part 2, No. 1B), L74–L76 (1996) [doi:10.1143/JJAP.35.L74].

[2]   G. Pozina et al., "Origin of multiple peak photoluminescence in InGaN/GaN multiple quantum wells," J. Appl. Phys. 88(5), 2677–2681 (2000) [doi:10.1063/1.1287124].

[3]   A. G. Bhuiyan et al., "InGaN Solar Cells: Present State of the Art and Important Challenges," IEEE J. Photovolt. 2(3), 276–293 (2012) [doi:10.1109/JPHOTOV.2012.2193384].

[4]   A. David and M. J. Grundmann, "Influence of polarization fields on carrier lifetime and recombination rates in InGaN-based light-emitting diodes," Appl. Phys. Lett. 97(3), 033501 (2010) [doi:10.1063/1.3462916].

[5]   M. Sarollahi et al., "Luminescence Properties of GaN/InxGa1−xN/InyGa1−yN Double Graded Structures (Zigzag Quantum Wells)," J. Electron. Mater. 49(6), 3512–3519 (2020) [doi:10.1007/s11664-020-08033-w].

[6]   P. K. Ghosh et al., "Investigation of the Structural and Optical Properties of Compositionally V-Graded Strained In x Ga 1− x N Layers," Phys. Status Solidi B 257(4), 1900591 (2020) [doi:10.1002/pssb.201900591].

[7]   G. F. Brown et al., "Finite element simulations of compositionally graded InGaN solar cells," Sol. Energy Mater. Sol. Cells 94(3), 478–483 (2010) [doi:10.1016/j.solmat.2009.11.010].

[8]   V. Gorge et al., "Theoretical analysis of the influence of defect parameters on photovoltaic performances of composition graded InGaN solar cells," Mater. Sci. Eng. B 178(2), 142–148 (2013) [doi:10.1016/j.mseb.2012.10.033].

[9]   H. P. Zhao et al., "Design and characteristics of staggered InGaN quantum-well light-emitting diodes in the green spectral regime," IET Optoelectron. 3(6), 283–295 (2009) [doi:10.1049/iet-opt.2009.0050].

[10]   P. Kivisaari, J. Oksanen, and J. Tulkki, "Polarization doping and the efficiency of III-nitride optoelectronic devices," Appl. Phys. Lett. 103(21), 211118 (2013) [doi:10.1063/1.4833155].

[11]   S. Li et al., "Polarization induced pn-junction without dopant in graded AlGaN coherently strained on GaN," Appl. Phys. Lett. 101(12), 122103 (2012) [doi:10.1063/1.4753993].

[12]   T. Tingberg, T. Ive, and A. Larsson, "Investigation of Si and O Donor Impurities in Unintentionally Doped MBE-Grown GaN on SiC(0001) Substrate," J. Electron. Mater. 46(8), 4898–4902 (2017) [doi:10.1007/s11664-017-5484-y].

<div align="center">

CHAPTER 5

Study of simulations of double graded InGaN solar cell structures

</div>

Authors: Mirsaeid. Sarollahi, Mohammad Zamani Alavijeh, Manal A. Aldawsari, Rohith Allaparthi, Reem Alhelais, , Malak A. Refaei, Md Helal Uddin Maruf , Yuri Mazur, Morgan E. Ware

5.1 Abstract

The performances of various configurations of InGaN solar cells are compared using nextnano semiconductor simulation software. Here we compare a flat base-graded wall GaN/InGaN structure, with an $In_xGa_{1-x}N$ well with sharp GaN contact layers, and an $In_xGa_{1-x}N$ structure with $In_xGa_{1-x}N$ contact layers, i.e. a homojunction. The doping in the graded structures is the result of polarization doping at each edge (10 nm from each side) due to the compositional grading, while the well structures and homojunctions are impurity doped at each edge (10 nm from each side) at levels equal to the polarization doping density in the graded structure with similar maximum indium concentration. The solar cells are characterized by their open-circuit voltage, V_{oc}, short circuit current, I_{sc}, solar efficiency, η, and energy band diagram. The results indicate that an increase in I_{sc} and η results from increasing both the fixed and the maximum indium compositions, while the V_{oc} decreases. The maximum efficiency is obtained for the InGaN well with 60% In.

5.2 Introduction

The optical properties of InGaN ternary alloys make them interesting materials for photovoltaic devices.[1]–[3]. Properties such as direct and tunable bandgaps which cover the whole range of the solar spectrum as well as high thermal conductivity, high optical absorption, and high radiation resistance are center to this interest.[4],[5] As a result, InGaN continues to

receive attention in the research community both fundamentally and with a strong push towards photovoltaics.[6]–[9] However, there are still fundamental difficulties in the growth and processing of this material, which prevents its use. Two main problems in particular are p-type doping and strain and relaxation of high indium concentration alloys. There have been many theoretical studies of single composition InGaN solar cells. For example, in 2007, modeling optimization of a thick, single junction $In_{0.65}Ga_{0.35}N$ solar cell achieved a conversion efficiency of 20.28%.[10] In another report (in 2008), they obtained higher efficiency (24.95%) with the same indium composition due to adoption of the density of states (DOS) model, providing much more information about recombination/generation in semiconductors than the lifetime model by neglecting defects.[11] These are similar to several other studies of InGaN solar cells, which use different modeling software to report solar efficiency.[12] Other predictions have been made using first principles modelling of InGaN homojunction solar cells by varying the indium content and thickness of the p-InGaN contact layer. For example, it was demonstrated that a 100 nm thick p-n InGaN solar cell under AM1.5G illumination could have a maximum efficiency of ~21.5%.[13]

Historically, graded structures, generally only consisting of a single grade, were studied for their strain relieving properties.[14] Ternary graded films in III-nitride materials have additionally resulted in polarization doping which has been demonstrated to achieve very high levels of doping, without the use of additional impurities in the lattice.[15] This feature is result of different spontaneous crystal polarizations, P, in InN and GaN. In a metal polar, graded structure, with increasing indium composition from GaN to InGaN, a negative background charge is created due to the changing polarization ($-\nabla.P=\rho < 0$), resulting in a p-type layer by attracting holes. The reverse compositional grade, from InGaN to GaN, then results in a positive

background charge, which attracts electrons forming an n-type layer.[16] Polarization doping for AlGaN generally results in the opposite doping type. I.e., by increasing (decreasing) the aluminum composition from GaN to AlGaN (AlGaN to GaN), the graded layer is n- (p-) type.[17],[18]. The III-nitrides are also strong piezoelectric materials, and as such, the changing piezoelectric polarization as the alloy composition changes is generally considered along with the spontaneous polarization component mentioned above. [19]

Here, we present a simulation study of graded and sharp barrier, GaN/InGaN devices compared with single junction InGaN solar cells, where the active regions are formed by a single composition InGaN layer and the contact layers are either compositionally graded InGaN (polarization doped), GaN (impurity doped), or InGaN (impurity doped). The structures in this work are shown in Fig. 1 using 50% indium as an example. These are 100 nm thick p-i-n type structures made from $In_xGa_{1-x}N$ with three different configurations. The first structure, Fig. 1a, is a flat base-graded barrier structure in which a single layer with constant x is sandwiched between two graded barrier layers.

The first graded layer (from 0-10 nm) starts from 0% indium and is graded to a maximum value, x_{max}, over 10 nm, then it is followed by an 80 nm flat base layer of constant composition, x_{max}, and finally (90-100 nm) the composition is graded back to 0%. This is Structure A and called a flat base graded (FBG) structure with polarization doped contact layers forming the p-i-n device. In addition, the energy band diagram related to structure A (for $x_{max} = 50\%$ at zero volts) is shown in Fig. 1b. The doping concentration resulting from the polarization doping as a function of x_{max} in the graded layers is shown in Fig.1g. Structure B, Fig. 1c, is a wide square well, with two doped GaN layers at each edge. The GaN layers are 10 nm thick each (0-10 nm and 90-100 nm) and doped at a level to match that of the polarization doping in Structure A. The

InGaN is 80 nm thick (10-90 nm). The energy band diagram of Structure B (for x =50% at zero volts) is displayed in Fig. 1d showing the two doped GaN edges. In addition, there are two sheet charge layers at each interface between InGaN and GaN effectively acting as traps and resulting from the sudden polarization change at the beginning (at 10 nm) and at the end (at 90 nm). Structure C, Fig. 1e, is a 100 nm $In_xGa_{1-x}N$ homojunction, with $x=x_{max}$. The energy band diagram of Structure C (for x =50% at zero volts) is shown in Fig. 1f and does not show any significant barriers into the ohmic contacts with the edges doped intentionally. In summary, Structures A, B, and C will be referred to as: Flat Base Graded (FBG), Square Well (SW), and Homojunction (HMJ), respectively.
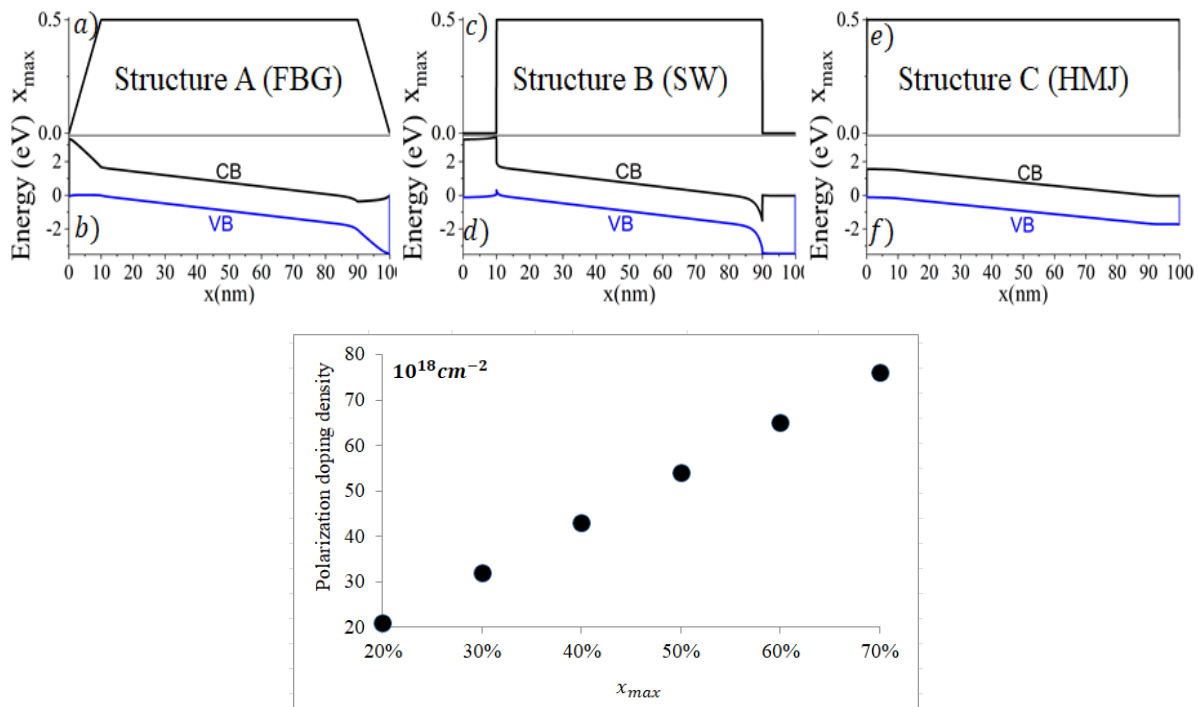
Figure 5. 1. a) Flat base graded well structure (Structure A) b) energy band diagram for Structure A , c) Single square well GaN/InGaN (Structure B) d) energy band diagram for Structure B e) Single InGaN homojunction (Structure C) f) energy band diagram for structure C. g) Polarization-doping correlated with indium composition in Structure A

5.3 Nextnano simulation

Using nextnano, the band structure was modeled using a single-band effective mass approximation.[20] For solar cell calculations, the generation rates for every layer of the structure must be determined. Nextnano, however is limited to calculations of generation rates for fixed composition materials only, within a single simulation. Therefore, generation rates for variable composition films must be determined in a step-graded procedure, semi-manually [21].Total generation versus position can then be imported into the nextnano+ simulation of the full graded structure in order to calculate the light *J-V* curves and other solar cell parameters.
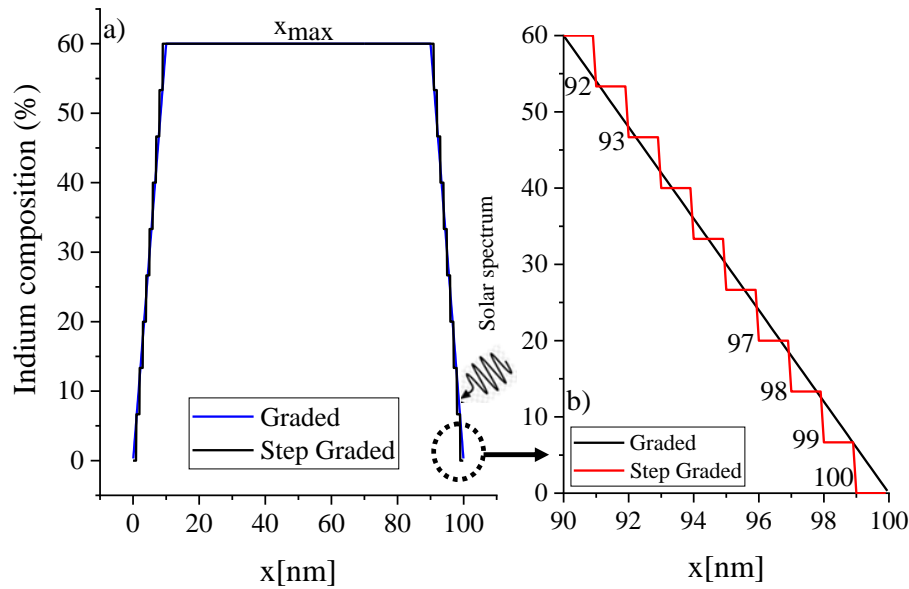
Figure 5. 2.a) Converting graded structure to step graded to calculate generation rate in nextnano, b) Receptivity of layers is given by the number next each layer when light passing through the structure between 90-100 nm.

In order to determine these generation rates, the graded regions of the FBG structures were parameterized as shown in Fig. 2 into step-graded layers with steps of 1 nm thicknesses. The generation rates for each layer was then determined separately. In order to justify this step-graded parameterization, we have used different step sizes for select calculations to demonstrate

convergence to a virtual step size of 0 nm. Throughout the range of step sizes examined, using the x_{max}=60% structure as a representative sample, the open circuit voltages remain virtually unchanged, however the short circuit current, J_{sc}, and the resulting solar cell efficiency, η, did evolve with step size. Generally, as the step size decreases, both J_{sc} and η decrease, however they appear to converge to values within ~1% of the reported values. So, we assume the 1 nm step size is a relatively good approximation of the continuously graded values given the significant savings in computational time as the step sizes become smaller. With this step-graded structure, the generation rates are calculated first by determining the spectrum and intensity of light incident on each step after having interacted with and being partially absorbed by the previous step. We begin with the solar spectrum with intensity, I_0; first entering the structure through layer 100, which here is 1 nm of GaN (see Fig. 2b). The solar spectrum along with the absorption coefficient of layer 100 is imported into nextnano3 in order to calculate the generation rate for that layer. The same procedure is followed for each subsequent layer by considering the light intensity, which is diminished by passing each previous layer, and the absorption coefficient for the alloy and strain of the next layer. This full dataset is then imported into nextnano+ and used as the generation rate data for the entire, continuous structure, in order to determine the solar cell parameters.

5.4 Absorption coefficient and generation rate

The quality of InGaN devices strongly depends on the substrate used in growth. Due to lattice mismatch between GaN and InGaN, strain resulting from the growth of these types of heterostructures can also have a significant impact on the properties and quality of the resulting devices. Heterostructures made of semiconductor materials with different lattice constants are subject to elastic deformations. Such deformations can be studied based on classical elasticity

within the harmonic approximation, (i.e. for small strains). As lattice deformation varies with the growth direction, a detailed understanding of the strain is important for design, development, and study of optoelectronic and electronic devices[22].

Strain causes piezoelectric effects and influences the conduction and valence band edges (including their degeneracies) as well as the k.p Hamiltonian of the Schrodinger equation. Additionally, other parameters correlating with the bandgap are affected like the absorption coefficient. Therefore, strain is a very important parameter for device engineers to modify and control the electronic and optical properties of semiconductor heterostructure [22]. In order to model the absorption coefficients of the continuously varying InGaN alloys, the bandgap energies are required. Strain and the resulting piezoelectric and spontaneous polarizations are taken into account in nextnano,[23],[24] So nextnano was used to predict the bandgap values for $In_xGa_{1-x}N$ strained to a GaN substrate. However, in the absence of strain, a simple Vegard's law relationship with bowing parameter, b, was used to determine the energy bandgap. Different reports have resulted in a large inconsistency in bowing parameters between 1.4-3 eV.[25]–[29] The nextnano database uses a value of b = 1.4 eV.[30] We adopt this value here. For the strained bandgaps we fit a quadratic in x, relationship to the output of nextnano arriving at an analytic representation, which is shown in equation (1):[21]

$$E_g \, (strain) \, (x) = -0.49286x^2 - 3.27153x + 3.43805 \qquad \text{Equation 5. 1}$$

With some analysis, it is found that Eq. 1 predicts that for $In_xGa_{1-x}N$ strained to GaN, with $x > {\sim}0.9$ the bandgap is negative. This concept won't be discussed further here except that this is a potentially novel area of research for this material as in topological insulators and semimetals.[31],[32] Further simulations here will be restricted to $x <= 0.7$ in order to strictly

avoid this range. However, prior modeling work calculated solar cell parameters for both relaxed and strained features for a Λ graded InGaN structure up to 90%.[21].

The absorption coefficient, $\alpha(\lambda)$, for bulk or relaxed material can be parameterized as in Ref.[33] using two parameters, $a(x)$ and $b(x)$, which are determined by fitting α over the entire composition range assuming unstrained, bulk material.

Then, the energy bandgap and the absorption coefficients are both available as functions of the indium composition over the entire range of the alloy [21]. These were combined numerically to determine the absorption coefficients as functions of the bandgap for any possible bandgap obtained by $In_xGa_{1-x}N$, allowing for the possibility for the bandgap changing with strain. The resulting absorption coefficients vs wavelength for a range of x for $In_xGa_{1-x}N$ strained to the GaN lattice constant is shown in Fig. 3a. The bandgap for this strained material predicted by Eq. 1 for $x > \sim70\%$ becomes less than ~0.7 eV, which is the bandgap of relaxed InN. And, since the original absorption data resulting in the fitting parameters [33], were acquired from relaxed material including InN, we will restrict the following discussion to only alloys for which $x \leq$ 70% in order to maintain the connection to real experimental data. In this work, all structures are strained to the GaN lattice parameter.

As a result, we can show the light intensity transmitted to any depth of material for each alloy. This is shown in Fig.3b, using AM1.5G as the incident solar spectrum. It can be seen here that the transmission effectively reaches a steady condition once a significant portion of the above bandgap light has been absorbed, and after which only a small amount of additional light is absorbed. For all alloys here, that depth is below ~500 nm, but becomes much smaller with decreasing In composition.
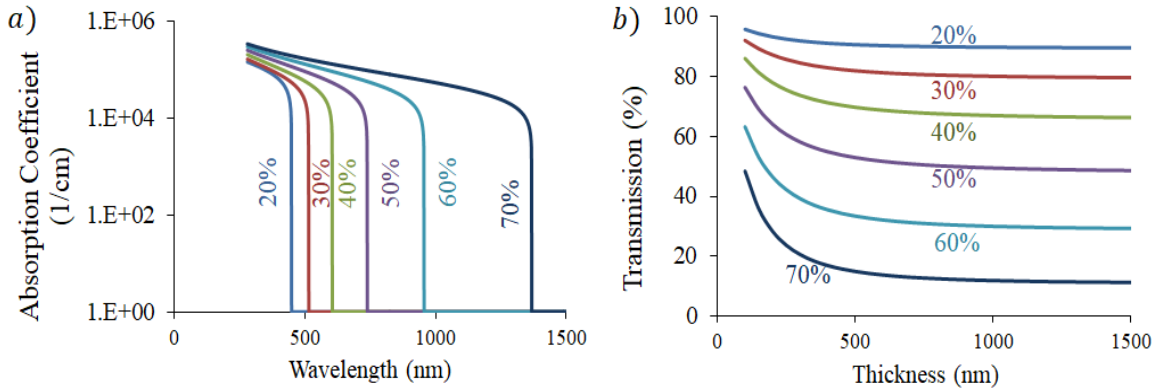
Figure 5. 3. a) Absorption coefficient under strain for different indium alloys (20 to 70%). b) The amount of total light transmitted to a certain depth for (20 to 70%) in FBG.

Finally, the generation rates can be calculated for each layer using AM1.5G (100 mW/cm^2) standard solar illumination (Fig. 4), and then imported into nextnano.
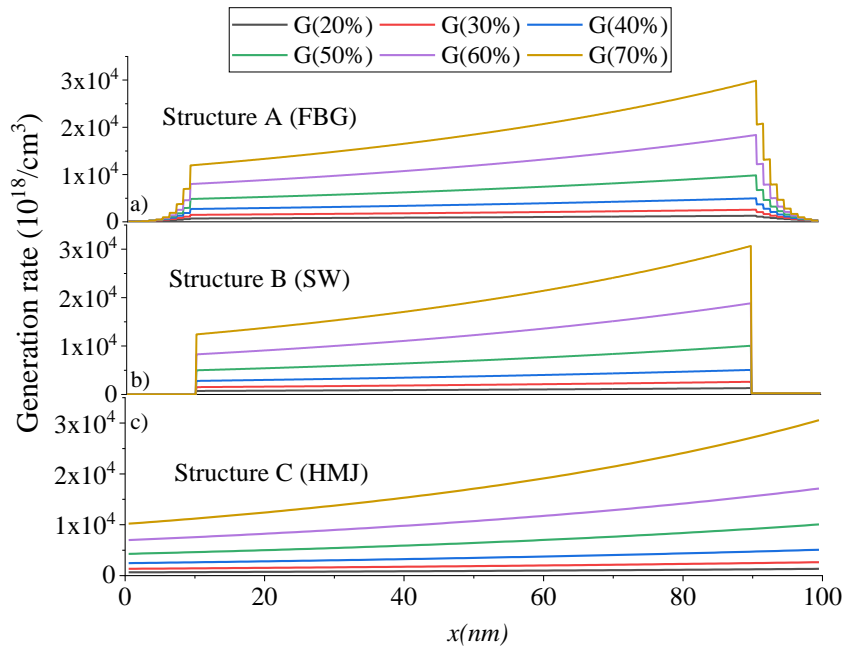
Figure 5. 4. a) Generation rate for structures A, b) structure B, and c) structure C.

5.5 Illuminated J-V curve, solar cell parameters

With these G profiles imported into nextnano+, accurate simulations of the *J-V* characteristics can be performed under AM1.5G (100 mW/cm^2) standard solar illumination, at

300 K, (room temperature). These are shown in Figs. 5a-c for all of the studied structures, with the $x = 0.6$ and 0.7 samples plotted again in Fig. 5d for comparison. These curves were then used to determine the fill factors and solar cell efficiencies manually.
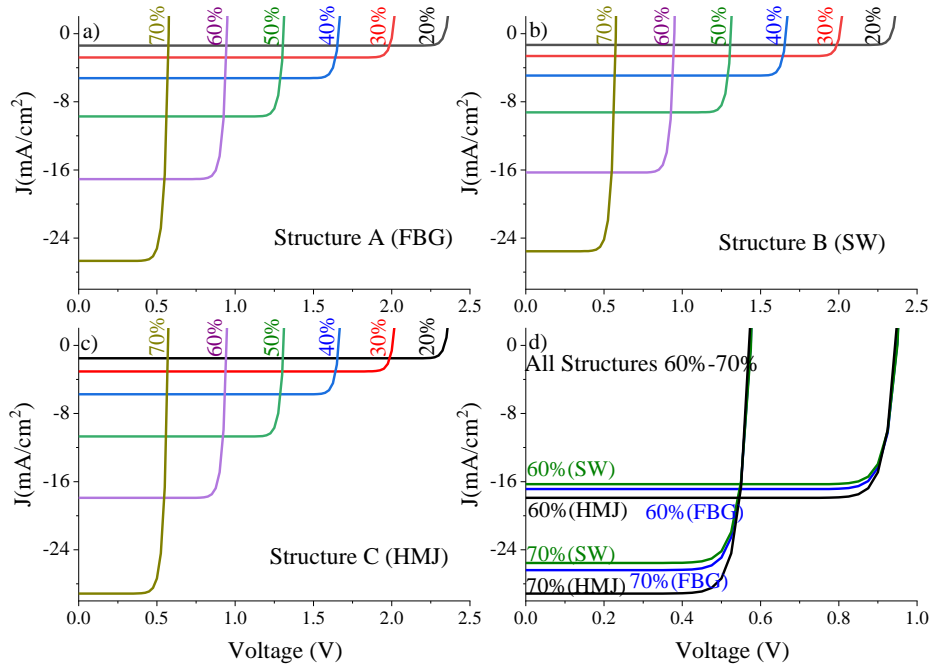
Figure 5. 5. Illuminated *JV* curve for a) structure A, b) structure B, c) structure C. In d) all structures at 60%-70% are shown for comparison.

As expected, by increasing the indium composition and thus decreasing the effective bandgaps, V_{oc} generally decreases as seen in Fig. 6. Any variation in the V_{oc} for different structures of the same composition is contained within the size of the data points. V_{oc} is tightly controlled by the bandgap. However, at the same time, the short circuit current density, J_{sc}, is found to increase with the indium. See Fig. 7.
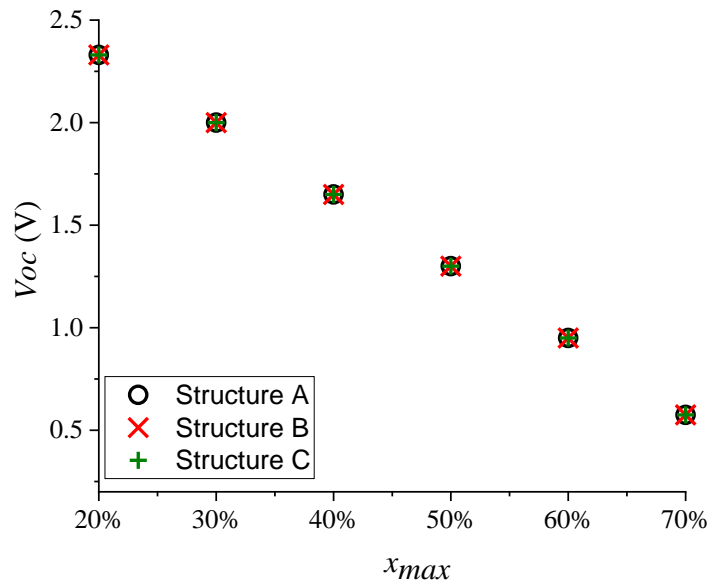
Figure 5. 6. Open Circuit voltage for three structures

Determination of the Fill Factor (*FF*) requires a little more effort. It is defined as the ratio between the maximum power ($P_{max} = J_m V_m$) created by the solar cell and $J_{sc}V_{oc}$ as follows.
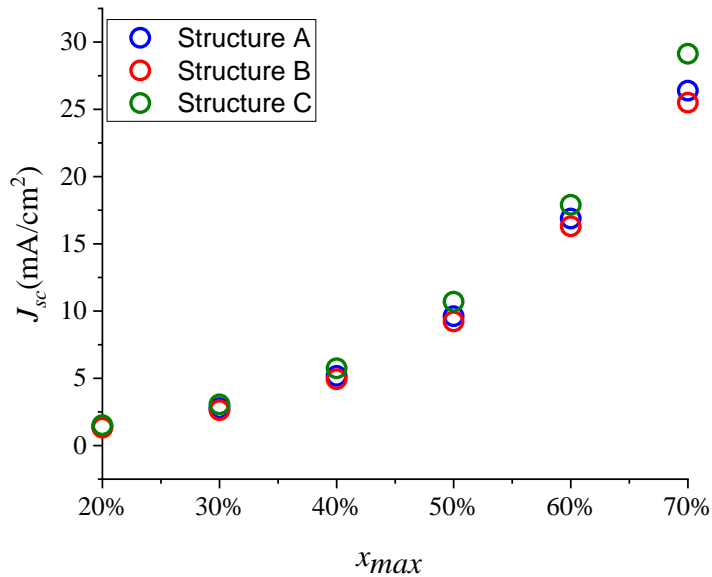
Figure 5. 7. Short circuit current density, J_{sc}, for the three structures

$$FF = J_m \cdot V_m / J_{sc} \cdot V_{oc} \qquad\qquad \text{Equation 5. 2}$$

The *FF*, shown in Fig.8, decreases with increasing indium composition in all structures with a maximum of ~95% at *x*=20%, and minimum values around 80% for at *x*=70%.
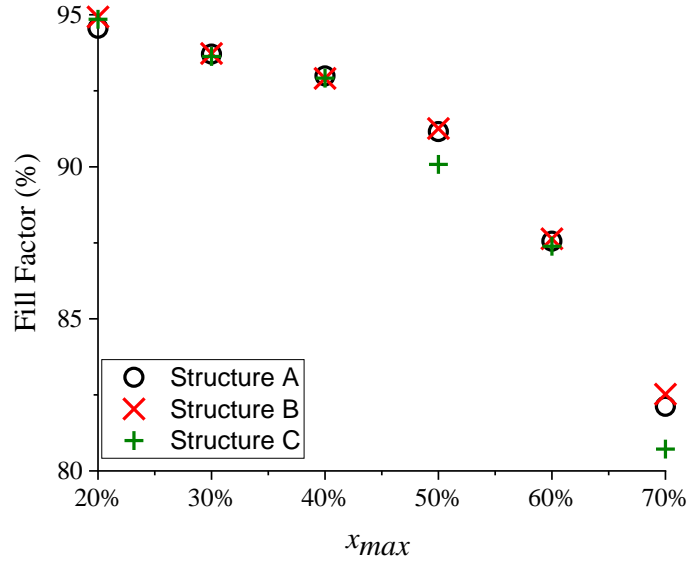
Figure 5. 8. Fill Factor comparison for 3 structures

Finally, the solar efficiency, Fig. 9, is defined as the part of the energy in the form of sunlight that gets converted to electricity by the solar cell and is given by:
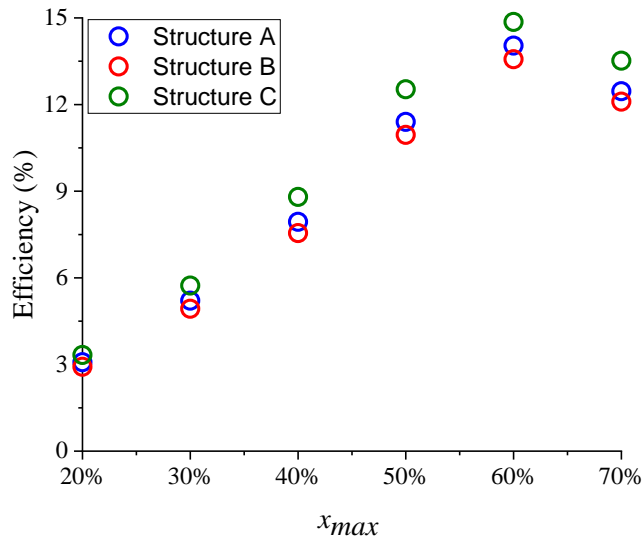
Figure 5. 9. Solar efficiency for all structures

$$\eta = P_{max}/P_{in} = P_{max}/100 \text{ , which } P_{max}=FF.J_{sc}.V_o \qquad \text{Equation 5. 3}$$

The solar efficiency, η, for all structures shows maximum values at $x = 0.6$ which are

14.18%, 13.57% and 14.86%, respectively for structures A, B, and C. These are noticeably lower

than some other reports due the significantly thinner structure of only 100 nm as compared to

nearly 500nm in Ref. [34], however demonstration of the maximum efficiency for $x_{max} = \sim 60\%$

is similar to reports of similar simulations.[13],[33] In general, we have, $\eta_{(Structure\ C)} > \eta_{(Structure\ A)}$

$> \eta_{(Structure\ B)}$. So, we find that structure C, a simple homojunction, provides for the most efficient

solar cell. This is likely not surprising, however physically growing structure C to high quality

would be challenging. At the same time, structure A has been demonstrated to be grown at a

high quality[35], while its performance is not substantially worse that structure C.

5.6 Conclusion

Although, at 60% indium composition the efficiency of structure C (homojunction) is

larger than structure A (FBG well), there are advantages in designing and using graded layers in

the contact regions. One of the most significant advantages of structure A is the formation of the

p- and n-type contact layers due to polarization doping. This is mainly due to that fact that p-type

doping in most III-V semiconductors is challenging, and in the III-nitrides it remains extremely

inefficient. In addition, when compared to structure B, which would be considered a traditional

solar cell homojunction, i.e., InGaN on a GaN substrate, with a GaN cap, the grading in the

contact layers allows for some amount of the strain to be mediated in going from a GaN substrate

to the InGan film. This compounds the impact of the improvement in efficiency of structure A

over B. Moreover, the encouraging results for the FBG structure (structure A) creates

opportunities for future studies for this structure such as changing the thickness of the flat base

layer, changing the shoulders (graded layers) symmetrically and asymmetrically in order to obtain even more optimized structures. Additionally, it has been shown in many varying materials systems that growing a graded composition buffer layer can enable the growth of much higher lattice mismatched layers than simply growing directly on a highly mismatched substrate. Finally, we have also calculated the effect of strain on the absorption coefficient and the energy band-gap, creating a Vegard's law-like relation for the bandgap of InGaN strained to a GaN substrate. This predicts a novel negative bandgap.

5.7 References

[1]   S. Nakamura, M. Senoh, N. Iwasa, S. Nagahama, T. Yamada, and T. Mukai, "Superbright Green InGaN Single-Quantum-Well-Structure Light-Emitting Diodes," *Jpn. J. Appl. Phys.*, vol. 34, no. Part 2, No. 10B, pp. L1332–L1335, Oct. 1995, doi: 10.1143/JJAP.34.L1332.

[2]   S. Nakamura *et al.*, "InGaN-Based Multi-Quantum-Well-Structure Laser Diodes," *Jpn. J. Appl. Phys.*, vol. 35, no. Part 2, No. 1B, pp. L74–L76, Jan. 1996, doi: 10.1143/JJAP.35.L74.

[3]   G. Pozina, J. P. Bergman, B. Monemar, T. Takeuchi, H. Amano, and I. Akasaki, "Origin of multiple peak photoluminescence in InGaN/GaN multiple quantum wells," *J. Appl. Phys.*, vol. 88, no. 5, pp. 2677–2681, Sep. 2000, doi: 10.1063/1.1287124.

[4]   A. G. Bhuiyan, K. Sugita, A. Hashimoto, and A. Yamamoto, "InGaN Solar Cells: Present State of the Art and Important Challenges," *IEEE J. Photovolt.*, vol. 2, no. 3, pp. 276–293, Jul. 2012, doi: 10.1109/JPHOTOV.2012.2193384.

[5]   A. David and M. J. Grundmann, "Droop in InGaN light-emitting diodes: A differential carrier lifetime analysis," *Appl. Phys. Lett.*, vol. 96, no. 10, p. 103504, Mar. 2010, doi: 10.1063/1.3330870.

[6]   G. F. Brown, J. W. Ager, W. Walukiewicz, and J. Wu, "Finite element simulations of compositionally graded InGaN solar cells," *Sol. Energy Mater. Sol. Cells*, vol. 94, no. 3, pp. 478–483, Mar. 2010, doi: 10.1016/j.solmat.2009.11.010.

[7]   X. M. Cai *et al.*, "Study of InGaN/GaN Multiple Quantum Well Solar Cells With Different Barrier Thicknesses," *Phys. Status Solidi A*, vol. 215, no. 10, p. 1700581, May 2018, doi: 10.1002/pssa.201700581.

[8]   E. Vadiee *et al.*, "InGaN solar cells with regrown GaN homojunction tunnel contacts," *Appl. Phys. Express*, vol. 11, no. 8, p. 082304, Aug. 2018, doi: 10.7567/APEX.11.082304.

[9] S. R. Routray and T. R. Lenka, "InGaN-based solar cells: a wide solar spectrum harvesting technology for twenty-first century," *CSI Trans. ICT*, vol. 6, no. 1, pp. 83–96, Mar. 2018, doi: 10.1007/s40012-017-0181-9.

[10] Z.-H. Zhang *et al.*, "InGaN/GaN multiple-quantum-well light-emitting diodes with a grading InN composition suppressing the Auger recombination," *Appl. Phys. Lett.*, vol. 105, no. 3, p. 033506, Jul. 2014, doi: 10.1063/1.4891334.

[11] X. Shen *et al.*, "Simulation of the InGaN-based tandem solar cells," San Diego, CA, Aug. 2008, p. 70450E. doi: 10.1117/12.793997.

[12] F. Bouzid and L. Hamlaoui, "Investigation of InGaN/Si double junction tandem solar cells," *J. Fundam. Appl. Sci.*, vol. 4, no. 2, p. 108, Sep. 2015, doi: 10.4314/jfas.v4i2.1.

[13] S.-W. Feng, C.-M. Lai, C.-Y. Tsai, Y.-R. Su, and L.-W. Tu, "Modeling of InGaN p-n junction solar cells," *Opt. Mater. Express*, vol. 3, no. 10, p. 1777, Oct. 2013, doi: 10.1364/OME.3.001777.

[14] E. A. Fitzgerald *et al.*, "Totally relaxed Ge $_x$ Si $_{1-x}$ layers with low threading dislocation densities grown on Si substrates," *Appl. Phys. Lett.*, vol. 59, no. 7, pp. 811–813, Aug. 1991, doi: 10.1063/1.105351.

[15] F. K. LeGoues, B. S. Meyerson, J. F. Morar, and P. D. Kirchner, "Mechanism and conditions for anomalous strain relaxation in graded thin films and superlattices," *J. Appl. Phys.*, vol. 71, no. 9, pp. 4230–4243, May 1992, doi: 10.1063/1.350803.

[16] Y.-J. Lee, Y.-C. Yao, and Z.-P. Yang, "Numerical Analysis on Polarization-Induced Doping III-Nitride n-i-p Solar Cells," *IEEE Photonics J.*, vol. 7, no. 1, pp. 1–9, Feb. 2015, doi: 10.1109/JPHOT.2015.2392374.

[17] S. Li *et al.*, "Polarization induced pn-junction without dopant in graded AlGaN coherently strained on GaN," *Appl. Phys. Lett.*, vol. 101, no. 12, p. 122103, Sep. 2012, doi: 10.1063/1.4753993.

[18] J. Simon, V. Protasenko, C. Lian, H. Xing, and D. Jena, "Polarization-Induced Hole Doping in Wide–Band-Gap Uniaxial Semiconductor Heterostructures," *Science*, vol. 327, no. 5961, pp. 60–64, Jan. 2010, doi: 10.1126/science.1183226.

[19] D. Jena *et al.*, "Polarization-engineering in group III-nitride heterostructures: New opportunities for device design: Polarization engineering in III-V nitride heterostructures," *Phys. Status Solidi A*, vol. 208, no. 7, pp. 1511–1516, Jul. 2011, doi: 10.1002/pssa.201001189.

[20] "qcl:electronic_band_structure [nextnano.NEGF - Software for Quantum Transport]." https://nextnano-

docu.northeurope.cloudapp.azure.com/dokuwiki/doku.php?id=qcl:electronic_band_structur
e (accessed Oct. 05, 2021).

[21] M. Sarollahi *et al.*, "Modeling of Λ-graded InxGa1−xN solar cells: comparison of strained and relaxed features," *J. Photonics Energy*, vol. 12, no. 02, Apr. 2022, doi: 10.1117/1.JPE.12.022205.

[22] S. Birner *et al.*, "Modeling of Semiconductor Nanostructures with nextnano [3]," *Acta Phys. Pol. A*, vol. 110, no. 2, pp. 111–124, Aug. 2006, doi: 10.12693/APhysPolA.110.111.

[23] "1D strain." https://www.nextnano.de/nextnano3/tutorial/1Dtutorial10.htm (accessed Apr. 13, 2021).

[24] "1D piezo." https://www.nextnano.de/nextnano3/tutorial/1Dtutorial6.htm (accessed Apr. 13, 2021).

[25] M. Kurouchi, T. Araki, H. Naoi, T. Yamaguchi, A. Suzuki, and Y. Nanishi, "Growth and properties of In-rich InGaN films grown on (0001) sapphire by RF-MBE," *Phys. Status Solidi B*, vol. 241, no. 12, pp. 2843–2848, Oct. 2004, doi: 10.1002/pssb.200405121.

[26] M. D. McCluskey, C. G. Van de Walle, C. P. Master, L. T. Romano, and N. M. Johnson, "Large band gap bowing of InxGa1−xN alloys," *Appl. Phys. Lett.*, vol. 72, no. 21, pp. 2725–2726, May 1998, doi: 10.1063/1.121072.

[27] M. Moret *et al.*, "Optical, structural investigations and band-gap bowing parameter of GaInN alloys," *J. Cryst. Growth*, vol. 311, no. 10, pp. 2795–2797, May 2009, doi: 10.1016/j.jcrysgro.2009.01.009.

[28] J. Wu, "When group-III nitrides go infrared: New properties and perspectives," *J. Appl. Phys.*, vol. 106, no. 1, p. 011101, Jul. 2009, doi: 10.1063/1.3155798.

[29] S. N. Alam, V. Z. Zubialevich, B. Ghafary, and P. J. Parbrook, "Bandgap and refractive index estimates of InAlN and related nitrides across their full composition ranges," *Sci. Rep.*, vol. 10, no. 1, p. 16205, Dec. 2020, doi: 10.1038/s41598-020-73160-7.

[30] I. Vurgaftman and J. R. Meyer, "Band parameters for nitrogen-containing semiconductors," *J. Appl. Phys.*, vol. 94, no. 6, pp. 3675–3696, Sep. 2003, doi: 10.1063/1.1600519.

[31] V. I. Litvinov, "Quantum anomalous Hall state with Chern number C = 2 in wurtzite quantum wells," *Phys. Rev. B*, vol. 104, no. 24, p. 245304, Dec. 2021, doi: 10.1103/PhysRevB.104.245304.

[32] M. S. Miao, Q. Yan, C. G. Van de Walle, W. K. Lou, L. L. Li, and K. Chang, "Polarization-Driven Topological Insulator Transition in a GaN / InN / GaN Quantum Well," *Phys. Rev. Lett.*, vol. 109, no. 18, p. 186803, Nov. 2012, doi: 10.1103/PhysRevLett.109.186803.

[33] R. Belghouthi, S. Taamalli, F. Echouchene, H. Mejri, and H. Belmabrouk, "Modeling of polarization charge in N-face InGaN/GaN MQW solar cells," *Mater. Sci. Semicond. Process.*, vol. 40, pp. 424–428, Dec. 2015, doi: 10.1016/j.mssp.2015.07.009.

[34] X. Zhang *et al.*, "Simulation of In 0.65 Ga 0.35 N single-junction solar cell," *J. Phys. Appl. Phys.*, vol. 40, no. 23, pp. 7335–7338, Dec. 2007, doi: 10.1088/0022-3727/40/23/013.

[35] P. K. Ghosh *et al.*, "Investigation of the Structural and Optical Properties of Compositionally V-Graded Strained In $_x$ Ga $_{1-x}$ N Layers," *Phys. Status Solidi B*, vol. 257, no. 4, p. 1900591, Apr. 2020, doi: 10.1002/pssb.201900591.

CHAPTER 6

Modeling of Λ-graded In(x)Ga(1-x)N solar cells; comparison of strained and relaxed feature

Authors: Mirsaeid. Sarollahi, Mohammad Zamani Alavijeh, Manal A. Aldawsari, Rohith Allaparthi, Reem Alhelais, , Malak A. Refaei, Md Helal Uddin Maruf , Morgan E. Ware

6.1 Abstract

The optical properties of Λ graded InGaN solar cells are studied. Graded InGaN well structures with the indium composition increasing to x_{max} then decreasing in a Λ shaped pattern have been designed. Through polarization doping, this naturally creates alternating p-type and n-type regions. Separate structures are designed by varying the indium alloy profile from GaN to maximum indium concentrations ranging from 20% to 90%, while maintaining a constant overall structure thicknesses of 100 nm. The solar cell parameters under fully strained and relaxed conditions are considered. The results show that a maximum efficiency of $\cong 5.5\%$, under fully strained condition occurs for x_{max}=60%. Solar cell efficiency under relaxed conditions increases to a maximum of 8.3% for x_{max}=90%. While Vegard's law predicts the bandgap under relaxed conditions, a Vegard-like law is empirically determined from the output of Nextnano for varying In compositions in order to calculate solar cell parameters under strain. Ternary alloys of Group III-N materials are great candidates to be used in photovoltaic devices. This is due to interesting properties such as high thermal conductivity, high optical absorption, and high radiation resistance [1]–[4]. In addition, the direct band gap, which is tunable over most of the usable solar spectrum [5],[6] makes them an appropriate choice for photovoltaic devices [7]–[9]. Several simulation studies for InGaN homojunctions have been reported. The solar efficiency, η, of a single junction $In_{0.65}Ga_{0.35}N$ solar cell was reported to be 20.28% [10], for example. However,

a higher efficiency of η =24.95% was demonstrated using the same indium composition due to adoption of the density of states (DOS) model [11]. This presented much more information about recombination/generation in the solar cell than the lifetime model by neglecting defects. Additionally, similar work for single-junction In0.622Ga0.378N demonstrated an efficiency of, η=26.5%, when the optical properties and physical models such as the Fermi-Dirac statistics, Auger and Shockley-Read-Hall recombination's, and the doping and temperature-dependent mobility model were taken into account in the simulations [12]. In another example[9],[11]–[13] InGaN homojunction solar cells were shown to have parameters for the short circuit current, open circuit voltage, fill factor, and efficiency equal to ~31.8 mA/cm2, ~0.874 V, ~0.775, and 21.5%, respectively, which were determined after varying the thicknesses of the junctions[13]. Growing p-type doped InGaN alloys are still considered challenging and problematic [14]–[17], therefore polarization doping plays an important role in the designed Λ shape graded structure. This grading of the film in group III-nitride materials can achieve very high levels of doping, without using additional impurities in the lattice [18]. This can be understood as follows. InN and GaN contain different spontaneous crystal polarizations (P). When a graded structure is grown, polarization doping is introduced correlating to the spatial rate of composition change by $-\nabla.P = \rho$. When the indium composition is increasing from GaN to InGaN, the background charges are negative ($\rho < 0$) which attract positive charges (holes) to make p-type doping. On the hand, when indium composition is decreasing from InGaN to GaN, the background doping charges are positive ($\rho > 0$) which attract negative charges (electrons) to make n-type doping [19]. In contrast, other reports show that AlGaN polarization doping due to graded films are reversed in comparison with InGaN. That is, by increasing the aluminum composition from GaN to AlGaN background charges are positive which create n-type doping due to attracting

electrons, and vice versa[20]. These polarization effects include both spontaneous and piezoelectric polarizations in III-V nitride heterostructures [21]. Additionally, growing a thick layer of $In_xGa_{1-x}N$ with a fixed indium composition is challenging due to a build up of strain and subsequent dislocation generation. Others have shown that InGaN alloys over the entire composition range can be grown when the layer is located within an InGaN/GaN double heterostructure without phase separation[22]–[24]. In this case, another advantage of using graded structures is that highly strained regions with high indium content can be obtained with reduced dislocations and phase separation[25],[26] whereas growing a thick high quality layer with a fixed indium composition would be challenging due to relaxation.

In this work, we present the simulation of a Λ-shaped graded structure. This is comprised of a double graded structure of $In_xGa_{1-x}N$ in which the indium composition starts to increase linearly from GaN to x_{max}, then linearly decrease from x_{max} to GaN. As explained above, this results in a p-n junction. The whole thickness of the structure is 100 nm (chosen to compare with previously published data) [27],[28], and x_{max} varies in different structures from 20% to 90%. The indium composition, strain relaxed energy band diagram, and fully strained energy band diagram versus position for x_{max}=50% are shown in Fig. 1 a, b & c respectively. According to Fig.1b and c, it is clear that the Λ graded structure creates p n junction. The first layer (0 – 50 nm) creates p-type (GaN to InGaN) and the second layer (50-100 nm) creates n-type (InGaN to GaN). (-10 to 0 and 100 to 110) are defined as ideal ohmic contact layers and are artifacts of the simulation. We consider no absorption or loss within these layers.
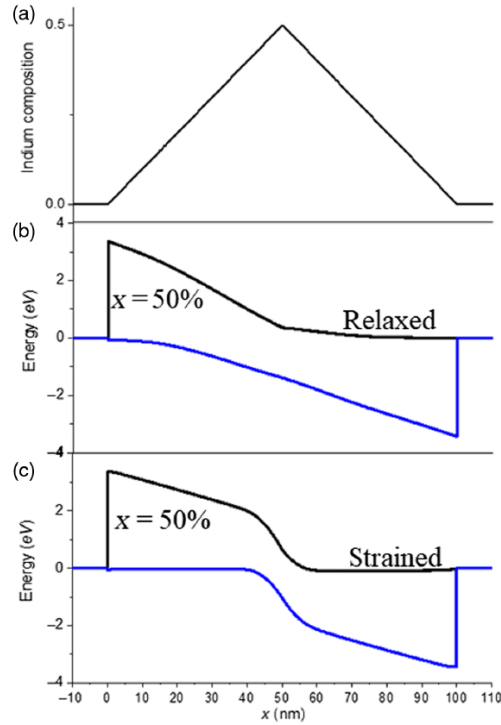
Figure 6. 1. a) Indium composition vs position, b) Energy band diagram vs position (fully relaxed), c) Energy band diagram vs position (fully strained) for Λ graded structure at x_{max}=50%

6.2 Simulation

Nextnano software, which has two varieties, nextnano3 and nextnano+ with slightly different specialities, was used to simulate the solar cell parameters. The software is able to calculate the generation rate for a constant alloy only. So, our graded structure is approximated as a step graded structure. Then, the generation rate of each layer is calculated in nextnano3. These are compiled manually into the generation rate versus position for the whole graded structure and subsequently imported in nextnano+ to calculate the light IV curve, incorporating the entire continuous graded film. This is then used for calculating solar cell parameters such as short circuit current, open circuit voltage, fill factor and efficiency for each structure.

The Λ-graded structure is defined by a d nm layer from GaN to $In_{x_{max}}Ga_{1-x_{max}}N$ followed by another d nm layer grading back to GaN. The total thickness of the designed

structure is then *2d*. To obtain the generation rate for the graded structure we need a method to

convert it to some set of constant alloy layers. A simple formula is created for this. A step size

provides the thickness of each constant composition layer, such that the Indium composition at

each position increases by:

$$\frac{x_{max}}{d - (step\ size)}$$ Equation 6. 1

We used a step size 1 nm (50 layers on each side of the maximum for a total of 100 layers

for our step graded structure). This step graded approximation of our structure is shown

schematically in Fig. 2.
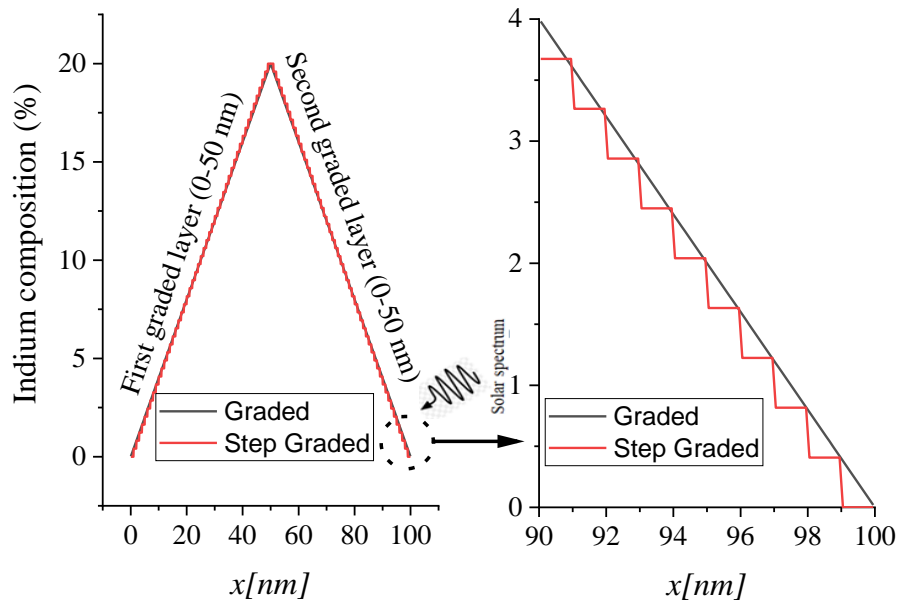
Figure 6. 2.a) Converting graded structure to step graded by equation 1 to calculate generation rate in nextnano. Receptivity of layers is given by the number below each layer between (90-100 nm) when light passing through the structure. Layers numbers are written next to each layer. b) Zoom in for 90-100 nm to show converting graded to step graded.

The generation rate for each layer in the step graded structure should be calculated in

order to find the generation rate for the whole structure. To find the generation rate in each layer,

the absorption coefficient and the light intensity should get imported into nextnano3. The solar

spectrum with intensity, I_0, first enters the structure through layer 100 (1 nm GaN), then the imported I_0 along with the GaN absorption coefficient (α) are used by nextnano3 to calculate the generation rate within this layer, for the first nm of penetration. The light intensity decreases as it passes through the layers. For layer 99, $I_{100} = I_0 \exp(-\alpha_{100}d)$, where d is the thickness of layer 100 and α_{100} is the absorption coefficient of that layer. By continuing this method for all given layers, the generation rate versus position is obtained as G_1(0-1), G_2(1-2),… G_{98}(97-98), G_{99}(98-99), G_{100}(99-100). Then, G vs position is imported into nextnano+ in order to determine the illuminated *I-V* curve for the solar cells. Other solar cell parameters can then be extracted from the light *I-V* curve.

6.3 Effects of strain on optical properties

There is a large lattice mismatch of 11% between InN and GaN. Due to this, strain is created for layers that are grown on a GaN substrate and can impact a device in different ways. First, the position of the valence and conduction band edges change, which reshapes the potential well along with the confinement of electrons and holes in the active region. The strain also changes the effective mass of carriers and the density of states (DOS) [29]–[33]. At the same time, general parameters which are derived from the bandgap, like the absorption coefficient are modified. So a detailed understanding of the strain is an important parameter for design, development and study of electronic and optical properties of semiconductor heterostructures based devices [34]. However, strict depth profiling of the strain in a bulk film, in which the strain is in general changing with each atomic layer (grading) is complicated. Therefore, in this paper we calculate the extreme cases, which are, a) the entire film is strained to the GaN substrate, and b) each layer is independently relaxed. We understand that for thicker films with higher compositions, neither of these cases is realistically possible within an as grown structure,

105

but we present them here as possible limits of this system. Nextnano software considers strain and, both piezoelectric polarization and spontaneous polarization [35]. Here, we assume InGaN to be strained to a GaN substrate. For modeling the absorption coefficient of InGaN as the alloy varies linearly, the bandgap under strain is required. In the absence of strain (fully relaxed) the $In_xGa_{1-x}N$ bandgap is calculated using Vegard's law which is defined in equation (3):

$$E_g(In_xGa_{1-x}N) = E_g(InN)x + E_g(GaN)(1-x) - b(x)(1-x) \quad \text{Equation 6. 2}$$

Large incosistencies are reported in literature for the bowing parameter, *b*, in the range of 1.4 to 3 eV which is generally thought to be the result of unaccounted for strain states in the $In_xGa_{1-x}N$ layers studied[36]–[42]. Additionally, there is some debate about whether the bowing coefficient parameter is compositionally dependent[43],[44] or not[12],[13],[45]. We derive our values from the nextnano materials database as a good overal average[46]–[48]. We acknowledge that there exist results indicating that other bowing parameters may be possible, but will use this one in order to learn the general response of the system. Any result which is dependent on bowing is by its nature a second order effect and should only minimally affect the present results.

The values for the bandgap energies under strain and relaxed as functions of composition, *x*, were determined using nextnano. The output was fit to a second order polynomial in *x*, similar to Vegard's law in order to achieve an analytic representation for this quantity[49]. Both are shown Eq. 4 based on Fig. 3.
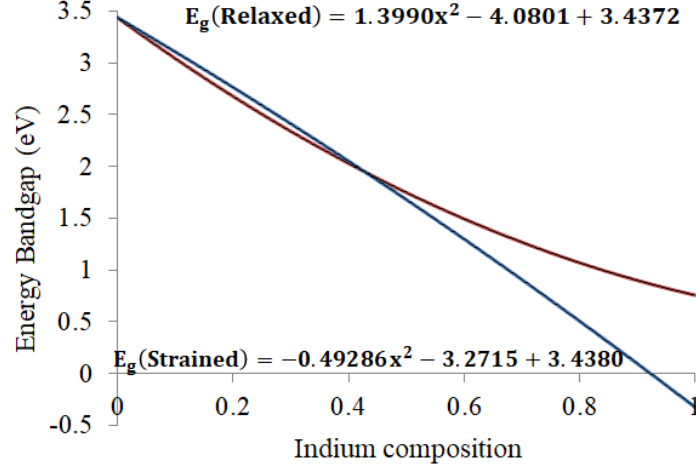
Figure 6. 3. Energy bandgap Vs Indium Composition under relaxed (Red line) and strained (Blue line)

$$E_g(x)(Strain) = -0.49286x^2 - 3.27153x + 3.43805 \qquad \text{Equation 6. 3}$$

	$E_g(x)(No\ strain) = 1.3990x^2 - 4.0801x + 3.4372$	Equation 6. 4

According to equation 3, the bandgap for strained $In_xGa_{1-x}N$ with $x > {\sim}90\%$ is negative[49], implying that InGaN is a semi-metal in this range[50]–[51]. In this work, we do not further discuss this subject, but materials with negative bandgap potentially present novel research directions. Here, all simulations are performed up to 90%. For the relaxed material, however, there is no problem with the bandgap becoming negative and in fact relaxed devices with $x_{max} > 90\%$ have been simulated and will be reported on separately as they demonstrate separate and interesting anomalous response. The absorption coefficient for InGaN ternary alloys can be parameterized as follows [52]–[54]:

$$\alpha(\lambda) = \alpha_0 \sqrt{a(x)(E - E_g) + b(x)(E - E_g)^2} \qquad \text{Equation 6. 5}$$

with E the photon energy, E_g the bandgap, and $\alpha_0 = 10^5\ cm^{-1}$. In addition, $a(x)$ and $b(x)$ are dimensionless parameters which are obtained by fitting over the entire composition range [52]–[54].

$$a(x) = 12.87x^4 - 37.79x^3 + 40.43x^2 - 18.35x + 3.52 \qquad \text{Equation 6. 6}$$

$$b(x) = -2.92x^2 + 4.05x - 0.66 \qquad \text{Equation 6. 7}$$

As a result, the absorption coefficients as functions of bandgap can be calculated empirically over the entire range of alloys. Once this calculation has been perform Eq.5 can be converted to functions of the bandgap energies under strain by plotting and fitting the parameters, a and b, as functions of the strained band gap energy, $a(E_{g(Strain)})$ and $b(E_{g(Strain)})$. These are shown in Eqs. 8 and 9 and Fig. 4.
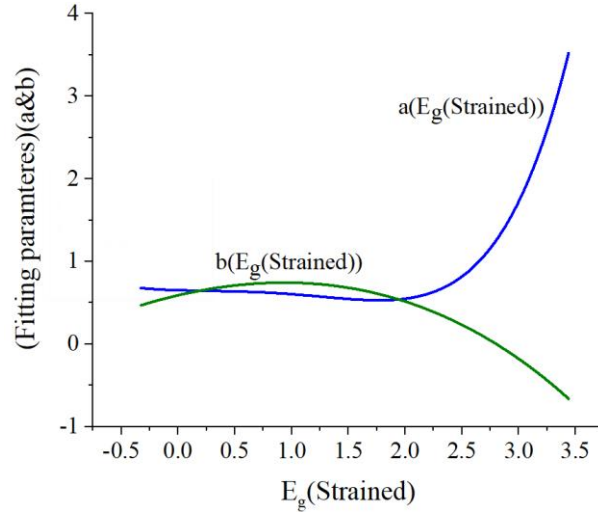
Figure 6. 4. Fitting parameters (a & b) Vs Energy bandgap under strained

$$a(E_{g(Strained)}) = \qquad \text{Equation 6. 8}$$
$$1.2550 \cdot 10^{-2} E_{g(s)}{}^5 - 8.3347 \cdot 10^{-3} E_{g(s)}{}^4 - 5.8864e.\,10^{-2} E_{g(s)}{}^3$$
$$- 4.5488.\,10^{-2} E_{g(s)}{}^2 - 4.1689.\,10^{-2} E_{g(s)} + 0.65425$$

$b(E_{g(Strained)}) =$	Equation 6. 9
$-1.5280.\,10^{-3} E_{g(s)}{}^4 - 5.5727.\,10^{-3} E_{g(s)}{}^3 - 1.6201.\,10^{-1} E_{g(s)}{}^2$ $+ 3.2084.\,10^{-1} E_{g(s)} + 0.59135$	

The absorption coefficients as functions of wavelength, $\alpha(\lambda)$, can then be calculated under strain, using the strained values for the bandgaps. Then, using Eqs. 4 through 9, we have both the bandgap energies as well as the absorption coefficients as functions of the bandgap energies for both strained and unstrained conditions. Finally, the generation rate for each layer

can be calculated after importing the absorption coefficient and light intensity relating to each layer. Here, the original absorption data upon which absorption constants are modeled from are obtained from experiments in Ref. [54] covering the natural relaxed alloys of InN and GaN. Therefore, the bandgap parameter only covers that range with a minimum of 0.7 eV for InN. Therefore, we limit our discussion of the strained material only to bandgaps within that range, i.e., $x \leq 0.9$ (strained). The generation rates for the strained condition are shown in Fig. 5. As discussed above, the generation for each nm was calculated, and then the generation for the whole structure as a function of position is compiled for both strained and relaxed.
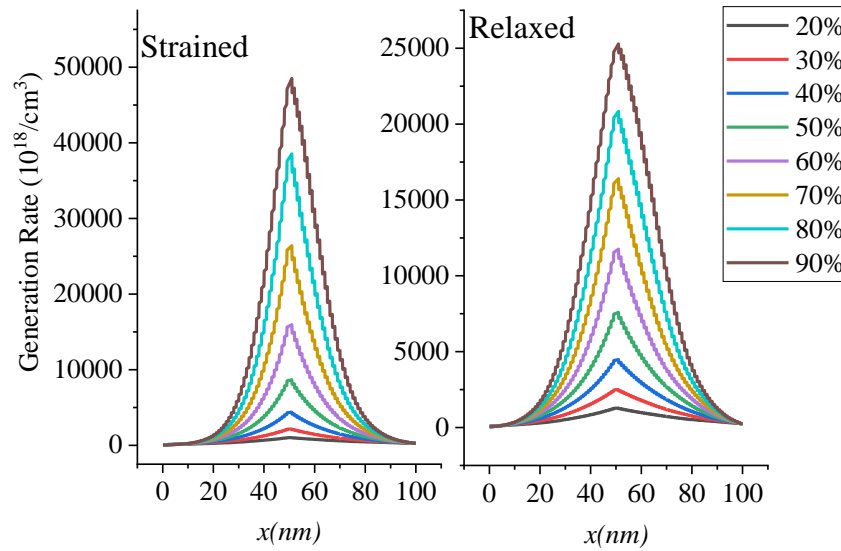
Figure 6. 5. Generation rate for Λ shape graded structure under a) strained b) Relaxed condition

6.4 Solar cell parameters

In order to calculate the *J-V* characterization, $AM_{1.5G}$ is used as the total irradiance on the solar cell, which supplies $100 \frac{mW}{cm^2}$ of power to the solar cell. The *J-V* plots for the fully strained and relaxed graded structures are shown in Fig5 a) and b), respectively.
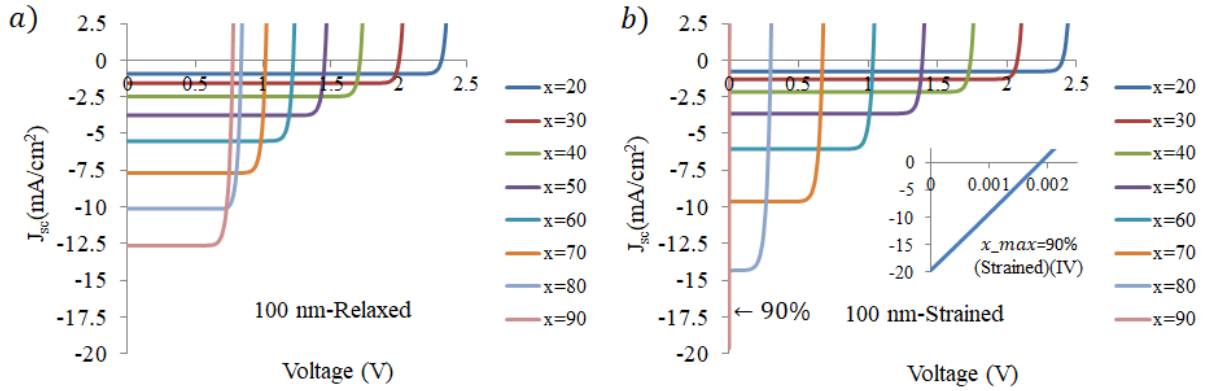
Figure 6. 6. Light J-V curve under a) fully relaxed and b) strained condition for different x_{max}. Insert is J-V curve for x_{max}=90% under strained.

According to literature for single composition growth, for x<25% the InGaN structure should be fully strained[28] to the GaN lattice constant, however the graded films have yet to be studied to realize the critical thickness for relaxation, which may be much higher. According to Fig.7, the V_{oc} effectively follows the bandgap with x_{max} as is also shown for different graded structures previously [28],[49].
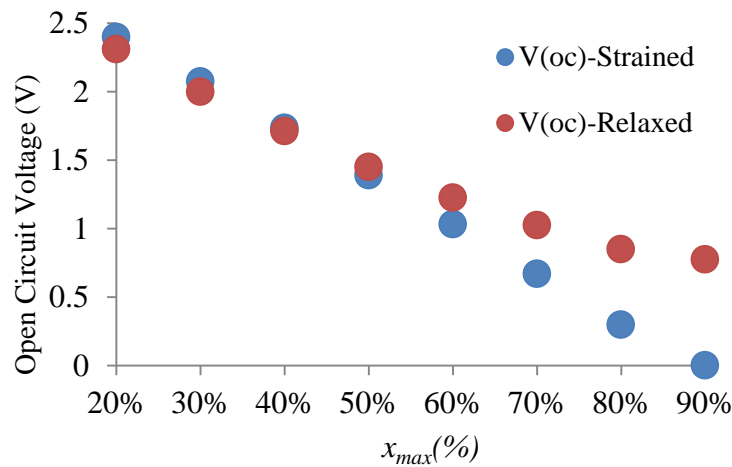
Figure 6. 7. Open circuit voltage for strained and relaxed condition in different x_{max}

By increasing x_{max}, the V_{oc} decreases due to the overall decrease in bandgap (for both strained and relaxed conditions). The short circuit current, I_{sc}, exhibits a reverse dependency,

where increasing the maximum indium composition, i.e., decreasing the bandgap, results in an increase in I_{sc}. This is shown in Fig.8 and generally expected [55].
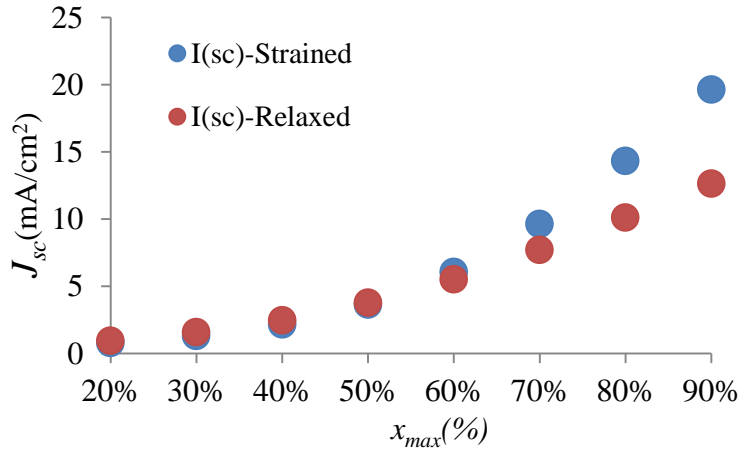
Figure 6. 8. Short circuit current for strained and relaxed conditions

Generally, this is the expected outcome. The minimum bandgap energy of the graded InGaN decreases by increasing the maximum indium composition. The open circuit voltage is directly correlated to energy bandgap. In other words, the V_{oc} is determined by the difference of the Fermi energies (ΔE_F) of the electron and the hole in the depletion region, which in turn is affected by the bandgap energy [56]. Ideally, the highest value available for V_{oc} in a given material is governed by the bandgap energy, with lower values determined by recombination processes [55], [57]. In contrast, the short circuit current density, J_{sc}, increases with decreasing bandgap[55], resulting from an increase in absorption and the associated generation rate in high-indium-composition InGaN solar cells[13]. Low short circuit current density, J_{sc}, due to weak absorption over the entire solar spectrum in low indium composition InGaN solar cells is the main reason for low solar efficiency in these structures. As the indium composition increases, J_{sc} increases and V_{oc} decreases, which generally leads to higher efficiency, however there are limitations as will be shown below. The fill factor (FF) is defined as the ratio between the maximum power ($P_{max} = J_m V_m$) created by the solar cell and the product, $V_{oc}J_{sc}$, as follows.

$$Fill\ Factor = \frac{J_m * V_m}{J_{sc} * V_{oc}}$$
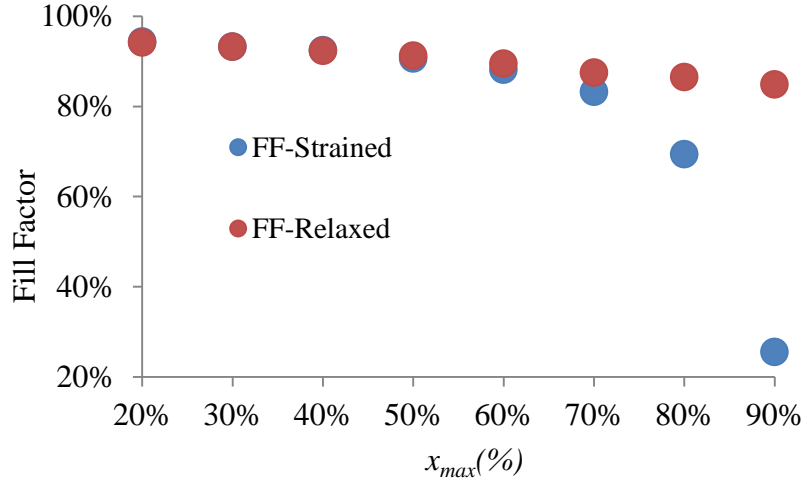
Figure 6. 9. Fill Factor for strained and relaxed conditions

According to Fig.9, FF decreases as the indium composition increases. The fill factor is ~94% for x_{max}=20% and decreases at higher x_{max}, with a minimum value of ~26% at x_{max}=90% under strain. The minimum value is ~85% at x_{max}=90% under fully relaxed conditions. Here, the relaxed material demonstrates more stability with increasing composition than the strained material does. Finally, the solar efficiency is reported. The solar efficiency is defined as the part of the sunlight energy that gets converted to electricity by the solar cell and is calculated by:

$$Efficiency(\%) = \frac{P_{max}}{P_{in}} = \frac{P_{max}}{100}, \ P_{max} = FF.V_{OC}J_{SC}$$

The solar efficiencies for the designed structures under fully strained and relaxed conditions are displayed for different maximum compositions in Fig.10.
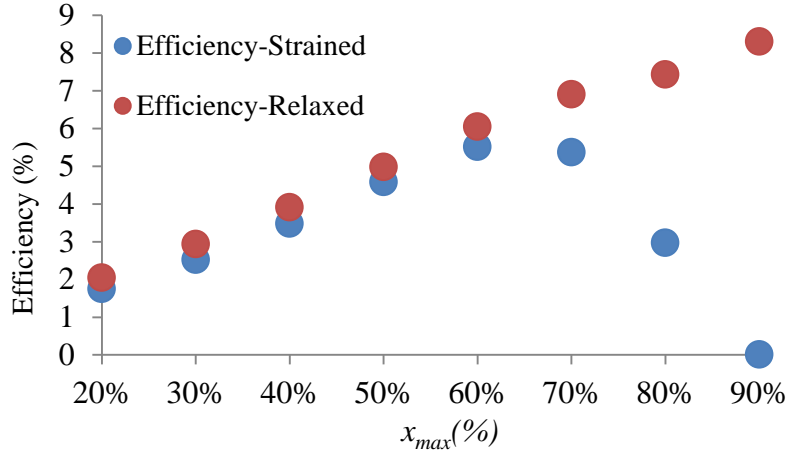
Figure 6. 10.Solar efficiency for strained and relaxed conditions

The solar efficiency for strained InGaN shows a maximum value at x_{max}=60% which is 5.5%. This is lower than other reports due mainly to the much thinner structure[10], however the resulting composition of the maximum is similar to published single composition results[10],[13]. The minimum efficiency at x_{max}=90% is less than 0.1% (strained InGaN) and ~2% at 20% (Relaxed InGaN). However, the solar efficiency of relaxed InGaN is ~ 8.3% for x_{max}= 90%, and would likely increase with further increase in x_{max}. The sudden drop in efficiency as the In composition increases past ~60% in the strained InGaN is the result of the sudden drop in the fill factor at the same composition. As we can see from Eq. 10, the FF is inversely proportional to the product of J_{sc} and V_{oc}. And, if we look at Figs. 7 and 8, we can see that the V_{oc} of the strained material is roughly half that of the relaxed material, while the J_{sc} of the strained material is only about 10% more than the relaxed material. So, as a product, $J_{sc}V_{oc}$ should decrease for the strained material relative to the relaxed material. However, we can see, again from Fig. 7 that the V_{oc} for the strained material quickly goes to zero, and since the V_m is bounded by the V_{oc}, it must go to zero faster than V_{oc}, so the fraction that is the FF rapidly vanishes as the composition increases beyond 60% for the strained material. Now, we must ask

ourselves why the V_{oc} of the strained material goes to zero at high In compositions, and the simple answer is that the bandgap in our model goes to zero due to the strain as can be seen in Fig. 3. The performance of solar cell out of atmosphere was studies by using AM0. The solar cell parameters were calculated under AM0 ($135.3 mW/cm^2$) for both strained and relaxed. The data show the same trend as domestic calculation. For strain, the maximum efficiency occurs at 60%. For relax, like previous reported results for AM1.5G, the efficiency increasing by increasing Indium composition. In other words, x_{max}=90% showed the maximum efficiency. Fig. 11a) shows Standard Solar Spectra for space (AM0) and domestic (AM1.5G) use, Fig. 11b) Efficiency for strained and relaxed conditions for space using (AM0). According to Fig. 11a, the intensity of AM0 is higher than AM1.5G. The maximum efficiency for both strained and relaxed conditions at AM0 is almost the same as AM1.5G.
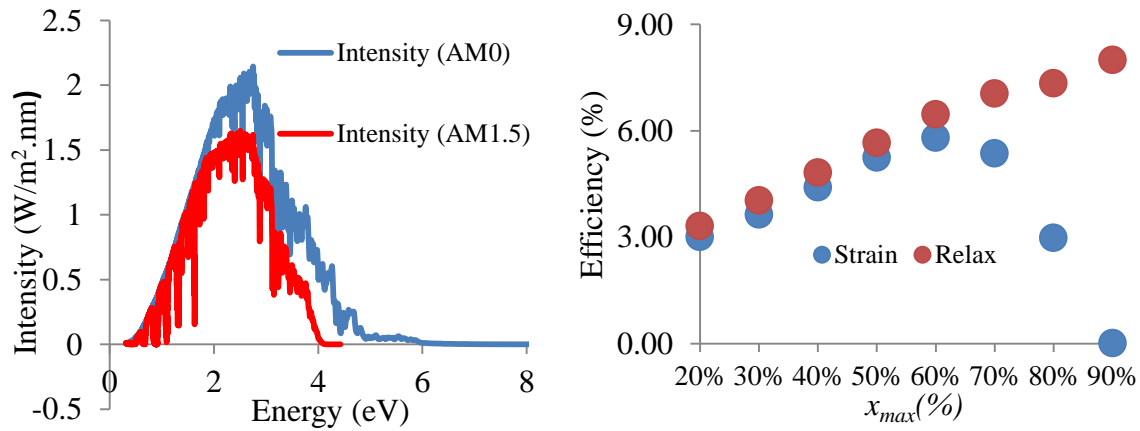
Figure 6. 11. a) Standard Solar Spectra for space (AM0) and domestic (AM1.5G), b) Solar efficiency for strained and relaxed conditions under AM0

In order to investigate the effect of thickness on solar cell parameters at x_{max}=60% for the strained condition, 200 and 300 nm, Λ-shaped graded structures, which are defined similarly symmetric as the above structures, are studied and compared with the 100 nm structure. The *J-V* curves for the different thicknesses at x_{max}=60% is displayed in Fig.12.
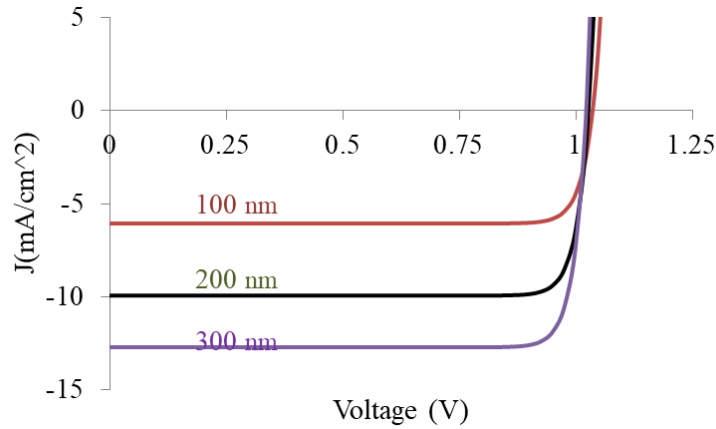
Figure 6. 12. J-V curve for different thicknesses at *x*=60% for strained condition

As the solar cell thickness increases, the short circuit current increases sharply. On the other hand, the open circuit voltage decreases slowly. The solar cell parameters for different thicknesses are shown in Fig.13. With this increase in thickness, we see the following. According to Fig.13a, the I_{sc} increases from $6.98\ mA/cm^2$ to $15\ mA/cm^2$. Fig.13b indicates V_{oc} decreases slowly from 1.04 V to 1.026 V. Fig.13c shows the fill factor increasing from 88.12% to ~88.45%, while the overall efficiency almost doubles from 6% to 12% in Fig.13d.
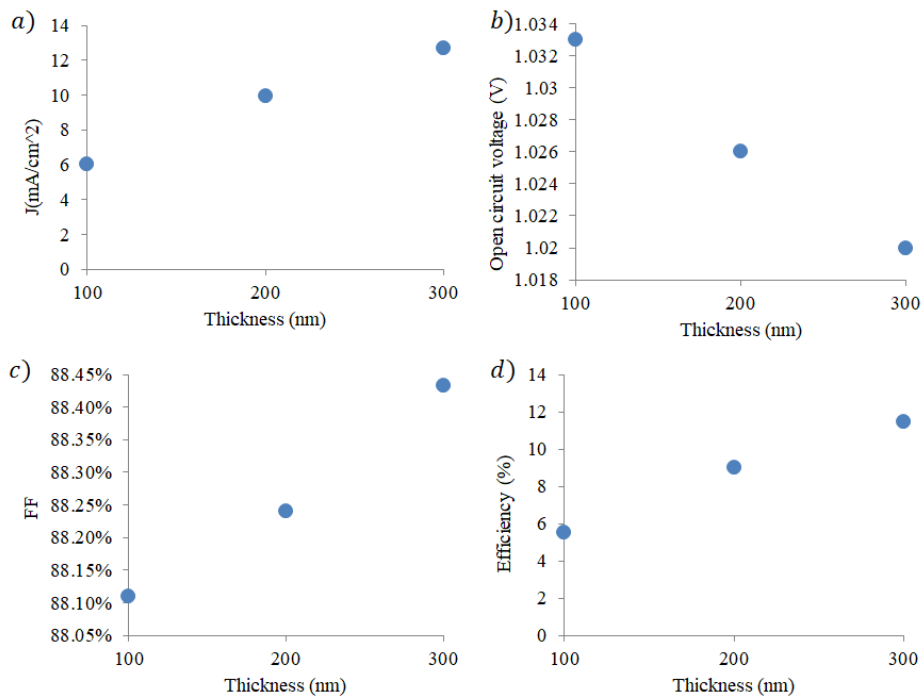
Figure 6. 13. a) Short circuit current, b) Open circuit voltage, c) Efficiency (%), d) Fill Factor in different thicknesses

6.5 Conclusion

InGaN graded structures, where the In composition varied in a Λ-shape over only 100 nm were designed and investigated through simulation to determine their potential for use as thin film solar cell devices. The main advantage of this structure is to form p- and n- type layers due to polarization doping as p-type doping in group III-nitride materials isn't efficient. In addition, a new model (a Vegard's law-like equation) was presented to calculate the energy bandgap for InGaN strained to a GaN substrate and similarly to calculate the absorption coefficient for an arbitrary value of the InGaN bandgap. Solar cell parameters were studied for Λ-shaped structures for both strained and relaxed conditions. The maximum efficiency was found to be ~5.5% with a maximum In composition of x_{max}=60% under fully strained conditions. However, for fully relaxed material, the maximum efficiency was found to be ~8.5% for x_{max}=90%, with an indication that further increase in composition would increase efficiency further. Finally, the efficiency for strained Λ-shaped structures with the total thickness increased to 300 nm and x_{max}=60% increased by nearly a factor of two. These results indicate a useful window for InGaN Λ-graded devices to be used for solar cells. The polarization doping provides the highly doped contact regions without the addition of lifetime killing impurities, while the compositional grading naturally allows for higher In content and therefore stronger optical absorption without immediate relaxation due to lattice mismatch with GaN substrates. Ultimately, we believe that the operation of any real device based on these types of graded films will perform somehow between the maximally strained example here and the maximally relaxed one. Generally, either extreme is difficult to realize for any significant thickness or high concentration. So, the

presented simulations form "boundary conditions" to the prediction of the performance of these

structures as solar cell devices.

6.6 References

[1] B. Kucukgok et al., "The structural properties of InGaN alloys and the interdependence on the thermoelectric behavior," AIP Advances **6**(2), 025305 (2016) [doi:10.1063/1.4941934].

[2] S. Nakamura et al., "Superbright Green InGaN Single-Quantum-Well-Structure Light-Emitting Diodes," Jpn. J. Appl. Phys. **34**(Part 2, No. 10B), L1332–L1335 (1995) [doi:10.1143/JJAP.34.L1332].

[3] S. Nakamura et al., "InGaN-Based Multi-Quantum-Well-Structure Laser Diodes," Jpn. J. Appl. Phys. **35**(Part 2, No. 1B), L74–L76 (1996) [doi:10.1143/JJAP.35.L74].

[4] G. Pozina et al., "Origin of multiple peak photoluminescence in InGaN/GaN multiple quantum wells," Journal of Applied Physics **88**(5), 2677–2681 (2000) [doi:10.1063/1.1287124].

[5] A. G. Bhuiyan et al., "InGaN Solar Cells: Present State of the Art and Important Challenges," IEEE J. Photovoltaics **2**(3), 276–293 (2012) [doi:10.1109/JPHOTOV.2012.2193384].

[6] A. David and M. J. Grundmann, "Influence of polarization fields on carrier lifetime and recombination rates in InGaN-based light-emitting diodes," Appl. Phys. Lett. **97**(3), 033501 (2010) [doi:10.1063/1.3462916].

[7] R. Cheriton et al., "Two-photon photocurrent in InGaN/GaN nanowire intermediate band solar cells," Commun Mater **1**(1), 63 (2020) [doi:10.1038/s43246-020-00054-6].

[8] S. R. Routray and T. R. Lenka, "InGaN-based solar cells: a wide solar spectrum harvesting technology for twenty-first century," CSIT **6**(1), 83–96 (2018) [doi:10.1007/s40012-017-0181-9].

[9] Y. Sayad and A. Nouiri, "Simulation Study of InGaN / GaN Multiple Quantum Well Solar Cells," JNTM **4**(1), 9–10 (2014) [doi:10.12816/0010288].

[10] X. Zhang et al., "Simulation of In$_{0.65}$Ga$_{0.35}$N single-junction solar cell," J. Phys. D: Appl. Phys. **40**(23), 7335–7338 (2007) [doi:10.1088/0022-3727/40/23/013].

[11] X. Shen et al., "Simulation of the InGaN-based tandem solar cells," presented at Solar Energy + Applications, 28 August 2008, San Diego, CA, 70450E [doi:10.1117/12.793997].

[12] A. Mesrane et al., "Design and Simulation of InGaN p - n Junction Solar Cell," International Journal of Photoenergy **2015**, 1–9 (2015) [doi:10.1155/2015/594858].

[13] S.-W. Feng et al., "Modeling of InGaN p-n junction solar cells," Opt. Mater. Express **3**(10), 1777 (2013) [doi:10.1364/OME.3.001777].

[14] C. G. Van de Walle and D. Segev, "Microscopic origins of surface states on nitride surfaces," Journal of Applied Physics **101**(8), 081704 (2007) [doi:10.1063/1.2722731].

[15] S. Brochen et al., "Dependence of the Mg-related acceptor ionization energy with the acceptor concentration in p-type GaN layers grown by molecular beam epitaxy," Appl. Phys. Lett. **103**(3), 032102 (2013) [doi:10.1063/1.4813598].

[16] T. Narita et al., "Progress on and challenges of p-type formation for GaN power devices," Journal of Applied Physics **128**(9), 090901 (2020) [doi:10.1063/5.0022198].

[17] H. Obloh et al., "Self-compensation in Mg doped p-type GaN grown by MOCVD," Journal of Crystal Growth **195**(1–4), 270–273 (1998) [doi:10.1016/S0022-0248(98)00578-8].

[18] F. K. LeGoues et al., "Mechanism and conditions for anomalous strain relaxation in graded thin films and superlattices," Journal of Applied Physics **71**(9), 4230–4243 (1992) [doi:10.1063/1.350803].

[19] Y.-J. Lee, Y.-C. Yao, and Z.-P. Yang, "Numerical Analysis on Polarization-Induced Doping III-Nitride n-i-p Solar Cells," IEEE Photonics J. **7**(1), 1–9 (2015) [doi:10.1109/JPHOT.2015.2392374].

[20] S. Li et al., "Polarization induced pn-junction without dopant in graded AlGaN coherently strained on GaN," Appl. Phys. Lett. **101**(12), 122103 (2012) [doi:10.1063/1.4753993].

[21] D. Jena et al., "Polarization-engineering in group III-nitride heterostructures: New opportunities for device design: Polarization engineering in III-V nitride heterostructures," Phys. Status Solidi A **208**(7), 1511–1516 (2011) [doi:10.1002/pssa.201001189].

[22] R. Dahal et al., "InGaN/GaN multiple quantum well solar cells with long operating wavelengths," Applied Physics Letters **94**(6), 063505 (2009) [doi:10.1063/1.3081123].

[23] R. Singh et al., "Phase separation in InGaN thick films and formation of InGaN/GaN double heterostructures in the entire alloy composition," Applied Physics Letters **70**(9), 1089–1091 (1997) [doi:10.1063/1.118493].

[24] A. Tabata et al., "Phase separation suppression in InGaN epitaxial layers due to biaxial strain," Applied Physics Letters **80**(5), 769–771 (2002) [doi:10.1063/1.1436270].

[25] N. Miller et al., "Low-temperature grown compositionally graded InGaN films," phys. stat. sol. (c) **5**(6), 1866–1869 (2008) [doi:10.1002/pssc.200778719].

[26] Md. A. Hossain et al., "Dislocation reduction in heteroepitaxial In x Ga1-xN using step-graded interlayer for future solar cells," Mater Renew Sustain Energy **3**(1), 20 (2014) [doi:10.1007/s40243-013-0020-3].

[27] M. Sarollahi et al., "Luminescence Properties of GaN/InxGa1−xN/InyGa1−yN Double Graded Structures (Zigzag Quantum Wells)," Journal of Elec Materi **49**(6), 3512–3519 (2020) [doi:10.1007/s11664-020-08033-w].

[28] P. K. Ghosh et al., "Investigation of the Structural and Optical Properties of Compositionally V-Graded Strained In $_x$ Ga $_{1-x}$ N Layers," Phys. Status Solidi B **257**(4), 1900591 (2020) [doi:10.1002/pssb.201900591].

[29] A. E. Romanov et al., "Strain-induced polarization in wurtzite III-nitride semipolar layers," Journal of Applied Physics **100**(2), 023522 (2006) [doi:10.1063/1.2218385].

[30] H. Masui et al., "Optical polarization characteristics of *m* -oriented InGaN/GaN light-emitting diodes with various indium compositions in single-quantum-well structure," J. Phys. D: Appl. Phys. **41**(22), 225104 (2008) [doi:10.1088/0022-3727/41/22/225104].

[31] S.-H. Park and S.-L. Chuang, "Crystal-orientation effects on the piezoelectric field and electronic properties of strained wurtzite semiconductors," Phys. Rev. B **59**(7), 4725–4737 (1999) [doi:10.1103/PhysRevB.59.4725].

[32] M. Azize and T. Palacios, "Effect of substrate-induced strain in the transport properties of AlGaN/GaN heterostructures," Journal of Applied Physics **108**(2), 023707 (2010) [doi:10.1063/1.3463150].

[33] C. E. Dreyer, A. Janotti, and C. G. Van de Walle, "Effects of strain on the electron effective mass in GaN and AlN," Appl. Phys. Lett. **102**(14), 142105 (2013) [doi:10.1063/1.4801520].

[34] S. Birner et al., "Modeling of Semiconductor Nanostructures with nextnano [3]," Acta Phys. Pol. A **110**(2), 111–124 (2006) [doi:10.12693/APhysPolA.110.111].

[35] "strain," <https://www.nextnano.de/nextnanoplus/software_documentation/input_file/strain.htm> (accessed 9 October 2021).

[36] S. N. Alam et al., "Bandgap and refractive index estimates of InAlN and related nitrides across their full composition ranges," Sci Rep **10**(1), 16205 (2020) [doi:10.1038/s41598-020-73160-7].

[37] P. G. Moses and C. G. Van de Walle, "Band bowing and band alignment in InGaN alloys," Appl. Phys. Lett. **96**(2), 021908 (2010) [doi:10.1063/1.3291055].

[38] M. Kurouchi et al., "Growth and properties of In-rich InGaN films grown on (0001) sapphire by RF-MBE," phys. stat. sol. (b) **241**(12), 2843–2848 (2004) [doi:10.1002/pssb.200405121].

[39] M. D. McCluskey et al., "Large band gap bowing of InxGa1−xN alloys," Appl. Phys. Lett. **72**(21), 2725–2726 (1998) [doi:10.1063/1.121072].

[40] T. Aschenbrenner et al., "Optical and structural characterization of AlInN layers for optoelectronic applications," Journal of Applied Physics **108**(6), 063533 (2010) [doi:10.1063/1.3467964].

[41] Y.-K. Kuo, W.-W. Lin, and J. Lin, "Band-Gap Bowing Parameter of the In $_x$ Ga $_{1-x}$ N Derived From Theoretical Simulation," Jpn. J. Appl. Phys. **40**(Part 1, No. 5A), 3157–3158 (2001) [doi:10.1143/JJAP.40.3157].

[42] M. Moret et al., "Optical, structural investigations and band-gap bowing parameter of GaInN alloys," Journal of Crystal Growth **311**(10), 2795–2797 (2009) [doi:10.1016/j.jcrysgro.2009.01.009].

[43] M. A. Caro, S. Schulz, and E. P. O'Reilly, "Theory of local electric polarization and its relation to internal strain: Impact on polarization potential and electronic properties of group-III nitrides," Phys. Rev. B **88**(21), 214103 (2013) [doi:10.1103/PhysRevB.88.214103].

[44] P. G. Moses et al., "Hybrid functional investigations of band gaps and band alignments for AlN, GaN, InN, and InGaN," The Journal of Chemical Physics **134**(8), 084703 (2011) [doi:10.1063/1.3548872].

[45] M. Nawaz and A. Ahmad, "A TCAD-based modeling of GaN/InGaN/Si solar cells," Semicond. Sci. Technol. **27**(3), 035019 (2012) [doi:10.1088/0268-1242/27/3/035019].

[46] I. Vurgaftman and J. R. Meyer, "Band parameters for nitrogen-containing semiconductors," Journal of Applied Physics **94**(6), 3675–3696 (2003) [doi:10.1063/1.1600519].

[47] I. Vurgaftman, J. R. Meyer, and L. R. Ram-Mohan, "Band parameters for III–V compound semiconductors and their alloys," Journal of Applied Physics **89**(11), 5815–5875 (2001) [doi:10.1063/1.1368156].

[48] J. Wu et al., "Small band gap bowing in In1−xGaxN alloys," Appl. Phys. Lett. **80**(25), 4741–4743 (2002) [doi:10.1063/1.1489481].

[49] M. Sarollahi et al., "Study of simulations of double graded InGaN solar cell structures," arXiv:2110.12864 [cond-mat, physics:physics] (2021).

[50] N. Malkova and G. W. Bryant, "Negative-band-gap quantum dots: Gap collapse, intrinsic surface states, excitonic response, and excitonic insulator phase," Phys. Rev. B **82**(15), 155314 (2010) [doi:10.1103/PhysRevB.82.155314].

[51] T. D. Veal, I. Mahboob, and C. F. McConville, "Negative Band Gaps in Dilute InN x Sb 1 − x Alloys," Phys. Rev. Lett. **92**(13), 136801 (2004) [doi:10.1103/PhysRevLett.92.136801].

[52] R. Belghouthi et al., "Modeling of polarization charge in N-face InGaN/GaN MQW solar cells," Materials Science in Semiconductor Processing **40**, 424–428 (2015) [doi:10.1016/j.mssp.2015.07.009].

[53] G. Giannoccaro, F. De Leonardis, and V. Passaro, "Modeling of the Interminiband Absorption Coefficient in InGaN Quantum Dot Superlattices," Photonics **3**(1), 5 (2016) [doi:10.3390/photonics3010005].

[54] J. Zhou et al., "Study on the self-absorption of InGaN quantum wells at high photon density," Appl. Opt. **59**(16), 4790 (2020) [doi:10.1364/AO.392940].

[55] M. A. Green, *Solar cells: operating principles, technology and system applications*, Repr. [der Ausg.] Englewood Cliffs, NJ 1982, Univ. of New South Wales, Kensington, NSW (1998).

[56] J. Nelson, *The Physics of Solar Cells*, PUBLISHED BY IMPERIAL COLLEGE PRESS AND DISTRIBUTED BY WORLD SCIENTIFIC PUBLISHING CO. (2003) [doi:10.1142/p276].

[57] J. C. Blakesley and D. Neher, "Relationship between energetic disorder and open-circuit voltage in bulk heterojunction organic solar cells," Phys. Rev. B **84**(7), 075210 (2011) [doi:10.1103/PhysRevB.84.075210].

CHAPTER 7

Summary and conclusion

7.1 Summary

This work investigates the optical properties of Λ shape graded structure experimentally and through simulation. Actual devices which were grown by molecular beam epitaxy (MBE) at 575 °C with a 400nm unintentionally doped GaN buffer grown at 800 °C, then a thin film which contained 88 nm double InGaN graded structure. The graded structure starts from $In_{3\%}Ga_{97\%}N$ and was graded linearly to $In_{x_{max}}Ga_{1-x_{max}}N$ over 44 nm, where x_{max} is the maximum indium composition. The next layer is 44 nm graded structure that indium composition is decreased from $In_{x_{max}}Ga_{1-x_{max}}N$ to $In_{3\%}Ga_{97\%}N$. Due to polarization doping, the first graded layer is p type (0-44 nm) , and second (reversed graded) layer is n type. Optical properties of two structures when x_{max}= 19.5% and 22.5% were studied with photoluminescence under HeCd laser illumination which the wavelength is 325 nm ($\sim$ UV range). Laser power is 10 mw in front of light source and the energy of laser is larger than thin film bandgap and GaN buffer layer. To obtain the basic understanding about the PL peak and recombination mechanism related to radiative transition corresponded to each peak, power dependence PL was studied.

As discussed in Chapter 2, the exponent of a power law describing the PL change with excitation intensity, α, describes the different recombination mechanisms. A table (2.2) is provided to summarize the power law for all peaks in the two samples. It indicates there are two peaks in each sample which are due to exciton-like transitions, with some free carrier character. The rest of the PL peaks are dominated by free-to-bound or bound-to-bound transitions.

Another study for these Λ-graded structures was performed to compare with nextnano simulation. The band to band low exciton power which is ground state hole wave-function along

with electron wave-functions were considered. Energy band diagram of graded structures (3 structures) when x_{max}= 19.5%, 22.5% and 26% were simulated by nextnano software. Energy band diagram plots confirmed the p type and n type layer due to polarization doping are provided by graded layers. In addition, electron and hole distribution verified that in the first 44 nm which predicted to be p type, hole distribution is high. Moreover, electron distribution is high in the second 44 nm. Intentional background doping was added to GaN Buffer layer $1.3*10^{17}$ cm^{-3} in order to closely match experiment. Reciprocal Space Mapping measurements showed fully strained for Sample A (19.5%) and Sample B (22.5%) and partially relaxed for Sample C (26%). In regard to position of wave-functions, we understood the luminescence due to band to band transitions occurs at the interface of n type GaN buffer layer and beginning of the first graded structure (which is p type) where the band offset was seen due to 3% alloy. This area formed a confined well for the holes. Transition probability among ground state hole and electron wave-functions were considered and calculated by nextnano. For electrons, a pseudo-continuum was considered to show available energy bands at the GaN/InGaN interface. Transition probability vs energy was used to predict the PL for each sample.

As we were capabled to predict PL for graded structure, the next study was to compare the predicted PL for graded structure when the number of layers were changed in periodic structures. Three samples were designed to study their predicted PL by nextnano. The samples had the same thickness (900 nm), containing a 500 nm GaN buffer layer (n type). Energy band diagrams showed p and n layers due to polarization doping. In addition, degenerate n type doping was seen for very rapid grades. Ground state electron and hole in each well were considered for all structures and the transition probability as a function of energy was considered as prediction of the PL. For sample A (1 period), two peaks were obtaind which peak at higher

enrgies was correlated to envelope of non-zero transition probability between ground state hole and all electrons, and peak at lower energy was due to envelope of non-zero transition probability between ground state electron and holes. For sample B, 2 peaks at lower energies were due to ground state electrons at each well and 2 peaks at higher energies were due to ground state hole at each well but due to convergency in electron peaks, 3 peaks were obvious. For sample C, 6 peaks were shown. Like two other samples, 3 peaks for electrons (lower energies) and 3 peaks for holes (higher energies). All electrons peaks energies were in similar energies. For holes the peaks due to well 2 and 3 had simialr enegies, while peaks at the highest energy was due to hole in first well.

Two last chapters consider the graded structures as solar cell devices. To compare the influence of graded structure on solar efficiency in comparison with well known structures, a 100 nm Flat Base Graded (FBG) structure which contains 20 nm (10 nm in each side) graded structure was designed to compare with 100 nm Square Well (SW) and 100 nm Homojunction (HMJ) structures. FBG starts from GaN to $In_{x_{max}}Ga_{1-x_{max}}N$ with variation of $x_{max} = 20\%$ to 70%. Then structure was followed with 80 nm of constant composition $In_{x_{max}}Ga_{1-x_{max}}N$, and then went back from $In_{x_{max}}Ga_{1-x_{max}}N$ to GaN. Due to polarization doping in graded InGaN layer, p and n layers were created at the edges of the device. For SW and HMJ structures, 10 nm in each side was intentionaly doped equal to polarization doping charge density in graded structure. All structres were p-i-n. The nextnano software was used to simulate the graded structure under fully strained to GaN lattice constant and fully relaxed. Nextnano gave an equation for strained and relaxed structure bandgap versus indium composition which was used to calculate absorption coeffiecint (which is the function of energy bandgap). Nextnano was able to calculate only generation rate for a fixed alloy layer (by

importing light intensity and layer absorption coeffiecint) so the graded structure was considered as step garded. A matlab code was written to calculate the generation rate out of nextnano in each 1 nm. As the graded structure thickness was 100 nm so there were 100 layers due to step graded definition. Matlab code calculated the generation rate in each 1 nm by considering (calculating) alloy content, absorption coefficient and light intensity in each layer. The obtained generation rate was imported to nextnano+ to calculate the *J-V* curve. All structures were considered strained to the GaN lattice constant. The efficeincy of the HMJ is the maximum among all structures. Efficiency in FBG is larger than SW. V_{oc} for all structures were the same so the parameter which influeneced solar cell efficeincy was J_{sc}. Generation rate which was obtained by a Matlab code indicated that the maximum generation rate for HMJ is larger than the two other structures. In addition, the generation rate for FBG is larger than SW which was due to sharp barriers in the SW structure. However, the efficiency of HMJ is larger than FBG but we remember that making a p type layer is difficult in InGaN structures.

For Λ shape graded structure, the whole structure is 100 nm which contains two graded layers. The first layer went from GaN to $In_{x_{max}}Ga_{1-x_{max}}N$ (0-50 nm), then the second layer went from $In_{x_{max}}Ga_{1-x_{max}}N$ to GaN (50-100 nm). Again, the graded layers provided p and n type doping due to polarization doping. To study the solar cell parameters, again the graded structure was converted to step-graded structure. Then, the illumintaed *J-V* curve was obtained to study the correlated parameters such as J_{sc}, V_{oc}, Fill Factor (FF) and efficiency. V_{oc} results for strained and relaxed structures followed the bandgap plot which already was obtained from nextnano as there is a direct correlation between V_{oc} and E_g. On the other hand, for J_{sc} the relation is reverse. The efficeincy for strained structure showed a maximum efficeincy at $x_{max} = 60\%$. For relaxed the structures, the efficieny was increased by increasing x_{max}. The

Fill Factor for both relaxed and strained were the same in low x_{max} but for strained structure at high x_{max}>=70% the FF drpos. To avoid facing negative bandgap, for strained structure only x_{max}<=90% was considered. For relaxed structure also x_{max}<=90% was condidered due to unique properties between 85% to 100% for V_{oc}.

7.1.1 Conclusion

Power dependence PL for Λ-shape graded structure was measured to study the source of each peak for Λ-shape $In_xGa_{1-x}N$ graded structure with power law. According to power law data for Sample A, peak 1 is exciton like transition. Alpha for peak 1 is larger then one (1.25) which can be considered as a combination of free carrier transition with competition of non-radiative channels allowing for longer lifetime carriers to find lower energy radiative states. This idea is confirmed by the fact that peak1 shows a redshift with excitation power. Peak 2 is also exciton like transition. For sample B, peaks 2 and 4 are exciton like transitions, with α_2=1.32 demonstrating some free carrier effect. In addition, for peak2, the red shift is replaced by a blueshift indicating a quatnum confined stark effect. All other peaks in both samples are free to bound or donor-acceptor pair recombination.

We proved that under fully strained conditions, the PL peak position for the simulation correlates with band to band transitions localized at interface. However, when the structure indicates partial relaxation the experimental PL is located between the fully strained and fully relaxed simulations.

The comparison of solar efficiency of p-i-n graded structurse with two common structures (HMJ, SW) showed that all structures are optimum at x_{max}~60% which are confirmed in other reports. In the same study, however the efficiency of HMJ is higher than the graded structure, but we believe that using graded structure has some advantage such as creating p type

matieral. In addition, the graded sidewalls facilitated higher indium compositions alloys under strain.

According to the simulations, the Λ-shape graded structure demonstrated p-n junction response under both strained to GaN lattice constant and relaxed. For the strained case, the maximum efficiency is obtained around $x_{max} = 60\%$, but for the relaxed case, the solar efficiency is found to continue to increase with increasing x_{max} . This indicates the potential to develop novel, high efficiency solar cell structure by manipulating the strain in these structures.

7.2 Future study

For relaxed Λ-shape graded structures, as the composition increases through the range, $87\% \leq x_{max} \leq 100\%$, the V_{oc} is found to increase. It was found ththat this is related to a change of the polarization doping from strictly a p-n structure to a more complicated p-n-p-n structure due to the interplay between the spontaneous and the piezoelectric polarizations. This subject needs deeper study in comparison with an unpolarized homojunction pnpn structures. The energy band diagram of the graded device exhibits a barier for the dark current within the n type layer (between 55 to 85 nm) which by increasing x_{max} getting larger. To overcome this barrier, carriers need more energy which results in higher V_{oc} to generate zero current. This can be part of future study for these structures, especially in comparison with actual fabricated devices.

In addition to some initial studies of novel doping schemes resulting from polarization doping, there have been some initial simulations showing that these types of III-nitride based solar cells have great potential for efficient operation at elevated temperatures of several hundred degrees. Further studies of this by both simulations and fabrication should prove extremely fruitful.

Appendix

Calculating generation rate for Homojunction and Square well which contain one and three layeres respectively were done with Nextnano3. An input file to calculate generation rate for a Homojunction structure is given here. Generally to calculate generation rate with nextnano3, absorption coeffiecient and solar spectrum intensity which hits this layer should get imported as alink (.dat) file in nextnano3 input file. To make a .dat file, the excel file which contains a wavelength column and absorption coefficient (or solar spectrum intensity) were converted to text file (.rnp). Opening the text file by notepad and save it as .dat file able us to import it into input file.

Input file for generation:

%FunctionParser = yes

---------------Graded Structure--

$simulation-dimension

dimension = 1

orientation = 1 0 0

$end_simulation-dimension

$numeric-control

 simulation-dimension   = 1

 varshni-parameters-on   = yes

newton-method   = Newton-1

current-poisson-method   = block-iterative

current-problem   = integrate-current

current-problem-iterations   = 100

 current-problem-residual   = 1d-11

current-block-relaxation-Fermi   = 0.1d0

$end_numeric-control

$import-data-on-material-grid

 source-directory   = m:/

 import-generation   = no

 filename-generation = read_in_generation1D.in

$end_import-data-on-material-grid

$optical-absorption

destination-directory   = **optics/**

import-absorption-spectrum   = yes

file-absorption-spectrum   = **"C:\Users\radman\Desktop\Links\Links with Strain\HMJ-Relaxed\Alpha-70R.dat"**

import-solar-spectrum   = yes

file-solar-spectrum   = **"C:\Users\radman\Desktop\Links\New Links\solar I0.dat"**

number-of-suns   = 1.0d0

calculate-black-body-spectrum = no

$end_optical-absorption

$global-parameters

 lattice-temperature = 300d0

$end_global-parameters

$simulation-flow-control

flow-scheme   = 4

 strain-calculation = homogeneous-strain

$end_simulation-flow-control

$domain-coordinates

 domain-type = 1 0 0

x-coordinates = 0d0 100d0

hkil-x-direction = 0 0 0 1

hkil-y-direction = 0 1 -1 0

growth-coordinate-axis = 1 0 0

pseudomorphic-on = GaN

$end_domain-coordinates

$regions

region-number = 1   base-geometry = line   region-priority = 1

x-coordinates = 0d0   100d0

$end_regions

$grid-specification

 grid-type = 1 0 0

x-grid-lines = 0d0 100d0

x-nodes = 99

x-grid-factors = 1d0

$end_grid-specification

$region-cluster

cluster-number = 1 region-numbers = 1 2

$end_region-cluster

$material

material-number = 1

material-name = In(x)Ga(1-x)N

cluster-numbers = 1

alloy-function = constant

$end_material

$alloy-function

material-number   = 1

function-name   = constant

xalloy   = 0.7d0

In(x)Ga(1-x)N, vary-from-pos-to-pos   = 0d0 100d0

orientation   = 1 0 0

$end_alloy-function

As it explained earlier, to calculate generation rate for graded structure, it should change to step graded (layers with fix alloy) because nextnano can calculate the generation rate for a fix alloy in each imput file. A Matlab code was written to calculate generation rate for a grdaed structure(Λ, FBG) under relaxed and strined. Matlab code calculates alloy, absorption coefficient, light intensity, and generation rate in each layer and at the end give total generation rate versus position in the whole structure by integration over wavelength.

Matlab code to calculate generation rate for Λ-garded structure under relaxed to GaN lattice constant:

D=50; %Half of thickness

d= 1; %step

X=90; %maxconcentration

```matlab
N=D/d;   % Number of steps /2

y=zeros;  % Indium composition(%)

Eg=zeros;

a=zeros;

b=zeros;

x=zeros; % y/100

E=zeros; % Energy of photon

phi=zeros; % Photon flux

G=zeros;  %Generation ( position)

g=zeros;%Generation ( position at each lambda)

Ge=zeros;%Generation ( position- concenteration)

l=zeros;% position( 2D -0)

for n=1:N

y(n)=(X/(D-d))*(n-1)*d;

end

for n=N+1:2*N

y(n)=(X/(D-d))*(2*N-n)*d;

end

alfa=zeros;

for i=1:2*N

   x(i)=y(i)/100;

   Eg(i)=1.399*(x(i)^2)-4.0801*x(i)+3.4372;

   a(i)=12.87*(x(i).^4)-37.79*(x(i).^3)+40.43*(x(i).^2)-(18.35*x(i))+3.52;
```

```matlab
    b(i)=-2.92*x(i).^2+4.05*x(i)-0.66;

  for j=1:1522

    E(j)=1240/lambda(j);

    if a(i)*(E(j)-Eg(i))+b(i)*(E(j)-Eg(i))^2 >= 0    &&  (E(j)-Eg(i)) > 0

      alfa(j,i)=100000*(a(i)*(E(j)-Eg(i))+b(i)*(E(j)-Eg(i))^2)^(1/2);

    else

    alfa(j,i)=1;

    end

  end

end

t=((10)^(-7))*d;

I=zeros;

I=I0;

for j=1:1522

    I(j,1)=I0(j);

end

for i=1:N-1

  for j=1:1522

    I(j,i+1)=I(j,i)*exp(-alfa(j,i)*t);

  end

end

for j=1:1522

  I(j,N+1)=I(j,N)*exp(-alfa(j,N)*t);
```

```
end

for i=N+1:2*N-1

   for j=1:1522

      I(j,i+1)=I(j,i)*exp(-alfa(j,(2*N+1)-i)*t);

   end

end

for j=1:1522

   for n=1:2*N

phi(j,n)=6.24*(10^14)*I(j,n)/E(j);

   end

end

  for n=1:2*N

    for i=1:10*d

      G(i,n)=0;

     for j=1:1521

     g(j,i,n)=(lambda(j+1)-lambda(j))*phi(j,n)*alfa(j,n)*exp(-alfa(j,n)*(i*(10^-8)));

     G(i,n)=G(i,n)+g(j,i,n);

      end

    end

  end

  Ge(1)=0;

  l(1)=2*D;

  for n=1:2*N
```

```matlab
    for i=((n-1)*d*10)+1:1:(n*d*10)

        l(i+1)=l(i)-(1/10);

    end

end

j=1;

for n=1:2*N

    for i=1:10*d

        Ge(j)=G(i,n);

        j=j+1;

    end

end

M=2*N*d*10+1;

Ge(M)=0;

hold on

plot(l,Ge,'B')

legend('X=7')

hold off

GP=zeros;

for i=-1:-1:-2*N*d*10

    GP(i+2*N*d*10+1,1)=l(-i);

    GP(i+2*N*d*10+1,2)=Ge(-i);

end
```

135

To calculate light J-V curve for graded structure, generation rate link should get imported into nextnano plus.

1D example for solving current-poisson

$MYSOLAR="**C:\Users\radman\Desktop\V(Graded)(100nm-devices)\V(Graded-Relaxed)(1nm)(New-Matlab)\Temperature-Dependence\40(TDependence)\G(300K)(40).dat**"

```
global{

  simulate1D{}

  crystal_wz{

    x_hkl = [ 0, 0, 1]

    y_hkl = [ 1, 0, 0]

  }

  substrate{

    name = "GaN"

  }

  temperature = 300E0

}<>


grid{

  xgrid{


    line{ pos = -10 spacing = 0.1}
```

```
    line{ pos = 0 spacing = 0.1}

    line{ pos = 50spacing = 0.1}

    line{ pos = 100 spacing = 0.1 }

    line{ pos = 110 spacing = 0.1}

  }

#periodic{x = no}

 }

contacts{

  ohmic{

    name = contact1

    bias = [0,0.05]

steps=2 # [V]

  }

  ohmic{

    name = contact2

    bias = 0.0 # [V]

  }

 }<>

impurities{

 #donor{   name=Si   energy=0.0058   degeneracy=2 }

  donor{   name=Si   energy= -1000   degeneracy=2 }

 #acceptor{ name=B    energy=0.027    degeneracy=4 }

  acceptor{ name=Saeed    energy= -1000  degeneracy=4 }
```

137

```
}

structure{

  output_region_index{ boxes = no }

  output_material_index{ boxes = no }

  output_alloy_composition{ boxes = no }

  output_impurities{ boxes = no }

  output_contact_index{}

region{

  everywhere{}

  generation{

    import{ import_from = "GenImportProfile" }

   }

 }

  region{

    line{x = [-10, 0]}

    contact{ name = contact1 }

    ternary_constant{name="In(x)Ga(1-x)N"

         alloy_x =0.00}

doping{constant{ name="Saeed" conc=5e18 }}

}

region{

    line{

      x = [0E0, 50E0]
```

```
  }

  ternary_linear{

    name    = "In(x)Ga(1-x)N"

    alloy_x =  [0, 0.4]

    x       = [0, 50]

  }

}

region{

  line{

    x = [50E0, 100E0]

  }

  ternary_linear{

    name    = "In(x)Ga(1-x)N"

    alloy_x =  [0.4, 0]

    x       = [50, 100]

  }

}

region{

  line{

    x = [100E0, 110E0]

  }

  contact { name = contact2}

  ternary_constant{name="In(x)Ga(1-x)N"
```

```
        alloy_x =0.00}

doping{

    constant{ name="Si" conc=5e18 }}

   }

}

strain{

 pseudomorphic_strain{}

piezo_density= yes

pyro_density = yes

output_polarization_charges{}

}<>


classical{

  Gamma{}

  HH{}

  LH{}

  SO{}


output_bandedges{ averaged=no }

output_bandgap{}

  output_carrier_densities{}

  output_ionized_dopant_densities{}

  output_intrinsic_density{}
```

```
}


poisson{

  output_potential{}

  output_electric_field{}

}


currents{

  recombination_model{

    SRH      = yes

    Auger    = yes

    radiative = yes

  }

  output_fermi_levels{}

  output_currents{}

  output_mobilities{}

  output_recombination{}

}

import{

  file{

    name = "GenImportProfile"

 # name for referencing the imported data in the input file

    filename = $MYSOLAR
```

```
  # name of file which is imported

    format = DAT

 # format of the file to be imported. At the moment only AVS format and a simple .dat format is

supported.

    scale = 1e18

# Import Spectra is in 1e18 1/[cm^3] imported data is multiplied by this scaling factor (optional,

default value is 1.0)

  }

  output_imports{}

# output all imported data including scale factor.                                         # The

filenames correspond to the entry given in name = ...                                      # The

files will be written to a folder called Imports/

}

run{

  solve_current_poisson{

    output_log = yes

    iterations        = 5000

    current_repetitions  = 3

    alpha_fermi       = 0.008

    alpha_iterations    = 2000

    residual_fermi     = 1e-2 #1e-6

    residual         = 1e3

}
```

```
  solve_strain{}

}<>
```